



# **A $CC1\pi^+/CCQE$ Cross-Section Ratio Measurement on Carbon using the T2K Near Detector**

Thesis submitted in accordance with the requirements of the University of Liverpool for  
the degree of Doctor in Philosophy

**Matthew Murdoch**

Oliver Lodge Laboratory,

University of Liverpool,

August 2012

# Abstract

T2K is a long baseline neutrino oscillation experiment designed to measure the  $\theta_{23}$  and  $\theta_{13}$  mixing angles to high precision using  $\nu_\mu$  disappearance and  $\nu_e$  appearance respectively. A major component of the T2K near detector is the electromagnetic calorimeter; the construction, commissioning and operation of the ECal is describe in detail in this thesis. T2K uses the dominant CCQE neutrino interaction as a clean and simple signal in oscillation measurements. However, other interaction processes interfere with the oscillation measurements, a large contribution to this interference for  $\nu_\mu$  analyses is from  $CC1\pi^+$  interactions. This thesis measures the  $\nu_\mu$   $CC1\pi^+$ /CCQE cross-section ratio on  $C_8H_8$  using the T2K near detector. As an internal consistency check, the flux integrated ratio is calculated as  $R^{MC} = 0.235 \pm 0.019^{Stat} \pm 0.047^{Syst}$  for MC and  $R^{Data} = 0.237$ . The ratio is also measured as a function of incident neutrino energy and finds an agreement with NEUT MC of  $\chi^2/NDOF = 6.6/6$ .

# Acknowledgements

The four years I have spent have been extremely taxing and enjoyable in equal parts. The help and support of many people helped to lighten the load through the trials of this PhD. And conversely, the many highs would not have been so enjoyable without the good company to share them with.

Firstly I must thank the people of Tokai-mura for all they did for me and others in the aftermath of the March 2011 earthquake. Specifically I would like to mention the staff of Masago International Lodgings and the staff of the J-PARC facility who were at times our only source of information and took exceptional care of us throughout the ordeal. To show such kindness to a scared and confused student in the midst of such a disaster is truly a testament to their character.

Next I would like to thank my supervisor Professor Christos Touramanis for his many contributions. You always seem to come through in a pinch, despite your ridiculously busy schedule. More than this, you have taught me much about the world of high energy physics and research. Your advice to me always seems to be on the mark and has been invaluable over the last four years. I should also thank you for putting up with my eccentricities, not least of which is my rather colourful hairstyle strategically adopted after passing first year to avoid getting kicked off the course. I still remember the look on your face that first time you saw it in the KEK dorms, I was slightly worry I'd get fired anyway!

Next on the list is Dr. Neil McCauley whom I have relentlessly bugged and questioned throughout this PhD with myriad physics and coding questions. This was especially true during the final six months whilst writing this thesis. Your explanations and advice have helped in an incalculable manner and your understanding during the summer of 2011 kept me from falling off the radar. You can rest easy that the knocking on your door probably

isn't me with yet more questions.

I would also like to thank the neutrino group beyond my supervisors for all the help and the interesting discussions, your support has been invaluable. Dr Jon Coleman who has been a constant force pushing me on to finishing this thesis and cracking the whip to keep me going. Dr. David Payne, the days of constructing the ECal seem so long ago now, heck you even seem to have gotten over the trauma! Sorry if reading this gave you flashbacks. Dr Kostas Mavrokoridis who has revealed to me the wonders of Liquid Argon TPCs. Dr. Carlos Chavez who spent many hours helping me with my code and all the amusement provided during the construction. And finally, Dr Georgios Christodolou, football, physics, touching DJs, is there anything you can't do?

My fellow students both at Liverpool and on T2K also deserve big thanks. First and foremost, Alex Thorley and Gil 'Smallu' Kogan, you guys have been true friends and put up with me throughout. I'll never forget that 10 hour drive to Tokyo and our parting of ways the next day. Let there be many more reunions of the three. Also, Richard Calland for the many parties and letting me use your room when you moved to Japan. All my bubble chamber team mates, we didn't win this time but in 2013 that trophy is coming home.

I would also like to thank my collaborators on T2K. There are too many to name here but I would like to thank specifically Dr. Roberto Sacco, Dr. Philip Litchfield and Dr. Martin Haigh for all their help whilst I was getting to grips with the ECal system and commissioning. Your help made a difficult job much easier.

Thank you to STFC and the University of Liverpool for funding and support during this PhD.

Thank you to all of you who made my time in Japan so enjoyable. Rika-san for Pono-Pono, the best bar in Tokai. Okuna-sensei, Sakamoto-sensei and Miura-sensei for teaching me Japanese (sorry I wasn't a very good student) and Maki-san who took me to hospital when I broke my shoulder and took care of so much admin. I should give a special mention to Tiff and Yvonne who took me around Tokyo and 'showed me the ropes' as it were. You knew all the best things to do in Tokyo, I had a lot of fun.

Finally I thank my family for all their help over the years. I could not have achieved this without your love and support. If I were to try to list everything you all have done for me,

it would surely be longer than the rest of this thesis (and a few other peoples on top). My mother Gillian, you put up with all my practical joking and always have my best interests at heart, I'm glad I could do you proud. My brother Phil, you are the single most annoying person I have ever known... but seriously, you've helped me more than you realise. Thank you for, 'You're too stubborn to die'. Nan, you have supported me throughout my days and kept me fed through the tough times, thank you. Also, to my aunts and uncles all of whom have helped me immensely through the years, I owe you all so much.

## **Declaration**

I hereby declare that all work in this thesis that is not my own has been properly referenced.

# Contents

<b>Contents</b>	<b>i</b>
<b>1 Neutrino Physics</b>	<b>1</b>
1.1 Initial Observations . . . . .	1
1.2 The Evidence for Oscillations . . . . .	2
1.3 Neutrino Oscillation Theory . . . . .	4
1.4 Measurement of Oscillation parameters . . . . .	7
1.5 Charged Current Neutrino Interactions . . . . .	10
1.5.1 Charge Current Quasi-Elastic Interactions . . . . .	13
1.5.2 Charged Current, Neutrino Induced Pion Production . . . . .	13
1.5.3 Nuclear Re-Interactions . . . . .	18
<b>2 The T2K Experiment</b>	<b>20</b>
2.1 Experiment Overview . . . . .	20
2.2 The J-PARC Accelerator Complex and the T2K Beamline . . . . .	22
2.3 The Far Detector : Super-Kamiokande . . . . .	24
2.3.1 The Neutrino Beam at Super-Kamiokande . . . . .	26
2.4 The INGRID Detector . . . . .	27
2.5 The ND280 Detector . . . . .	29
2.5.1 The $\pi^0$ Detector . . . . .	29
2.5.2 The Time Projection Chambers (TPC) . . . . .	30
2.5.3 The Fine Grained Detectors (FGD) . . . . .	32
2.5.4 The Electromagnetic Calorimeters (ECals) . . . . .	33
2.5.5 The Side Muon Range Detector (SMRD) . . . . .	34

<b>3</b>	<b>Construction of the ND280 Barrel ECal</b>	<b>37</b>
3.1	Calorimeter Detectors . . . . .	37
3.2	Detector Design . . . . .	40
3.2.1	Geometry and Dimensions . . . . .	40
3.2.2	Construction Materials . . . . .	41
3.3	Detector Electronics and Readout . . . . .	42
3.3.1	Multi-Pixel Photon Counters (MPPCs) . . . . .	42
3.3.2	TripT Front-end Boards (TFBs) . . . . .	43
3.4	Construction of the Barrel ECal modules . . . . .	45
3.4.1	Preparation . . . . .	45
3.4.2	Layer Construction . . . . .	46
3.4.3	Layer Insertion . . . . .	47
3.4.4	Fibre Insertion . . . . .	48
3.4.5	Layer Scanning . . . . .	50
3.4.6	Finalisation and MPPC Connection . . . . .	51
3.4.7	Shipping . . . . .	54
3.5	On Site Checkout and Testing . . . . .	54
<b>4</b>	<b>ECal Commissioning and Operation</b>	<b>56</b>
4.1	Readout Electronics . . . . .	56
4.1.1	Electronics Front-End . . . . .	57
4.1.2	Electronics Back-End . . . . .	57
4.2	Data Acquisition . . . . .	58
4.2.1	Processor Nodes . . . . .	59
4.3	Detector Commissioning . . . . .	59
4.4	MPPC Gain Calibration . . . . .	61
4.4.1	Calibration Method . . . . .	62
4.4.2	Calibration Issues . . . . .	65
4.4.3	Procedure Improvement . . . . .	65
4.4.4	Pedestal Calculation . . . . .	66



4.5	Detector Operation . . . . .	66
4.5.1	Calibrations . . . . .	67
4.5.2	Data Quality . . . . .	67
4.5.3	Detector Monitoring . . . . .	70
4.6	System Recovery . . . . .	74
4.6.1	Hardware Inspection . . . . .	74
4.6.2	Re-commissioning . . . . .	76
<b>5</b>	<b>ND280 Event Reconstruction</b>	<b>79</b>
5.1	The ND280 Offline Software Chain . . . . .	79
5.2	ND280 Reconstruction . . . . .	80
5.2.1	Tracker Reconstruction . . . . .	81
5.2.2	TPC Reconstruction . . . . .	81
5.2.3	TPC PID . . . . .	82
5.2.4	FGD Reconstruction . . . . .	83
5.2.5	Vertex Reconstruction . . . . .	83
5.2.6	ECal Reconstruction . . . . .	84
5.2.7	P0D Reconstruction . . . . .	84
5.3	Global Reconstruction . . . . .	85
<b>6</b>	<b>A <math>CC1\pi^+/CCQE</math> Cross Section Ratio Measurement</b>	<b>86</b>
6.1	Measurement Motivation . . . . .	86
6.1.1	Defining the Signals . . . . .	88
6.1.2	Event Binning . . . . .	89
6.2	Data Sets and Monte Carlo . . . . .	89
6.2.1	Data Quality . . . . .	90
6.3	Selecting Charged Current Events . . . . .	91
6.3.1	Beam Timing . . . . .	92
6.3.2	FGD Fiducial Volume . . . . .	92
6.3.3	Muon Identification . . . . .	94
6.3.4	Veto Cuts . . . . .	95

6.4	CCQE Event Selection . . . . .	97
6.4.1	CCQE Overview . . . . .	99
6.5	$CC1\pi^+$ Event Selection . . . . .	105
6.5.1	$CC1\pi^+$ Overview . . . . .	106
6.6	Neutrino Energy Reconstruction and Ratio Calculation . . . . .	109
6.7	Detector and Reconstruction Systematics . . . . .	111
6.7.1	TPC Track Finding Efficiency . . . . .	111
6.7.2	TPC Broken Tracks . . . . .	112
6.7.3	FGD-TPC Matching Efficiency . . . . .	113
6.7.4	Charge Confusion . . . . .	113
6.7.5	Michel Electron Tagging . . . . .	114
6.7.6	Vertex Reconstruction . . . . .	115
6.7.7	TPC PID . . . . .	116
6.7.8	Veto Systematics . . . . .	117
6.7.9	FGD Multiplicity Systematic . . . . .	118
6.7.10	Momentum Resolution . . . . .	119
6.7.11	Momentum Scale . . . . .	119
6.7.12	Fiducial Mass Uncertainty . . . . .	120
6.7.13	Detector and Reconstruction Systematics Overview . . . . .	121
6.7.14	Sand Muons . . . . .	122
6.8	Interaction and Model Systematics . . . . .	122
6.8.1	Event ReWeighting . . . . .	122
6.8.2	Flux Uncertainty . . . . .	123
6.8.3	Neutrino Interaction and Final State Interaction Uncertainties . . .	125
6.9	Results . . . . .	127
<b>7</b>	<b>Conclusions</b>	<b>135</b>
	<b>Bibliography</b>	<b>137</b>

# Chapter 1

## Neutrino Physics

From its very beginning the nature of the neutrino has been shrouded in mystery. In keeping with its inception, the history of the neutrino provided a few surprises and remains one of the least understood fundamental particles. This chapter will give an outline of the history of the neutrino starting with its observation. An overview of the solar and atmospheric neutrino problems and their implications will be presented. Finally, the theory behind neutrino oscillations and interactions will be discussed.

### 1.1 Initial Observations

The existence of the neutrino was first hypothesised in 1930 by Wolfgang Pauli to explain the continuous energy spectrum of electrons[1] and non-conservation of spin in nuclear beta decay. The neutrino was predicted to have neutral charge, spin half, and a mass of the same order as the electron. In 1933, the neutrino was included in Enrico Fermi's theory of nuclear beta decay[2], producing the first theoretical model of the weak interaction. This made the neutrino the first particle to be theoretically described before being directly observed.

The neutrino was first observed experimentally by Cowan and Reines in 1956[3][4]. Cowan and Reines used a 200 litre water target with liquid scintillator detectors to detect the anti-neutrinos from a nearby nuclear reactor. The experiment relied on observing the delayed coincidence events of annihilation and capture of the positron and neutron from an

inverse beta decay interaction in the water.

$$\bar{\nu}_e + p \rightarrow n + e^+ \quad (1.1)$$

In 1962 the muon neutrino was discovered at Brookhaven National Laboratory[5] in the first accelerator neutrino experiment. The experiment produced a beam of muon neutrinos by firing protons at a target. This resulted in a beam of pions produced travelling along a decay volume pointed towards the detector. The pions decay in flight to a muon and a neutrino. Due to the boost from the pion's momentum, the neutrinos are produced travelling in a forward going beam in the lab frame. Any pions and muons remaining at the end of the decay volume were directed to a beam dump. This method of creating a neutrino beam is still used in accelerator experiments today. The experiment found that only a muon could be produced in the resulting neutrino interactions, showing the muon neutrino to be distinct from the previously observed electron neutrino.

In 1975 the tau lepton was discovered[6], and with it, a third neutrino flavour was predicted. Strong evidence for a third neutrino flavour was obtained at CERN when the LEP experiment observed that the Z boson width was consistent with three flavours of neutrino[7]. Direct observation of the tau neutrino was difficult due to the large mass of the tau lepton and its short lifetime. Direct observation of the tau lepton was obtained by the DONUT experiment in 2000[8].

## 1.2 The Evidence for Oscillations

The nuclear reactions in the core of the Sun produce a massive flux of electron neutrinos that can be observed on Earth. Measuring the flux of neutrinos from the Sun could therefore test the validity of theoretical solar models. The Homestake experiment first measured the flux of these solar neutrinos in 1968[9]. The experiment used electron neutrino capture on Chlorine atoms to produce  $Ar^{37}$  in the reaction,

$$\bar{\nu}_e + Cl^{37} \rightarrow n + Ar^{37} \quad (1.2)$$

The Argon was then filtered off and its decays observed to count the number of neutrino

interactions. The neutrino flux observed was found to be roughly 30% of that predicted by the Standard Solar Model. Further solar neutrino observatories[10][11] and reactor experiments[12] also saw a deficit in the flux. This discrepancy became known as the solar neutrino problem. It is important to note that the Homestake experiment was only sensitive to electron neutrinos and so the measurement was not of the total neutrino flux.

The Kamiokande experiment in Japan was another one to measure the solar neutrino flux. Kamiokande was a water Čerenkov detector originally built to search for proton decay. The detector was upgraded in 1985 to become a neutrino observatory. In 1989 Kamiokande reported a solar neutrino flux measurement[13] finding the solar neutrino flux to be roughly half that expected. Furthermore, Kamiokande was capable of reconstructing the energy and momentum of the incident neutrinos. This made it the first to confirm the solar origin of the neutrinos.

The most probable causes of the observed deficit were either errors in the solar model or in the neutrino theory. The agreement of several, large, independent experiments made the prospect of experimental error very unlikely. Modifications to the solar model were suggested but none could provide sufficient agreement with the observed fluxes. This left only the possibility that something happened to the neutrinos between their creation and their observation, thus the theory of neutrino oscillations was born. If neutrino mixing occurred analogously to quark flavour mixing, the deficit could be explained by electron neutrinos oscillating to other flavours. Neutrinos were previously thought to be massless however oscillations require them to have a small but non-zero mass, contrary to SM predictions.

Concurrently to their solar neutrino flux measurement, Kamiokande found an anomaly in the flavour ratio of neutrinos from atmospheric cosmic rays[14]. When cosmic rays interact in the upper atmosphere, pions are produced. These pions then decay to muons and muon neutrinos. These muons also decay to electrons, muon neutrinos and electron neutrinos. It was therefore expected that the ratio of muon neutrinos to electron neutrinos would be close to 2:1. The number of electron neutrinos from atmospheric cosmic rays was found to be consistent with Monte Carlo predictions. However, the observed muon neutrino flux was roughly 60% of the predicted value. The muon neutrino deficit result was later confirmed by the IMB experiment[15]. These observations strengthened the case

for neutrino oscillations. The solution to the atmospheric neutrino anomaly came when Super-Kamiokande observed a strong zenith angle dependence in the muon neutrino flux whilst the electron neutrino flux remained independent of the angle[16].

The solution to the solar neutrino problem and thus evidence for neutrino oscillations was given by the SNO experiment[17]. SNO measured both the overall neutrino flux in conjunction with the electron neutrino flux. The overall flux was measured using neutral current (NC) interactions[18] that are mediated by the Z boson as opposed to charged current (CC) interactions mediated by the charged W bosons. In NC current interactions no lepton is produced and so they are not sensitive to lepton flavour. The overall flux was measured to be consistent with that predicted by the solar model. This measurement, combined with the deficit of electron neutrinos showed conclusively that the neutrinos were oscillating between flavours.

Further confirmation was given by the KamLAND reactor neutrino experiment[19] in 2003 where the disappearance of anti- $\nu_e$ s was measured and a flux 60% of expectation was observed. Combining the KamLAND data with the solar neutrino observations identified neutrino oscillations as the cause of the solar neutrino problem to greater than  $5\sigma$ [20]. Beam neutrino experiments further confirmed neutrino oscillation theory, the first being K2K[21], followed by MINOS[22] and most recently T2K[23].

### 1.3 Neutrino Oscillation Theory

When a neutrino is created it has a definite weak flavour eigenstate,  $|\nu_\alpha\rangle$ , in accordance with flavour conservation in the Weak Interaction. If we allow neutrinos to have mass, their mass eigenstates,  $|\nu_i\rangle$ , need not necessarily be identical to the flavour eigenstates. In this case the definite flavour eigenstates are created in a superposition of the mass eigenstates, conserving energy and momentum at the decay vertex. In the case that neutrino oscillations do not occur, the mass eigenstates are identical to the flavour eigenstates.

$$|\nu_\alpha\rangle = |\nu_j\rangle \tag{1.3}$$

where  $\alpha = e, \mu, \tau$  and  $j = 1, 2, 3$ . However oscillations can occur if the sets of eigenstates are not identical and

$$|\nu_\alpha\rangle = \sum_j U_{\alpha j} |\nu_j\rangle \quad (1.4)$$

Where  $U_{\alpha j}$  is the mixing matrix. In this case the relative phase of the different mass states changes as the neutrino propagates through space. When the neutrino arrives at a detector some distance later, it will be in a different superposition of mass eigenstates and a different flavour neutrino may be observed.

The neutrino mixing matrix  $U$  is analogous to the CKM matrix that describes flavour mixing in the quark sector. For the predicted three flavour scenario, the neutrino mixing matrix is 3x3, unitary and complex. The matrix is known as the Pontecorvo-Maki-Nakagawa-Sakata (PMNS) matrix[24][25] and can be written in terms of three mixing angles and a complex phase as:

$$U = \begin{pmatrix} c_{12} & s_{12} & 0 \\ -s_{12} & c_{12} & 0 \\ 0 & 0 & 1 \end{pmatrix} \begin{pmatrix} c_{13} & 0 & e^{i\delta} s_{13} \\ 0 & 1 & 0 \\ -e^{i\delta} s_{13} & 0 & c_{13} \end{pmatrix} \begin{pmatrix} 1 & 0 & 0 \\ 0 & c_{23} & s_{23} \\ 0 & -s_{23} & c_{23} \end{pmatrix} \quad (1.5)$$

where  $s_{jk}$  and  $c_{jk}$  are  $\sin\theta_{jk}$  and  $\cos\theta_{jk}$  respectively. It is important to note for later that the CP-violating phase  $\delta$  is always multiplied by a factor of  $\sin\theta_{13}$ .

In order to calculate the oscillation effect this produces, we first consider the time evolution of a neutrino propagating through a vacuum. We use the Schrödinger equation to derive a time dependent version of Equation 1.4 such that after time  $t$ , a neutrino of flavour  $\alpha$  is described by,

$$|\nu_\alpha(t)\rangle = \sum_j U_{\alpha j}^* e^{-iE_j t} |\nu_j\rangle \quad (1.6)$$

where  $|\nu_j\rangle$  is a mass eigenstate of energy  $E_j$ . We also rearrange Equation 1.4 to describe the mass eigenstates as a superposition of the flavour eigenstates, giving,

$$|\nu_j\rangle = \sum_\alpha U_{\alpha j} |\nu_\alpha\rangle \quad (1.7)$$

Substituting this into the previous equation gives,

$$|\nu_\alpha(t)\rangle = \sum_{j,\beta=e,\mu,\tau} U_{\alpha j}^* e^{-iE_j t} U_{\beta j} |\nu_\beta\rangle, \quad (1.8)$$

showing that a pure eigenstate  $\alpha$  at  $t = 0$  will be described by a superposition of flavour states at time  $t > 0$ . The probability of measuring a given flavour eigenstate  $\beta$  at time  $t$  later is given by the amplitude of the  $|\nu_\beta\rangle$  component in  $|\nu_\alpha(t)\rangle$  i.e.

$$P_{\alpha \rightarrow \beta}(t) = |\langle \nu_\beta | \nu_\alpha(t) \rangle|^2 \quad (1.9)$$

Using what we know from Equation 1.8 we get,

$$P_{\alpha \rightarrow \beta}(t) = \sum_{j,k} U_{\alpha j}^* U_{\beta j} U_{\alpha k} U_{\beta k}^* e^{-i(E_k - E_j)t} \quad (1.10)$$

The neutrino masses are known to be small and so neutrinos can be assumed to be ultra relativistic. Taking the ultra relativistic limit we use  $E = p + \frac{m^2}{2p}$  where  $p$  is the scalar momentum of the neutrino. In this limit we also assume that rest mass is negligible such that  $p = E$  and that the neutrino travels at the speed of light so that  $t = L$  in natural units, where  $L$  is the distance travelled by the neutrino. As only the mass differences enter into the oscillation equation, we define  $\Delta m_{jk}^2 = m_k^2 - m_j^2$ . Putting all this into the above equation yields,

$$P_{\alpha \rightarrow \beta}(t) = \sum_{j,k} U_{\alpha j}^* U_{\beta j} U_{\alpha k} U_{\beta k}^* e^{-i \frac{\Delta m_{jk}^2 L}{2E}} \quad (1.11)$$

This equation can be viewed as two distinct pieces. The first half contains only PMNS mixing matrix elements and gives the overall amplitude of the oscillations. These contain the complex phase  $\delta$ . The sign of the imaginary components will change under the  $\hat{C}P$  operation. If the phase is non-zero, this will result in different oscillation amplitudes for neutrinos and anti-neutrinos and thus CP-violation will exist in the lepton sector. The second half is the exponential phase term that depends on three parameters,  $\Delta m_{jk}^2$ ,  $L$  and  $E$ . The  $L$  and  $E$  parameters are set by the experiment and can be chosen such that a given



mixing  $\alpha \rightarrow \beta$  is maximal, giving greater sensitivity to the relevant mixing parameters.

The three flavour oscillation equation is rather unwieldy and so in some cases we simplify to only assume mixing between two flavours. This simplifies  $U$  to a 2x2 rotation matrix, with a single mixing angle  $\theta$ , such that

$$U = \begin{pmatrix} \cos\theta & \sin\theta \\ -\sin\theta & \cos\theta \end{pmatrix} \quad (1.12)$$

This simplification gives the oscillation probability as,

$$P(\nu_\alpha \rightarrow \nu_\beta) = \sin^2 2\theta \sin^2 \left( \frac{\Delta m^2 L}{4E} \right) \quad (1.13)$$

This equation is a valid approximation for oscillation experiments that are sensitive to only one  $\Delta m^2$  mass difference. T2K sits at the oscillation maximum for  $\nu_\mu$  disappearance and so is dominated by the mixing angle  $\theta_{23}$  and so this approximation will be valid in this case.

The formalism described above only holds true for neutrinos travelling in the vacuum. Neutrinos travelling through matter can scatter off of the electrons in the atoms. The contribution from Z boson exchange contributes little as the scattering amplitude is independent of neutrino flavour. W boson exchange however adds an extra potential term to the electron neutrino energy that is dependent on the electron density in the matter. This propagates to give an extra potential term in the mixing matrix, thus altering the probability of oscillation. The short baseline of T2K means that matter effects can be ignored as their effect on the oscillation will be small.

## 1.4 Measurement of Oscillation parameters

Neutrino oscillations are the first 'beyond the Standard Model' physics to be observed and as such much effort over many decades has been put into understanding them. With a brief description of the oscillation formalism and an introduction to the mixing parameters given, the measurement of these parameters will be discussed.

Perhaps unsurprisingly, the parameters  $\theta_{12}$  and  $\Delta m_{12}^2$ , those relating to the solar sector,

are the most well understood. Recent fits combine the data of the solar neutrino and the reactor neutrino experiment's to give best fit measurements of  $\sin^2\theta_{12} = 0.304^{+0.022}_{-0.016}$  and  $\Delta m_{21}^2 = 7.65^{+0.23}_{-0.20} \times 10^{-5} eV^2$ [26]. A contour plot of current knowledge is given in Figure 1.1.

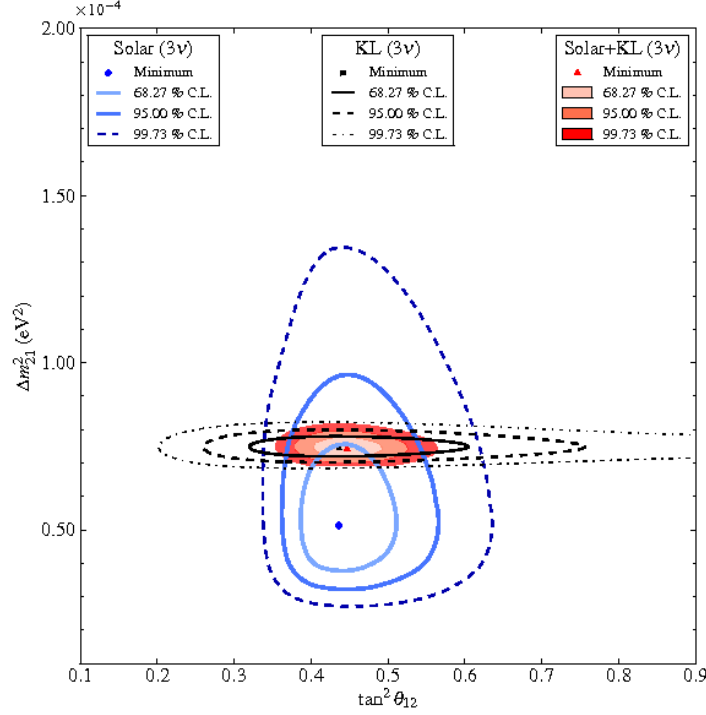


Figure 1.1: The current knowledge of the solar mixing parameters from SNO and KamLAND data in the 3 neutrino mixing case.[27]

The current knowledge of the atmospheric mixing parameters,  $\theta_{23}$  and  $\Delta m_{23}^2$ , has a large contribution from accelerator experiments. The K2K experiment was the first long baseline experiment to publish a  $\nu_\mu$  disappearance result[28]. The current leading measurement in the atmospheric sector comes from the MINOS collaboration giving  $\Delta m_{23}^2 = 2.32^{+0.12}_{-0.06} \times 10^{-3} eV^2$  and  $\sin^2 2\theta_{23} > 0.9(90\%CL)$ [29] using the two flavour approximation. In 2012, T2K published the first  $\nu_\mu$  disappearance result with an off-axis beam using  $1.43 \times 10^{20}$  protons on target (POT)[30], less than 1% of the experiments planned total data. Accelerator experiments so far have been insensitive to the sign of  $\Delta m_{23}^2$ . Therefore it is not yet known which mass eigenstate is the heaviest giving two distinct cases,

$m_1 < m_2 < m_3$  called the normal mass hierarchy and  $m_3 < m_1 < m_2$  called the inverted mass hierarchy.

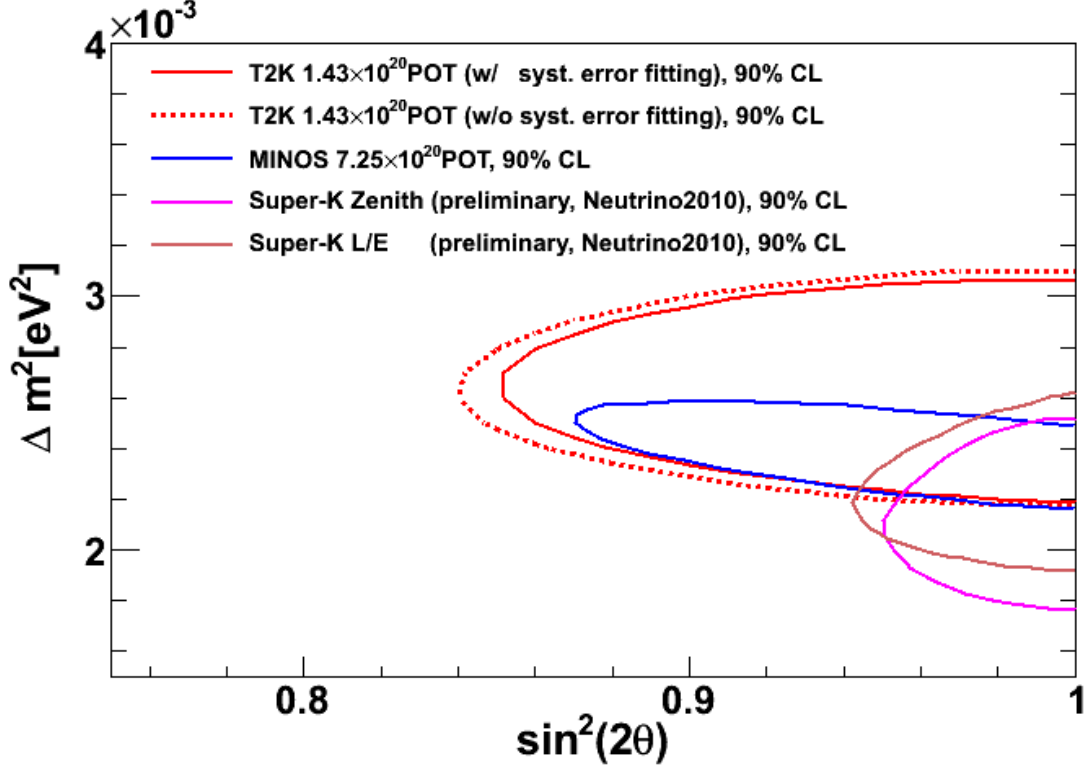


Figure 1.2: The 90% CL for  $\theta_{23}$  from the two T2K analyses[30] compared with data from SK[31] and MINOS[29]

The final mixing angle,  $\theta_{13}$  is the smallest and least precisely measured. Many of the current generation of neutrino oscillation experiments are focussed on measurement of this mixing angle. The measurement of  $\theta_{13}$  is important in the search for CP-violation in the lepton sector. As noted in Section 1.3, the CP-violating phase  $\delta$  is always accompanied by a  $\sin\theta_{13}$  term. Thus CP-violation in the lepton sector is only possible if  $\theta_{13} \neq 0$ . Measurements by CHOOZ[32] and MINOS[33] proved inconclusive, setting limits on the size of  $\theta_{13}$  but not excluding 0. The first significant indication of non-zero  $\theta_{13}$  was given by T2K in 2011 where  $\theta_{13} = 0$  was excluded to  $2.5\sigma$  significance level[34] as shown in Figure 1.3. This result was updated in 2012, improving the significance to  $3.2\sigma$ . In 2012 the Daya Bay reactor experiment publish an anti- $\nu_e$  disappearance measurement showing  $\sin^2 2\theta_{13} = 0.092 \pm 0.016(stat) \pm 0.0005(syst)$ , excluding  $\theta_{13} = 0$  to  $5.2\sigma$  significance[35].

Further evidence for non-zero  $\theta_{13}$  was published by the RENO reactor experiment later in the year[36], excluding zero to  $4.2\sigma$  significance. With strong evidence for a non-zero  $\theta_{13}$ , the current generation of experiments will be able to focus on achieving a precision measurement.

Charged current (CC) interactions are mediated by the charged W bosons whilst neutral current (NC) interactions are mediated by the neutral Z boson. CC interactions have the generic form of  $\nu_l N \rightarrow l X$  where  $l$  is a charged lepton,  $N$  is a nucleon and  $X$  represents the other final state particles. NC interactions take the form  $\nu_l N \rightarrow \nu_l X$  where no charged lepton is produced. As such, CC interactions are used to make oscillation measurements as they are the only interactions that allow observation of the neutrino flavour.

## 1.5 Charged Current Neutrino Interactions

The neutrino physics community has entered an age of precision measurements. The current generation of accelerator based oscillation experiments are designed to achieve statistical sensitivity far greater than previous projects. As the statistical uncertainties decrease, the systematic uncertainties in experiments become more important. The largest systematics associated with most experiments relate to the neutrino flux and interaction cross-sections. To achieve precision measurements, these uncertainties must be reduced through measurement. The flux uncertainty is reduced from experiments such as NA61, that use hadron spectroscopy to measure the hadron production on nuclear targets[37].

Neutrino interaction cross-sections are poorly measured at neutrino energies of order 1 GeV where the oscillation maximum for T2K lies. In this energy region there are three dominant Charged Current processes, Quasi-Elastic (CCQE), Single Pion Production ( $CC1\pi^+$ ) and Deep Inelastic Scattering (DIS). The CCQE process dominates at lower neutrino energies. The main background to the CCQE process is single pion production. As neutrino energy increases, the  $CC1\pi^+$  fraction of CC events increases, becoming equal to the CCQE fraction at  $E_\nu$  of order 2 GeV. At higher energies, DIS becomes the dominant process and the CCQE and  $CC1\pi^+$  fractions fall. Figure 1.4 shows how the cross-section over neutrino energy changes with neutrino energy.

A number of neutrino event generators exist to model the interaction cross-sections

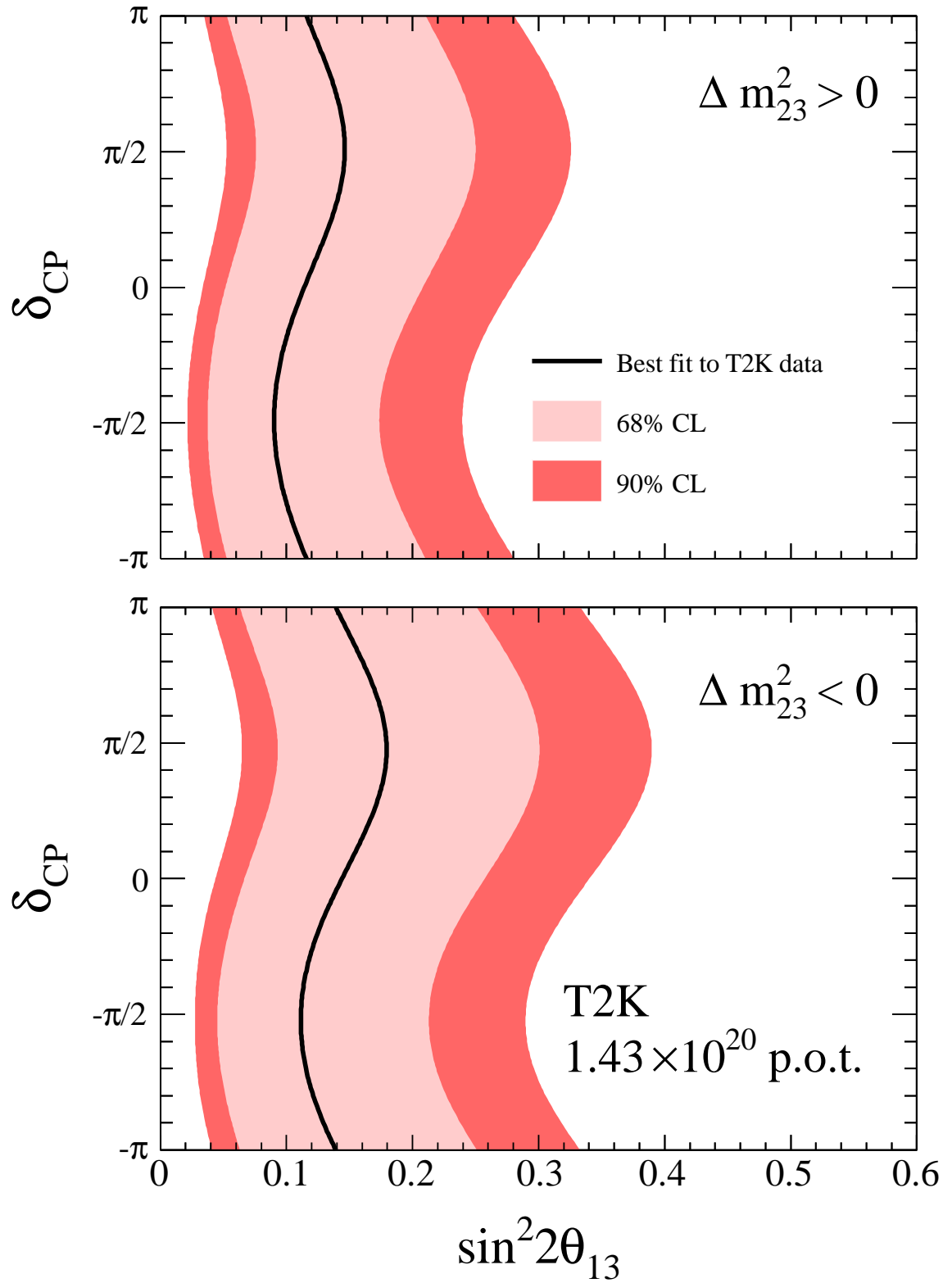


Figure 1.3: The 68% and 90% CL of  $\sin^2 \theta_{13}$  for the best fit to T2K  $\nu_e$  appearance data. The data is shown for the normal(top) and inverted(bottom) hierarchy for three flavour oscillations.[34]

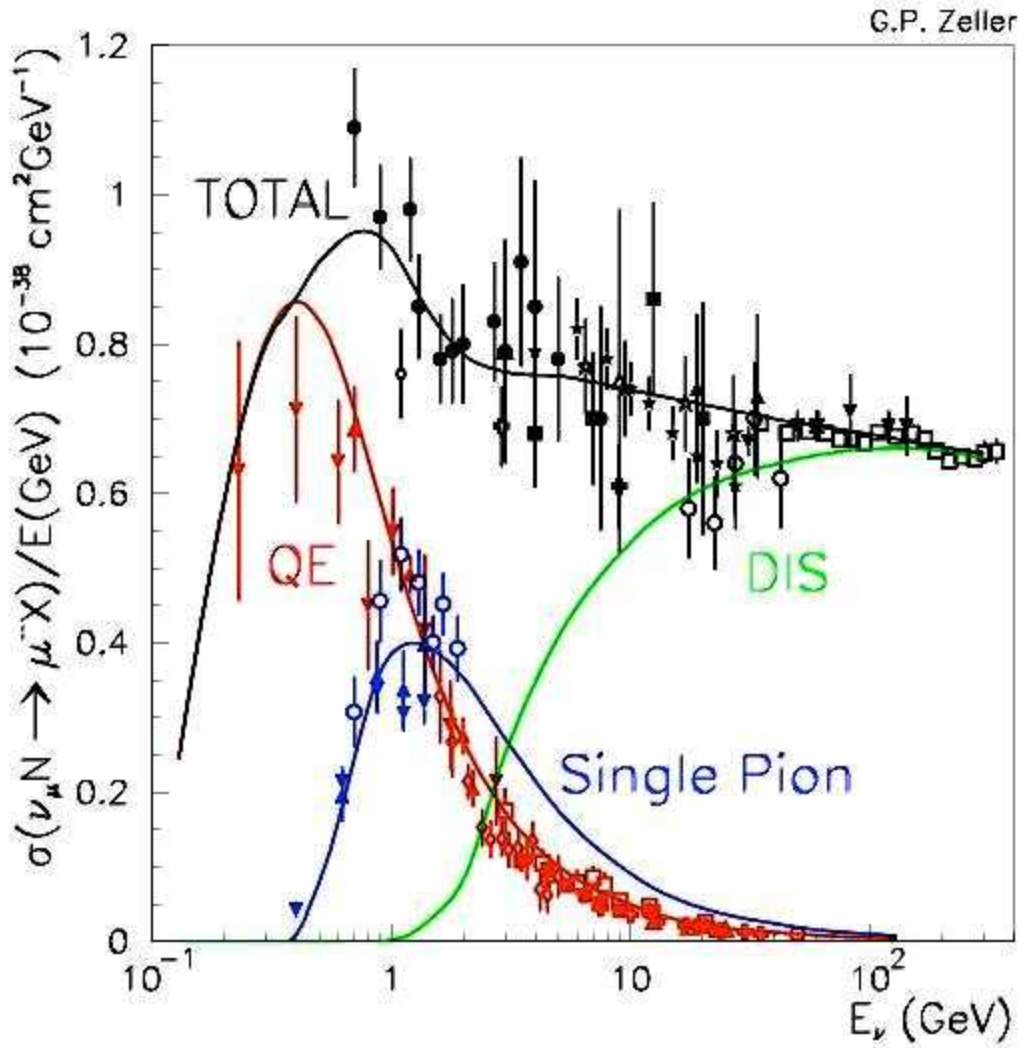


Figure 1.4: An overview of charged current neutrino cross-section over energy measurements (data points) and the NUANCE prediction (solid lines). The data has been corrected to an isoscalar target.[38]

such as NUANCE[39] and NUWRO[40]. T2K uses GENIE[41] and NEUT[42] to produce neutrino interactions for MC data sets. This thesis focusses on the NEUT generator used to produce the MC data sets in the final analysis.

### 1.5.1 Charge Current Quasi-Elastic Interactions

CCQE interactions are the dominant process at T2K energies and are the signal channel for oscillation analyses. They are also the simplest interaction, with a lepton and nucleon in both the initial and final states. CCQE interactions are only possible when a neutrino interacts with a neutron in the process  $\nu n \rightarrow l^- p$ . The Feynman diagram for such interactions is shown in Figure 1.5.

In NEUT, CCQE scattering is modelled using the Llewellyn-Smith cross-section equation[43]:

$$\frac{d\sigma}{dQ^2} = \frac{M^2 G_F \cos^2 \theta_C}{8\pi E_\nu^2} (A(Q^2) \pm B(Q^2) \frac{s-u}{M^2} + C(Q^2) \frac{(s-u)^2}{M^4}) \quad (1.14)$$

where  $E_\nu$  is neutrino energy,  $M$  is the mass of the nucleon,  $s$  and  $u$  are the Mandelstam variables and  $\theta_C$  is the Cabibbo angle. The three coefficients  $A$ ,  $B$  and  $C$  are given in terms of two vector form factors and one axial form factor. The vector form factors can be related to the electromagnetic form factors using the conservation of vector current. This allows the vector form factors to be parametrised in terms of the vector mass,  $m_v$ , that has been previously measured by electron scattering experiments[44]. This leaves the axial form factor  $F_A$  as the only unknown parameter. In NEUT,  $F_A$  is assumed to have a dipole form:

$$F_A(Q^2) = -\frac{1.23}{(1 - \frac{Q^2}{M_A^2})^2} \quad (1.15)$$

where  $M_A^2$  is the quasi-elastic axial mass. The value of the axial mass is tuned by fits to previous neutrino cross-section measurements. The value set in NEUT is  $M_A = 1.21 \text{ GeV}$

### 1.5.2 Charged Current, Neutrino Induced Pion Production

There are two main methods of single pion production to consider. The dominant process is resonant pion production. Here, a neutrino interacts with a bound nucleon with enough momentum transfer to create a resonant nucleon state. This resonance state then decays

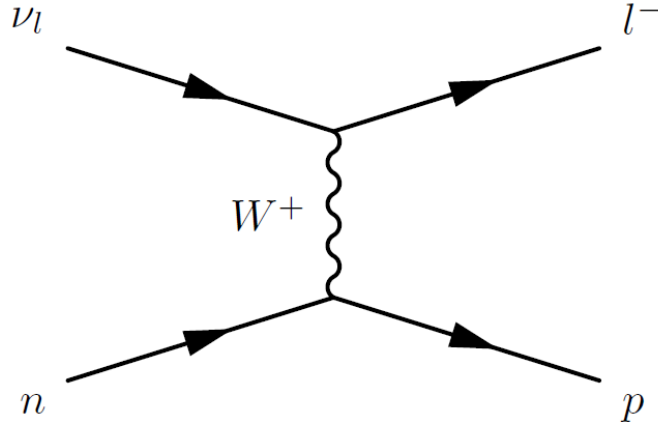


Figure 1.5: Feynman diagram for the charged current quasi-elastic neutrino-nucleon interaction

into a nucleon and a pion. Feynman Diagram for such a process is shown in Figure 1.6.

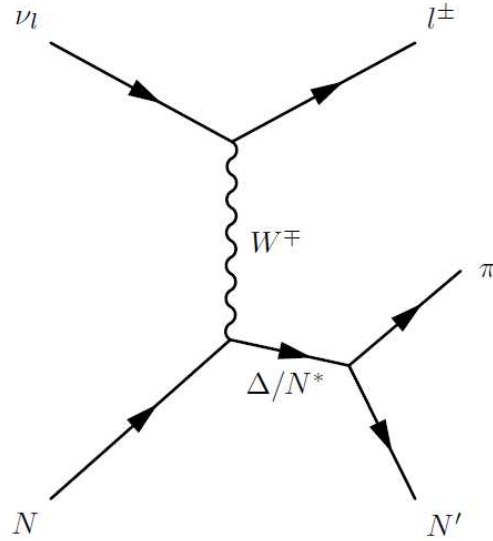


Figure 1.6: Feynman diagram for the charged current resonant pion production

NEUT uses the Rein-Seghal model to simulate this interaction mode[45]. In this model, the cross-section for resonant single pion production is separated into two parts. Firstly the production of the nucleon resonance,  $N^*$  in the process  $\nu + N \rightarrow l + N^*$ . Secondly, the



decay of that resonance to a pion and nucleon,  $N^* \rightarrow \pi + N'$ .

The amplitude for creating each resonance is calculated using the Rein-Seghal model and multiplied by the probability that the resonance will decay to a single pion and nucleon. NEUT considers 18 nuclear resonances with invariant mass below 2 GeV when calculating the single pion production cross-section.

In the Rein Seghal model, the transition amplitude for the creation of the nuclear resonance  $N^*$  from nucleon  $N$  is given by the charged current Lagrangian and Feynman rules as:

$$T(\nu N \rightarrow l N^*) = \frac{g^2 \cos \theta_c}{8} [\bar{l} \gamma^\mu (1 - \gamma^5) \nu_\mu] \frac{g_{\mu\nu} - \frac{q_\mu q_\nu}{M_W^2}}{q^2 - M_W^2} \langle N^* | J^\mu | N \rangle \quad (1.16)$$

where  $\theta_c$  is the Cabibbo angle,  $q^\mu$  is the four-momentum of the W boson,  $M_W$  is the W mass. For  $q^2 \ll M_W^2$  and using the Fermi constant  $G_F = \frac{\sqrt{2}g^2}{8M_W^2}$ , this simplifies to:

$$T(\nu N \rightarrow l N^*) = \frac{G_F \cos \theta_c}{\sqrt{2}} [\bar{l} \gamma^\mu (1 - \gamma^5) \nu_\mu] \langle N^* | J^\mu | N \rangle \quad (1.17)$$

The hadronic current operator  $J^\mu$  is composed of vector and axial components and can be written as:

$$J^\mu = V^\mu - A^\mu = 2M(F_V^\mu - F_A^\mu) \quad (1.18)$$

where we factor out the resonance mass  $M$ . Each factor  $F_{V,A}$  is proportional to a form factor  $G_{V,A}(q^2)$ . The form factors are assumed to have the form:

$$G_{V,A}(q^2) = \left(1 - \frac{q^2}{4m_N^2}\right)^{\frac{1}{2}-n} \left(\frac{1}{1 - \frac{q^2}{m_{V,A}^2}}\right)^2 \quad (1.19)$$

where  $m_{V,A}$  are parameters with units of mass that must be obtained empirically and  $n$  is an ad hoc factor introduced to fix unphysical aspects of the model related to time-like excitations. These parameters are known as the axial and vector masses and are the two free parameters in the resonant pion production cross-section. These two variables therefore, are those used to tune the pion production cross-section.

The cross-section for the production of a single resonance with mass  $M$  and negligible

width is written

$$\frac{d\sigma}{dq^2 dE} = \frac{1}{64\pi m_N E_\nu^2} \sum_{spins} |T(\nu N \rightarrow l N^*)|^2 \delta(W^2 - M^2) \quad (1.20)$$

where  $W$  is the observed invariant mass of the resonance. We replace the delta function with the Breit-Wigner factor to write the cross-section for a resonance of finite width  $\Gamma$ , giving

$$\frac{d\sigma}{dq^2 dE} = \frac{1}{64\pi m_N E_\nu^2} \sum_{spins} |T(\nu N \rightarrow l N^*)|^2 \frac{1}{2\pi} \frac{\Gamma}{(W - M)^2 + \frac{\Gamma^2}{4}} \quad (1.21)$$

The cross-section for resonant production is then given by the sum of the cross-sections for the 18 resonant states and their interferences. To obtain the total transition amplitudes, accounting for the interference, we first decompose the final states using the Clebsch-Gordan coefficients:

$$|\pi^+ p\rangle = |1, 1\rangle \otimes |\frac{1}{2}, \frac{1}{2}\rangle = |\frac{3}{2}, \frac{3}{2}\rangle \quad (1.22)$$

$$|\pi^+ n\rangle = |1, 1\rangle \otimes |\frac{1}{2}, -\frac{1}{2}\rangle = \frac{1}{\sqrt{3}} |\frac{3}{2}, \frac{1}{2}\rangle + \sqrt{\frac{2}{3}} |\frac{1}{2}, \frac{1}{2}\rangle \quad (1.23)$$

For each final state, only contributing resonances with the same total angular momentum,  $j$ , can interfere. The  $\pi^+ p$  final state can only arise from the decay of an isospin  $\frac{3}{2}$ ,  $\Delta^+$ . In this case there is no interference as each  $\Delta^+$  resonance must each have distinct total angular momentum. Therefore, the total transition amplitude is

$$\begin{aligned} |T(\nu_\mu \rightarrow \mu^- \pi^+ p)|^2 &= |\sum_{j=1,3} T(\Delta_{0,1}^+)|^2 + \sum_{j=1,3} |\sum T(\Delta_{1,j}^+)|^2 \\ &+ \sum_{j=3,5} |\sum T(\Delta_{2,j}^+)|^2 + \sum_{j=5,7} |\sum T(\Delta_{3,j}^+)|^2 \end{aligned} \quad (1.24)$$

The  $\pi^+ n$  final state has both isospin  $\frac{3}{2}$  and isospin  $\frac{1}{2}$  components and so  $\Delta^+$  and  $N$  resonances with the same total angular momentum will interfere. Using the coefficients

given above, the total transition amplitude can be written as:

$$\begin{aligned}
 |T(\nu_\mu \rightarrow \mu^- \pi^+ p)|^2 = & \left| \sqrt{\frac{1}{3}} \sum T(\Delta_{0,1}^+) + \sqrt{\frac{2}{3}} \sum T(N_{0,1}^+) \right|^2 \\
 & + \sum_{j=1,3} \left| \sqrt{\frac{1}{3}} \sum T(\Delta_{1,j}^+) + \sqrt{\frac{2}{3}} \sum T(N_{1,j}^+) \right|^2 \\
 & + \sum_{j=3,5} \left| \sqrt{\frac{1}{3}} \sum T(\Delta_{2,j}^+) + \sqrt{\frac{2}{3}} \sum T(N_{2,j}^+) \right|^2 \\
 & + \sum_{j=5,7} \left| \sqrt{\frac{1}{3}} \sum T(\Delta_{3,j}^+) + \sqrt{\frac{2}{3}} \sum T(N_{3,j}^+) \right|^2
 \end{aligned} \tag{1.25}$$

where  $i/2, j/2$  from  $\Delta_{i,j}(N_{i,j})$  represent orbital angular momentum and spin respectively.

Finally, the decay amplitude section of the cross-section is calculated as having three separate contributions. The first is an approximately normalised Breit-Wigner factor accounting for the resonance width. A second factor that is the branching ratio of the resonance to the final state in question. Finally a pure sign factor is applied to ensure interference is calculated correctly. The sign of the decay amplitude is lost when using the experimental Breit-Wigner factor, it must therefore be added manually. Therefore, the transition amplitude for each resonance is given by,

$$T(N^*) = T((\nu N \rightarrow l N^*) \eta(N^* \rightarrow \pi^+ N)) \tag{1.26}$$

where  $N^*$  is the resonance in question,  $N$  is a nucleon and  $\eta$  is the decay amplitude.

Sub-dominant coherent pion production is also modelled in NEUT. In resonant pion production, the neutrino interacts with a single nucleon. Here, the neutrino coherently interacts with the target nucleus as a whole, producing a pion and charged lepton and leaving the nucleus in a final state identical to its initial state. Coherent interactions typically have low momentum transfer and produce the pion and lepton at low angles to the neutrino momentum, i.e. forward going in the lab frame. Coherent pion production in NEUT is modelled using a revised Rein-Seghal model[46].

### 1.5.3 Nuclear Re-Interactions

Many previous cross-section measurements were performed on low-mass targets in bubble chambers. These experiments suffered from relatively poor statistics due to the low interactions rates given by light targets. Modern experiments use heavier nuclear targets to obtain the high statistics necessary for precision measurement. However, the increase in the size of the nucleus means that nuclear effects become important in measuring cross-sections. The interaction cross-sections of a pion with the nuclear medium are large and dominated by low energy QCD processes. The QCD equations to describe the interactions do not have analytic solutions and so nuclear models must be used.

NEUT models the nuclear medium as a relativistic Fermi gas. The initial position of the pion (or other interaction particle) is set according to the Woods-Saxon nucleon density distribution. The pion is then stepped through the nuclear medium in what is called the cascade model. The interaction at each step is calculated using the mean free path of each interaction type. The types of interaction considered in NEUT are: inelastic scattering, charge exchange, pion absorption and pion production. NEUT uses the Oset model[47] to calculate the mean free paths of these interactions. The direction and momentum of pions after scattering and charge exchange are calculated based on the results from pion-nucleon scattering experiments[47]. The scattering amplitude takes into account the Pauli blocking by requiring the scattered nucleon momentum to be greater than the Fermi surface momentum. The probability of each interaction per step is shown in Figure 1.7

The effect of the nuclear medium on the  $\Delta$  width is also calculated. Furthermore, 20% of  $\Delta$  resonances are assumed to decay without producing a pion due to the effects of the nuclear medium. This has a large migration effect between the  $CC1\pi^+$  and CCQE samples as a pionless decay resonant event will appear to be a CCQE event in the detector.

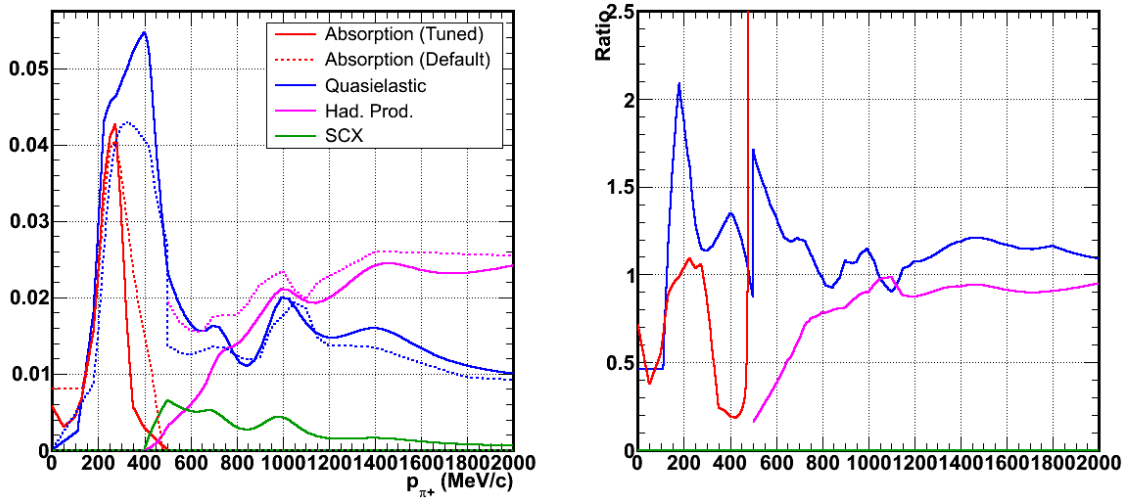


Figure 1.7: Left) The interaction probability per cascade step for a pion at the centre of a Carbon-12 nucleus as a function of momentum. The dotted lines show the NEUT default and the solid lines show the tuned probabilities used in the T2K implementation. The label SCX denotes 'Single Charge eXchange' Right) The ratio of the tuned over default probabilities as a function of pion momentum using the same label colour scheme. Taken from [48]

## Chapter 2

# The T2K Experiment

### 2.1 Experiment Overview

The T2K experiment is the first in a new generation of high luminosity neutrino oscillation experiments. The  $\nu_\mu$  beam for the experiment is provided by the J-PARC (Japan Proton Accelerator Research Complex) located in Tokai-mura, Japan. Here, a 30 GeV proton beam is fired at a graphite target with a design, incident power of 750 kW. This provides the large neutrino flux required for precision neutrino oscillation measurements.

T2K is a Long Baseline neutrino experiment and so measures the profile of the neutrino beam in two places. The ND280 (Near Detector 280 m) suite forms the near detector and will measure the neutrino beam before oscillations have occurred. ND280 is comprised of the on-axis INGRID (Interactive Neutrino Grid) detector and the off-axis ND280 Detector. These detectors are situated 280 m from the graphite target used to produce the neutrino beam in order to allow the initial products of the beam interactions to decay into neutrinos. The INGRID detector provides precision monitoring of the beam centre and width, whilst the ND280 detector profiles the energy spectrum and flavour composition of the neutrino beam before any oscillation has occurred. The far detector is the water Čerenkov detector, Super-Kamiokande (Super-K) in Kamioka on the west coast of Japan. This gives T2K a baseline of 295 km. Super-Kamiokande will profile the neutrino beam after oscillations have occurred. A simple illustration is provided in Figure 2.1

The ND280 detector and Super-Kamiokande are placed  $2.5^\circ$  from the beam axis. This reduces the neutrino flux but also gives a narrow band peak in the neutrino energy spectrum



Figure 2.1: An overview of the T2K baseline

around 0.7 GeV; at this neutrino energy there will be maximal mixing in the atmospheric sector for a baseline of 295 km. This makes T2K sensitive to  $\nu_\mu$  disappearance in the beam, thus allowing it to achieve one of its primary physics goals of producing precise measurements of the  $\Delta m_{23}^2$  and  $\sin^2\theta_{23}$  oscillation parameters. The T2K predicted flux is shown in Figure 2.2. T2K is also sensitive to the less frequent  $\nu_e$  appearance, due to the high neutrino flux and well understood far detector. Furthermore, the off-axis technique also greatly reduces the high energy tail in the neutrino spectrum and thereby suppresses one of the major backgrounds to this measurement at Super-Kamiokande. This sensitivity is necessary for T2K to achieve its other physics goal of precisely measuring, the much smaller  $\theta_{13}$  mixing angle. Furthermore, with recent measurements of large  $\theta_{13}$ , T2K should have sufficient sensitivity to search for the CP-violating phase  $\delta$ .

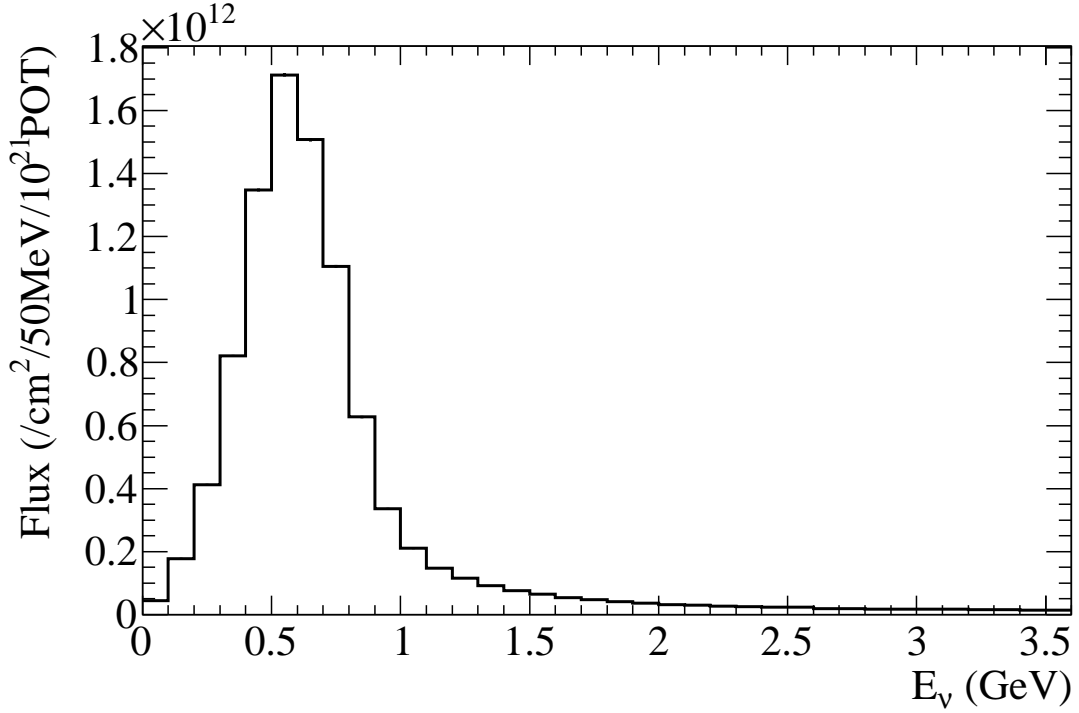


Figure 2.2: The POT weighted,  $\nu_\mu$  flux prediction at ND280 integrated over Run 1 and Run 2.

## 2.2 The J-PARC Accelerator Complex and the T2K Beamline

J-PARC consists of three accelerators, a linear accelerator (LINAC), rapid-cycling synchrotron (RCS) and a 30 GeV Main Ring synchrotron (MR). The LINAC accelerates a  $H^-$  beam to 181 MeV kinetic energy. The  $H^-$  beam is then stripped of its electrons to give a proton beam upon injection into the RCS where it is further accelerated to 3 GeV. The proton beam is then injected into the MR where it is accelerated to 30 GeV. The protons are then fast extracted to the neutrino beamline using 5 kicker magnets. The protons are supplied to the neutrino beamline in 5 ns wide spills, each composed of eight proton bunches (6 bunches for Run 1). The neutrino beamline consists of a primary and secondary beamline and is illustrated in Figure 2.3

The primary beamline first tunes the proton beam using a series of 11 normal conducting magnets before using 14 superconducting magnets to bend the beam through an angle of  $80.7^\circ$  to point towards Kamioka. Finally, 10 normal conducting magnets are used to



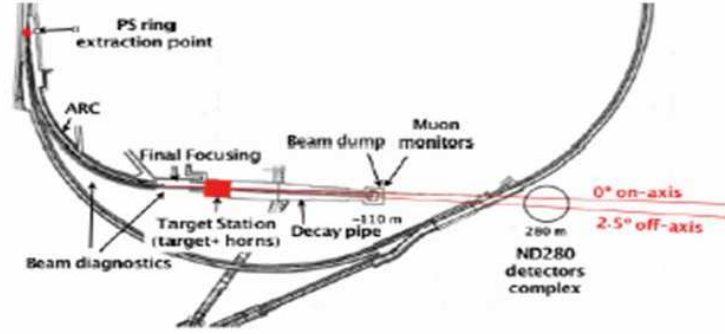


Figure 2.3: An overview of the T2K beamline

direct the beam towards the neutrino target. The neutrino target is a graphite cylinder 91.4 cm (1.7 radiation lengths,  $X_0$ ) long, 2.6 cm in diameter and is cooled by high pressure helium gas.

The secondary beamline starts at the neutrino target. The proton beam interacts with the target producing secondary pions and a small number of secondary kaons. The target is surrounded by the first of three magnetic horns to collect the secondary hadrons produced by the beam interactions. The hadrons are then focused by the two further horns as they travel through the 110 m decay volume. The horns produce a toroidal magnetic field at a maximum of 2.1 T. When operating at a current of 320 kA, the horns increase the neutrino flux at Super-Kamiokande by a factor of 16 compared to 0 current operation. The horns can operate to select either positive or negative hadrons, creating a neutrino or anti-neutrino beam respectively. The decay volume length was selected to minimise muon decay whilst maximising pion decay and is filled with Helium gas at 1 atm to minimise pion-nucleus interactions.

The vast majority of pions decay in flight via the weak interaction,  $\pi^+ \rightarrow \mu^+ \nu_\mu$ , providing the beam neutrinos. However, some of the muons will also decay in flight via  $\mu^+ \rightarrow e^+ \nu_e \bar{\nu}_\mu$ , adding small  $\nu_e$  and  $\bar{\nu}_\mu$  contamination to the beam. The beam is also contaminated by  $\nu_e(\bar{\nu}_e)$  from the secondary kaons that decay in the decay volume. The secondary beamline terminates in the water cooled, graphite, beam dump which is designed to absorb the remaining hadrons and any muons below 5 GeV. Situated just behind the beam dump is the muon monitor. The muon monitor uses the  $> 5$  GeV muons to precisely

measure the beam position and intensity. Figure 2.4 shows a schematic of the secondary beamline. Further downstream, a nuclear emulsion detector is used to measure the absolute muon flux and momentum distribution.

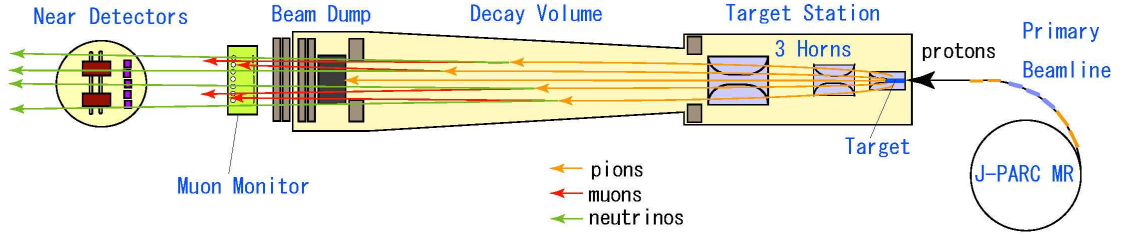


Figure 2.4: Schematic of the secondary neutrino beamline

### 2.3 The Far Detector : Super-Kamiokande

Super-Kamiokande is a 50 kt water Čerenkov detector located 1 km deep inside Mount Ikenoyama, Japan. Super-Kamiokande has two co-axial, cylindrical volumes forming an inner detector (ID) and an outer detector (OD). A pictorial representation of the detector can be found in Figure 2.5 The outer detector is instrumented by 1,885, 20 cm PMTs (Photomultiplier Tubes) and is used as a veto to reject events originating outside of the detector. The inner detector contains 11,129 50 cm, PMTs facing inwards. The PMTs are mounted on a scaffold that separates the detector volumes. The scaffold is covered in plastic sheets to optically separate the two detector volumes. The inner surface is covered in black sheeting to absorb light and stop light crossing the detector boundary. The outer surface of the scaffold is lined with a highly reflective material to compensate for the sparse readout coverage of the outer detector.

A highly relativistic particle may exceed the effective speed of light for the medium through which it is travelling. If the particle is electrically charged it will polarise the medium along its trajectory. When the medium depolarises it will emit photons in a cone around the particle's path. The opening angle of the cone ( $\theta$ ) is dependent on the particle's speed ( $\beta$ ) and the material's refractive index ( $n$ ) as shown in Equation 2.1. Water has  $n = 1.34$  and so a particle must have velocity above the threshold  $\beta > 0.75$  to emit

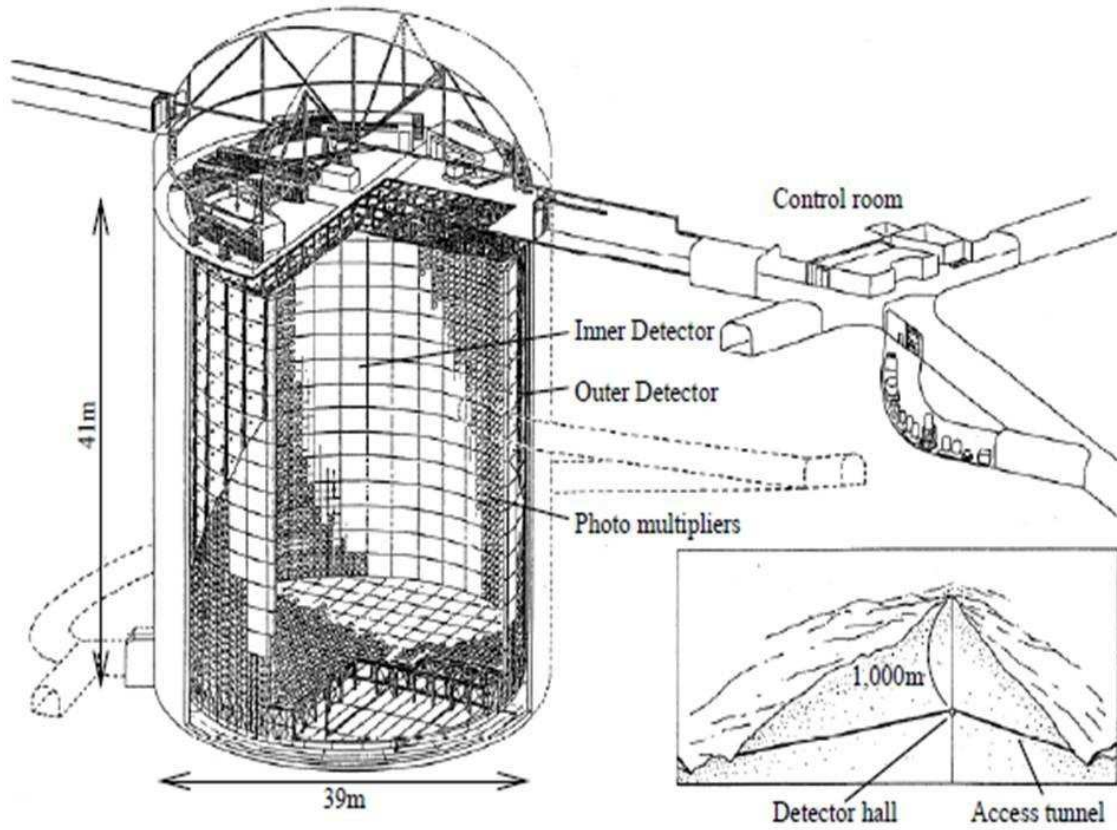


Figure 2.5: The Super-Kamiokande detector layout showing the inner and outer detectors. The two detectors are separated by a cylindrical scaffold that is used to mount PMTs

Čerenkov Radiation in Super-Kamiokande.

$$\cos \theta = \frac{1}{\beta n}, \beta > \frac{1}{n}, \quad (2.1)$$

The light cone will project a circular pattern onto the detector wall which will be seen as a ring like pattern of hits in the PMTs. The width of the ring and the timing of the hits can then be used to determine the particle's momentum and the event vertex position.

The shape of the rings observed in the inner detector can be used to separate the different particle types produced in neutrino interactions at Super-Kamiokande. Muons and pions tend to pass through the detector with only minimal scattering and so produce a very sharp clean ring. These sharp rings are tagged as being  $\mu$  - like. Electrons will almost always scatter multiple times and shower. The ring observed in the detector will be blurred as

the shape and angle of the light cone changes with each scattering. A 'fuzzy' ring will be produced by the superposition of the many light cones, this pattern is then tagged as  $e - like$ . Event displays showing the difference between muon and electron events are shown in Figure 2.6. Protons from neutrino interactions in Super-Kamiokande are usually created with velocities below threshold and so are not observed. There is no way to extract charge information from the Čerenkov light and so Super-Kamiokande cannot distinguish neutrinos and anti-neutrinos.

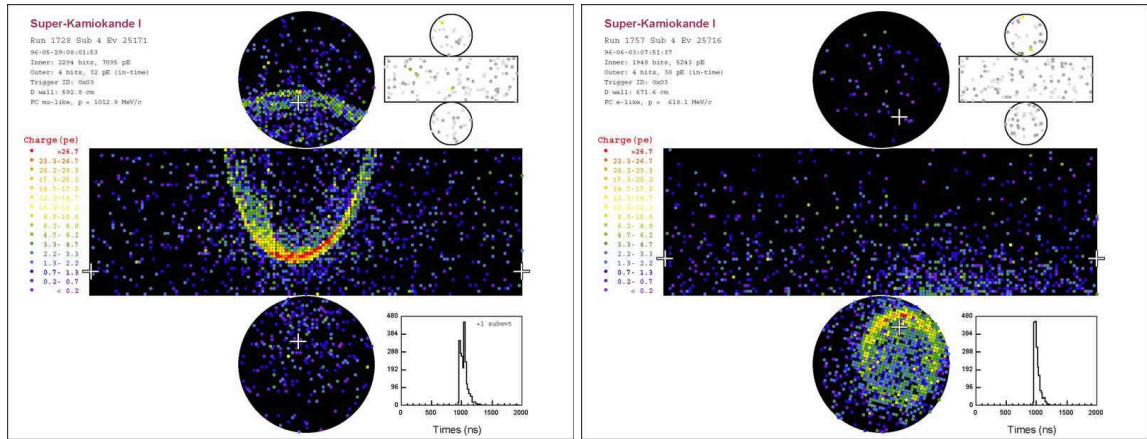


Figure 2.6: Event displays showing neutrino events in Super-Kamiokande . The left display shows a single ring  $\nu_\mu$  event. The right shows a single ring  $\nu_e$  event. The ring from the muon event is much more well-defined than that in the electron event.

### 2.3.1 The Neutrino Beam at Super-Kamiokande

Super-Kamiokande measures the flavour composition of the beam by counting the number of Charged Current Quasi-Elastic (CCQE) neutrino interactions observed. In a CCQE event, the neutrino interacts to produce a lepton of the same flavour and a recoil nucleon. The recoil nucleon does not usually exceed the Čerenkov threshold and so passes undetected. The lepton will leave a single ring signal in the detector. By selecting these single ring events a sample of CCQE-like events can be created. Neutral Current (NC) interactions do not produce leptons and so cannot be used to determine the flavour composition of the beam. They can however be used to measure the total neutrino flux passing through the detector.

An initial selection of Fully Contained, Fiducial Volume (FC, FV) events is created.

The FV is a cylinder 200 cm from the inner detector walls and contains a fiducial mass of 22.5 kt, in order to be selected, the event vertex must be reconstructed within this fiducial volume. A FC event is one that deposits at least 30 MeV visible energy in the ID and has no event activity in either the OD or in the 100  $\mu$ s before the event trigger. The selected event must also fall within the beam trigger window. Single ring events are then selected from this FCFV sample. PID is applied to these single ring events to select  $\nu_\mu$  or  $\nu_e$  interactions. Further cuts are implemented to enrich the samples depending on the neutrino flavour being measured.

The main background to the  $\nu_\mu$  CCQE measurement is charged current single pion production ( $\text{CC}1\pi^+$ ).  $\text{CC}1\pi^+$  events can produce a single ring, CCQE-like signal when the pion is created below Čerenkov threshold and so not observed. This then skews the muon momentum distribution and distorts the reconstructed neutrino energy. This background can be mitigated somewhat by searching for a Michel electron produced in the pion decay but this does not remove the background fully. A precise measurement of the  $\text{CC}1\pi^+$  differential cross section on water will be made at the near detector to calculate and remove this background.

## 2.4 The INGRID Detector

INGRID is part of the near detector suite, 280m from the neutrino target station and is comprised of 16 identical modules. Each module is a  $1\text{m}^3$ , 7-ton, iron/scintillator sandwich with 11 layers of 25 plastic scintillator bars and 65 mm thick layers of iron. In order to reject cosmic and out-of-detector events, each module is surrounded by four veto, scintillator planes. 14 of the modules are arranged in 10 m vertical and horizontal arrays (perpendicular to the beam direction) forming a cross centred on the beam. The final 2 modules are placed on opposing corners of the cross shape as shown in Figure 2.7.

The primary purpose of the INGRID detector is to profile the beam shape and centre and measure the on-axis neutrino flux on a daily basis. The high target mass of the modules gives the high number of interactions required to measure the beam on such time scales. INGRID exceeds the target accuracy of detecting beam deviations to the order of 1 mrad[23] as shown in Figure 2.8



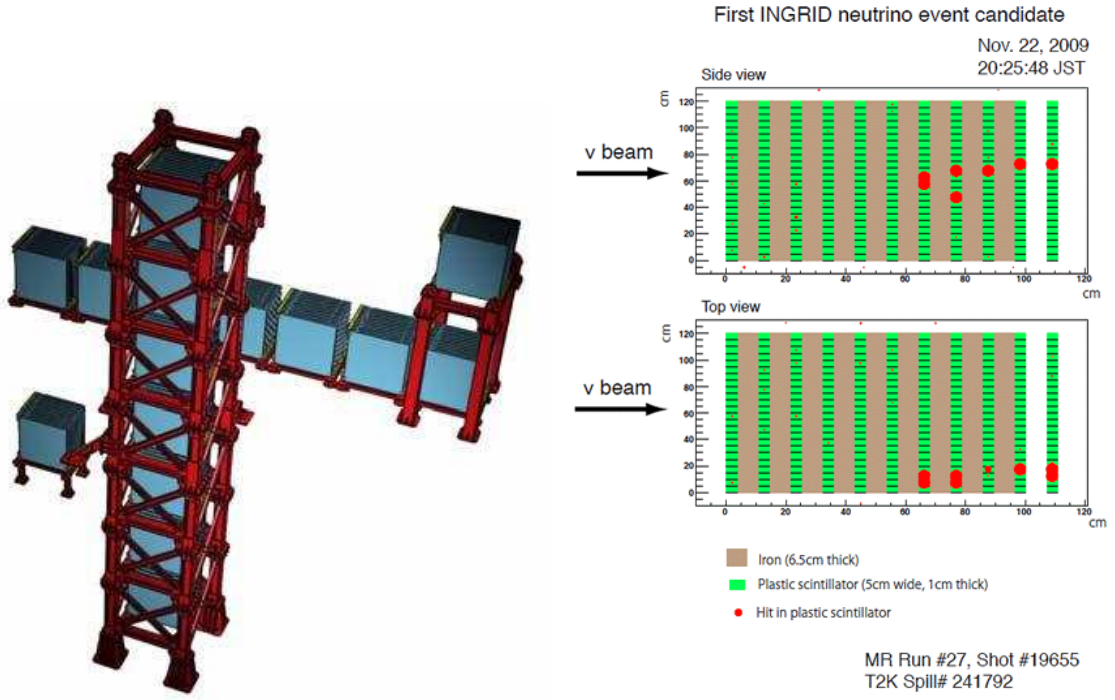


Figure 2.7: The left shows the layout of the INGRID modules. The right hand image shows an event display of the first T2K neutrino event observed in the detector.

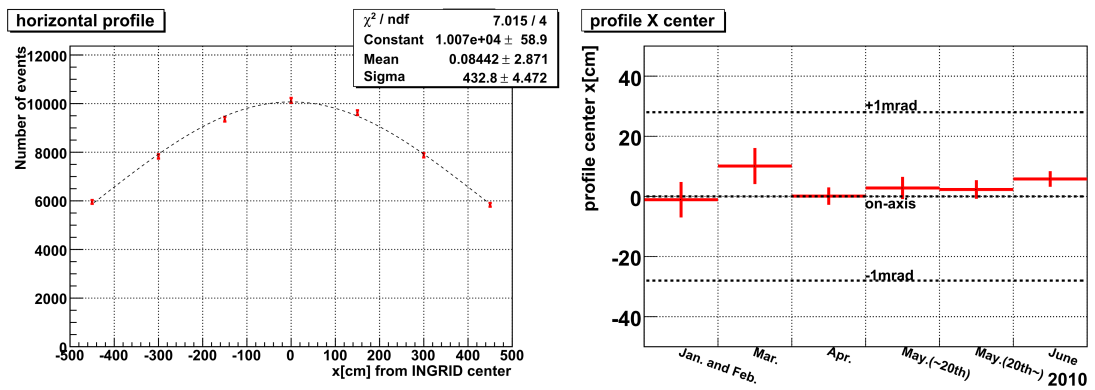


Figure 2.8: Left: The horizontal beam profile as measured by INGRID. Right: A plot showing how the beam centre varies with time

## 2.5 The ND280 Detector

The off-axis near detector is a magnetised, fine grained, all purpose neutrino detector designed to measure the flux, energy spectrum and flavour content of the beam heading to the far detector as well as measuring neutrino interaction cross-sections. The near detector must measure both the  $\nu_\mu$  and  $\nu_e$  fluxes. The  $\nu_\mu$  flux measurement will be used to predict the flux at the far detector for the  $\nu_\mu$  disappearance measurement. The  $\nu_e$  contamination of the beam forms an irremovable background to the  $\nu_e$  appearance measurement at Super-Kamiokande.

ND280 is comprised of several sub-detector systems contained within a 0.2 T magnet. The inner region of the detector is mounted in a  $6.5m \times 2.6m \times 2.5m$  basket. The most upstream detector in this basket is the  $\pi^0$  detector (P0D). Downstream from this is the tracker containing three time projection chambers (TPC) interspersed with two, scintillator based, fine grained detectors (FGD). The final most downstream detector within this basket is the downstream electromagnetic calorimeter (DsECal). The P0D and tracker regions are surrounded by electromagnetic calorimeters (ECal) mounted on the refurbished UA1 magnet. A muon range detector (SMRD) is mounted within the air gaps between the flux returns of the magnet yoke. A figure of the ND280 detector is shown in Figure 2.9

### 2.5.1 The $\pi^0$ Detector

The P0D region of ND280 is optimised to measure  $NC\pi^0$  production on a water target. Accurate measurement of this process will be used to reduce systematic uncertainties in the Super-Kamiokande  $\nu_e$  appearance measurement.

The P0D uses planes of scintillator bars as the active region. This region is fine grained enough to allow reconstruction of charged tracks and electromagnetic showers. The centre of each bar contains a single WLS fibre (Kuraray, double-clad, Y11 wave length shifting fibre. 1 mm diameter) that is readout by a Hamamatsu MPPC (Multi-Pixel Photon Counter). The scintillator bars have a triangular cross-section (33.6 mm base by 17.25 mm height)

At the upstream and downstream ends of the P0D are calorimeter modules consisting of alternating 4 mm thick lead sheets and scintillator P0Dules. Each scintillator P0Dule is formed of two layers with the bars aligned in perpendicular arrays along the x and y

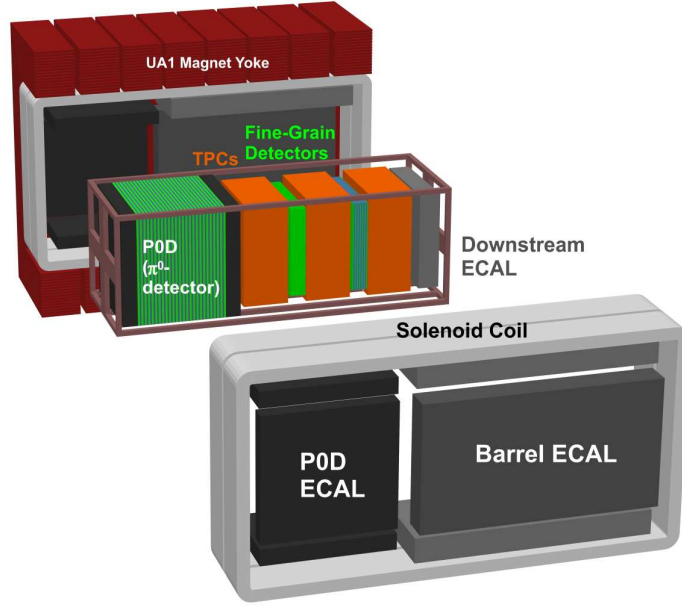


Figure 2.9: An exploded diagram of the ND280 detector showing each subsystem

directions. These areas are designed to contain the electromagnetic showers and form a veto for events entering from outside the P0D volume. The layout of the P0D is shown in Figure 2.10. In the centre of the P0D is the neutrino target region, two sections of 13 P0Dules separated by pairs of water target bags for a total of 50 water bags in the detector. The P0D can be operated with the water bags filled with air or water. By running in both modes, a subtraction method can be used to determine the interaction cross sections on a water target. The detector mass is 16.1 tons when filled with water and 13.3 tons when filled with air.

### 2.5.2 The Time Projection Chambers (TPC)

The three TPC modules within the tracker provide three-dimensional charged particle tracking, momentum measurement from track curvature and charged particle identification via mean energy loss. Each TPC has an inner box filled with an argon-based drift gas, contained within an outer box filled with  $C0_2$  as an insulating gas. A uniform electric drift field is applied across the TPC volume and is roughly aligned with the ND280 magnetic field. As charged particles travel through the TPC gas, they produce ionisation electrons which are drifted to the readout planes on the detector walls. The electrons are detected in MI-



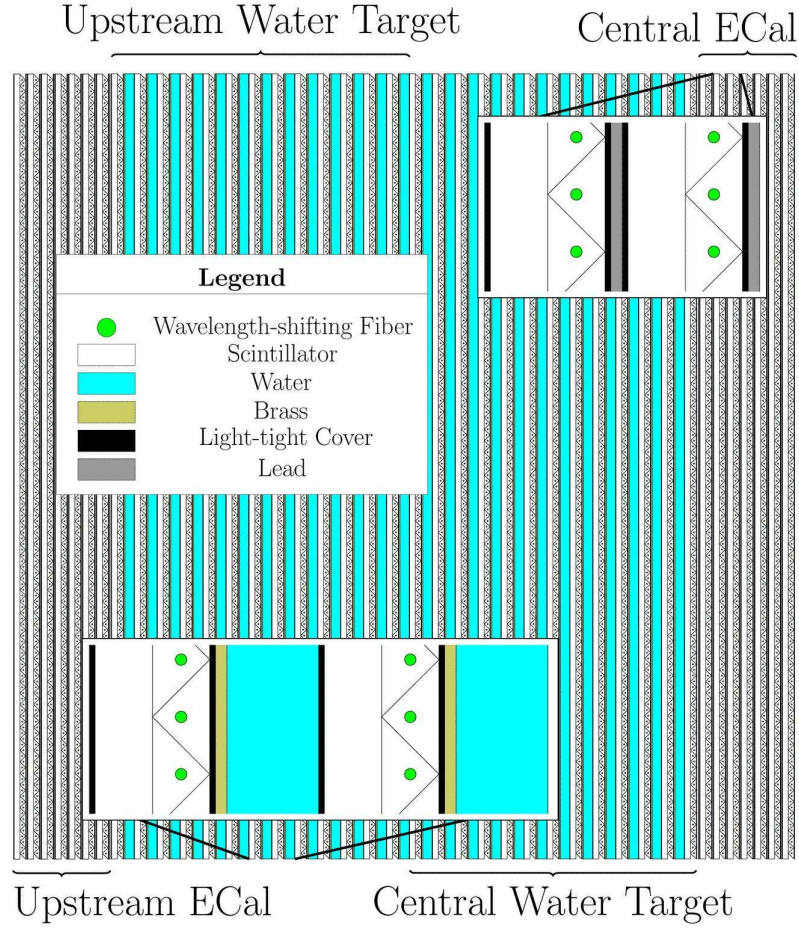


Figure 2.10: A schematic showing the construction of the POD, including diagrams of the Ecal and water PODules

CROMEGAS [49] readout modules, where they avalanche to amplify the original signal. The position of the charge deposit on the readout plane provides two dimensional position information, the third position co-ordinate is calculated from the electron drift time and a timestamp from the surrounding FGDs or ECals.

The particle identification in the TPC uses truncated mean measurements of the energy loss by charged particles in the gas. The linear charge density of the track is estimated using the lowest 70% of values from the track segments. The resolution of the energy loss is 7.8% for minimum ionising particles, which exceeds the design resolution of 10% [50]. Figure 2.11 shows the energy loss vs momentum curves for positive particles traversing the TPC during the first T2K physics run.

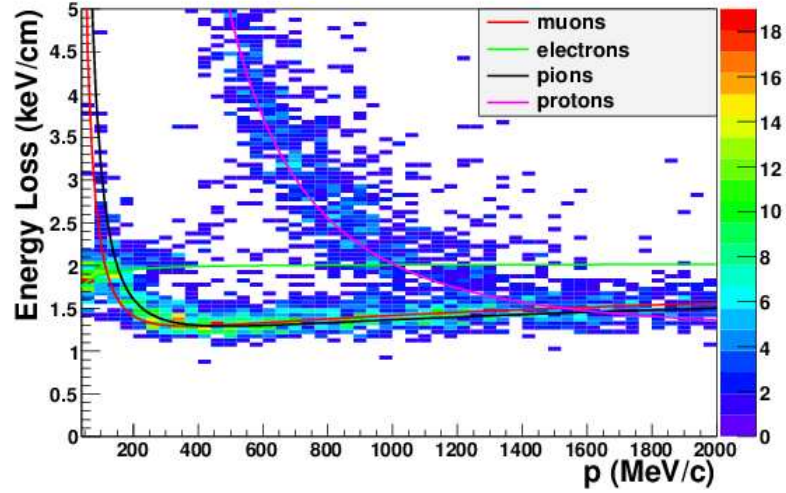


Figure 2.11: Energy loss vs momentum for positive particles produced in neutrino interactions during first T2K physics run. The lines show the Monte Carlo expectations for different particle types.

### 2.5.3 The Fine Grained Detectors (FGD)

The FGDs provide the target mass for the neutrino interactions within the tracker region. The fine grain of the detector allows it to see the low energy particles produced in neutrino interactions, such as the recoil protons and also perform tracking and vertex reconstruction. The two FGDs are placed between the TPC modules. Each FGD has identical dimensions and contain 1.1 tons of target material. The target material is carbon based scintillator in the first FGD and water in the second, this allows the cross sections on water to be measured by comparing the rates in each detector and using a subtraction method.

The first FGD is a pure scintillator detector with 30 layers of scintillator bars (with  $10\text{mm} \times 10\text{mm}$  cross section). The layers are arranged such that they form XY modules of two layers, one layer with the bars aligned horizontally and the other layer with the bars aligned vertically. Each bar has a Y11 WLS fibre passing through its centre. The fibres are read out on one end by an MPPC, the other end is mirrored to maximise light collection.

The second FGD is part water, part scintillator, having only 7 XY modules of plastic scintillator. The scintillator modules are interspaced with 6 layers of water, held within hollow corrugated polycarbonate. The water is at negative pressure so that any leaks will

introduce air into the target region instead of the water leaking out into the surrounding detector.

#### 2.5.4 The Electromagnetic Calorimeters (ECals)

The ECals are lead-scintillator, sampling electromagnetic calorimeters providing near hermetic coverage for the inner detectors. As the name suggests, it's main goal is to make energy measurements of electromagnetic showers. The ECal is necessary in forcing photons to convert and shower, this will be essential to detect  $\pi^0$  particles produced in the tracker. The ECal will also be key in separating muons, pions and electrons. Muons will pass through the ECal as a minimum ionising track whilst electrons will shower. Pions will often look like a combination of the two, travelling as a MIP and then showering.

There are a total of 13 ECal modules in the ND280 detector, 1 downstream module (DsECal), 6 barrel ECal modules (BrECal), and 6 P0D ECal modules (P0DECals). All ECal modules are mounted on the inside of the magnet yoke except for the DsECal, which, occupies the most downstream volume of the basket. The basic design for each module is similar, each module is made of layers of scintillator bars glued to lead sheets. The bars in each layer are orientated at right angles to those of the previous layer to allow full three dimensional reconstruction. The ECals are less fine grained than the other scintillator detectors with the bars having a 40 mm by 10 mm cross section. As with the other detectors, the bars have a Y11 WLS fibre running through the middle.

The DsECal is placed at the most downstream end of ND280 after the final TPC within the basket. It has dimensions  $2m \times 2m \times 0.5m$  and is 34 layers deep in the z (beam) direction. The lead sheets in the module are each 1.75 mm thick giving the module a total thickness of  $10.6X_0$ . The DsECal is the thickest module due to the more lax spatial restrictions and the higher peaked momentum spectrum for forward travelling particles. All of the bars in the downstream module are readout on both ends by an MPPC (double ended readout).

There are a total of 6 BrECal modules that surround the tracker region on four sides and are mounted on the magnet yoke. The bars aligned parallel to the beam direction are 3.84 m long and are also double ended readout to compensate for the effects of the long

bar length. The bars aligned perpendicular to this (in the x or y direction) are 1.52 m (top/bottom modules) or 2.36 m (side modules) long and have single ended readout due to spatial constraints. The barrel modules are 31 layers deep with lead sheets of the same thickness as the DsECal. This gives the barrel modules a total radiation length of  $9.7X_0$ .

The P0DECals surround the POD on four sides and are not designed for full electromagnetic shower reconstruction. Their primary purpose is to detect photons that do not convert in the POD and to tag charged tracks passing through them, acting as a veto. Each of the 6 modules has only 6 layers of scintillator with 5 layers of 4 mm thick lead sheets giving  $3.6X_0$ . Unlike the other ECals, the bars in the P0DECals are all aligned in the z direction and have only single ended readout, limiting the modules to two dimensional reconstruction.

### 2.5.5 The Side Muon Range Detector (SMRD)

The SMRD is a plastic scintillator detector mounted within the magnet yoke. The SMRD serves multiple purposes. It's main physics role is to reconstruct high momentum muon tracks that exit the inner detectors, especially muons travelling at high angles to the z axis which may be poorly reconstructed by the other detectors. The SMRD is also a useful veto for events entering the detector from the outside. Further to this, it acts as a trigger for detecting cosmic rays outside of beam windows. These cosmic rays can then be used for various detector calibrations. By requiring different combinations of SMRD modules to fire you can select different cosmic ray acceptance angles. This is particularly useful for studying rare track topologies, for example, tracks travelling parallel to the x axis. The reconstruction of these rare topologies can then be studied and understood in beam events. An SMRD module is shown in Figure 2.12

The magnet yoke is divided into two halves, each consisting of 8 C-shaped flux return yokes. The SMRD scintillator modules are installed in the air gaps between each yoke. The SMRD scintillator modules are plastic scintillator slabs with an S-shaped groove carved into the surface. A Y11 WLS fibre is glued into the groove and readout by an MPPC. The plastic slabs are then wrapped in lightproof, stainless steel containers.

Figure 2.13 shows an event display of a neutrino interaction in ND280. The neutrino

interacts in the POD producing a high energy particle that traverses the basket producing several secondary particles before showering in the DsECal. This event was taken early in data Run 3 shortly after operations resumed.

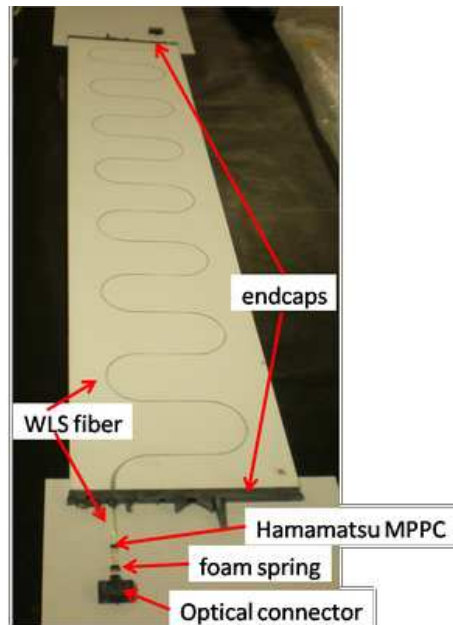


Figure 2.12: An SMRD module before the light tight cover has been mounted.

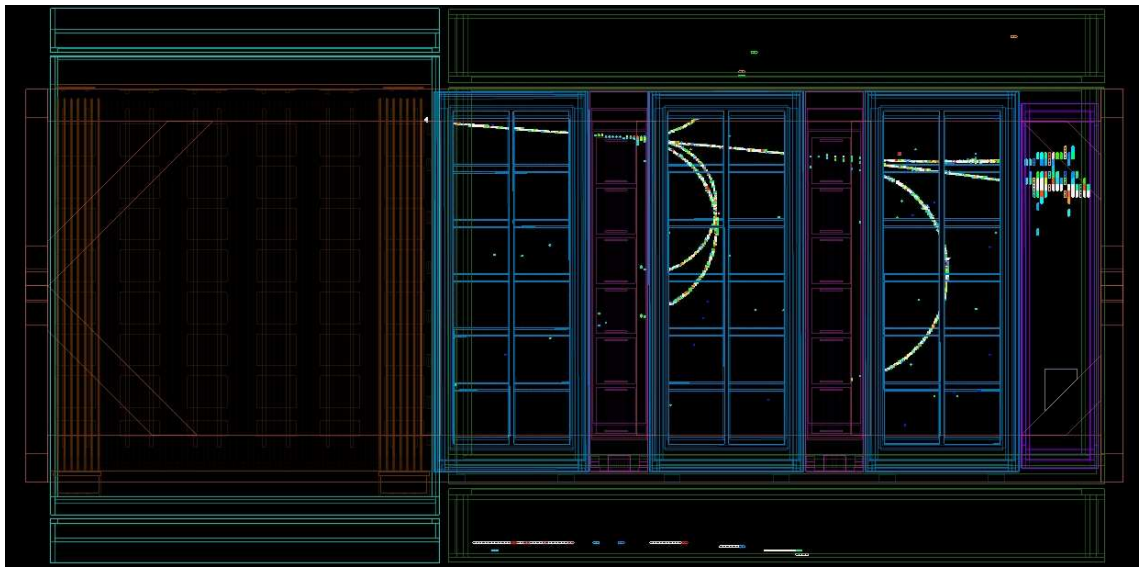


Figure 2.13: An ND280 event display showing a neutrino beam event observed shortly after the start of Run 3 data taking. The Event Display shows an interaction in the P0D volume producing several particles that traverse most detector modules.

## Chapter 3

# Construction of the ND280 Barrel ECal

### 3.1 Calorimeter Detectors

General information regarding the Barrel ECal has already been discussed in Chapter 2, this chapter will focus on the details of the ECal design and construction. The primary purpose of a calorimeter is the absorption and measurement of the energy deposited by particles passing through the detector. In order for the calorimeter to be accurate and efficient it should have sufficient radiation thickness so that particles will interact and deposit most of their energy within the detector volume. This is usually achieved by designing the calorimeter so that primary particles entering the detector will interact creating a 'shower' of secondary particles at lower energy. These secondary particles then create further particles at even lower energy. This process continues until all particles pass below the threshold to produce new particles. During this process some fraction of the primary particle's initial energy will be deposited as visible signal (In the ND280-ECal case, scintillation light) Two types of particle shower can be produced, electromagnetic and hadronic, depending on the type of the primary particle which interacts.

As one might expect, electrons and photons will produce electromagnetic showers. In this case the cascade of shower particles will be produced predominantly via pair production and bremsstrahlung. The shape of the shower is characterised by  $X_0$ , the 'radiation length' of the calorimeter material.  $X_0$  is the length at which an electron will have radiated all but  $1/e$  of it's energy and  $7/9^{th}$  the mean free path for a photon to pair produce. In a simplified model, an electron travelling  $1 X_0$  will emit a bremsstrahlung photon with



roughly half it's energy. Furthermore, a photon travelling  $1 X_0$  will undergo pair production (in this simple model). The number of particles in the shower will double every radiation length until the maximum depth  $t_{max}$ . The  $t_{max}$  is reached when the particles are produced at critical energy, where energy loss per radiation length is equal to the particle's energy. So at  $t_{max}$ , we have,

$$|E(t)| = E_c = E_0/2^{t_{max}}, \quad (3.1)$$

which rearranges to

$$t_{max} = \frac{\ln(E_0/E_c)}{\ln 2} \quad (3.2)$$

This model only qualitatively describes the evolution of an electromagnetic shower. The reality is more complex and requires several corrections, such as, the mean free path of photons before pair production and secondary effects such as scattering and fluctuations in particle production.

Hadronic showers are produced by strongly interacting particles such as pions and protons. Hadronic showers are much more complex than the electromagnetic case. The secondary particles are mostly pions and nucleons, with the number produced being only weakly dependent on the energy of the primary particle. A proportion of the secondary particles are  $\pi^0$  particles which will then propagate electromagnetically without further nuclear interactions. The number of  $\pi^0$ s produced is largely dependent on the first interaction of the primary particle and so large fluctuations occur between showers. Furthermore, a large amount of the energy will be deposited in nuclear breakup and will be mostly unobserved. The fraction of the initial energy deposited in this manner varies randomly between showers as does the fraction that is observed. This makes energy measurements difficult and thus far not possible in the ND280.

The majority of the energy in a hadronic shower is carried by fast, forward going particles whilst a limited amount of energy is carried in the transverse direction. This gives a shape distinct from that of electromagnetic showers.

There are two basic calorimeter designs as shown in Figure 3.1. Homogeneous calorimeters use a single material for shower propagation and readout. This gives them a high precision energy resolution at the cost of position reconstruction. The lack of segmentation



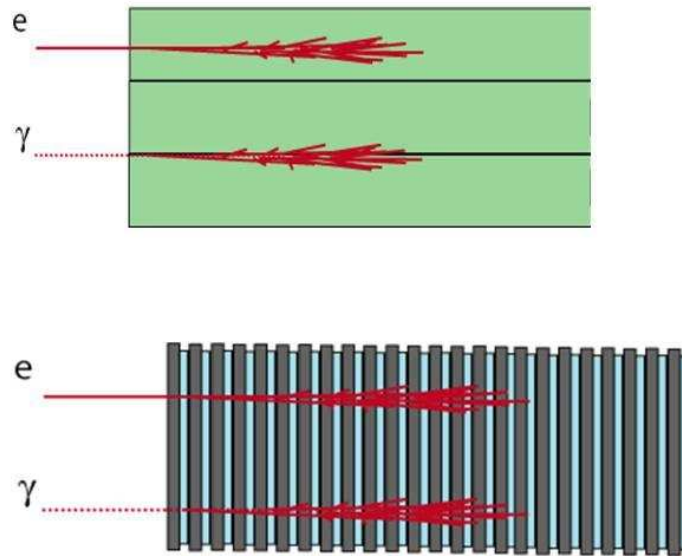


Figure 3.1: A simple diagram depicting a homogeneous (top) and a sampling (bottom) calorimeter

prohibits 3D reconstruction. Homogeneous calorimeters are only practical for electromagnetic showers, the large size of hadronic showers make homogeneous detectors impractical. Furthermore, materials suitable for use as an homogeneous calorimeter are relatively expensive per  $X_0$ .

The ND280 ECal is a sampling calorimeter. A sampling calorimeter is segmented between an absorber material to initiate and develop showers, and an active material to profile the shower as it develops. The ND280 ECal uses a lead absorber and a plastic scintillator active material. The inclusion of the inactive absorber material reduces the energy resolution of the detector. However, the segmentation makes readout easier and allows for 3D reconstruction, sampling calorimeters can then provide some measure of tracking as well.

	DS-ECal	Barrel ECal	P0D ECal
Length	2.3m	4.140m	2.454m
Width	2.3m	1.676m top/bottom 2.503m side	1.584 top/bottom 2.894m side
Layers	34	31	6
Bar orientation	x/y	Longitudinal/Perpendicular	Longitudinal
Bars	1700	2280 Long. top/bottom 1710 Long. sides 6144 Perp. top/bottom 3072 Perp. sides	912 Long. top/bottom 828 Long. sides
Bars per layer	50	38 Long. top/bottom 57 Long. side 96 Perp top/bottom/sides	38 Long. top/bottom 69 Long. sides
Bar length ( $\pm 2mm$ )	2.000m	3.840m Long. 1.520m Perp. top/bottom 2.280m Perp. sides	2.340m Long.
Fibre length ( $\pm 0.5mm$ )	2.144m	3.986m Long. 1.583m Perp. top/bottom 2.343m Perp. sides	2.410m Long.
Pb thickness	1.75mm	1.75mm	4.0mm

Table 3.1: ECal module design dimensions. Longitudinal bars are those whose long axis lies parallel to the beam direction.

## 3.2 Detector Design

### 3.2.1 Geometry and Dimensions

Six Barrel ECal modules surround the inner tracking region of ND280. The two largest modules are mounted at the sides of the tracker and four smaller modules are mounted above and below. Four smaller modules are used so that the two halves of the magnet may be opened. Table 3.1 gives a complete overview of the design dimensions for the ECal modules.

All scintillator bars have a cross section of  $40mm \times 10mm$ . Each bar has a 2 mm central hole with a WLS fibre inserted into it. The WLS fibre is required due to the short attenuation length of the scintillator, without the WLS fibre, significant signal loss would occur as the scintillation light travelled along the bar to the sensor. The WLS fibre also

shifts the wavelength of all light towards the green band of the spectrum, near the region of peak sensitivity for the MPPCs. An MPPC is attached to one or both ends of the fibre as a readout. Each MPPC is attached to a channel on a Trip-T Front-end Board (TFB) via a mini-coaxial cable for readout. The readout is described in detail in Section 3.3.2.

### 3.2.2 Construction Materials

This section will discuss the materials used in the construction of the ECal modules. The scintillator material and WLS fibres are common to every sub-detector in the ND280 except the TPCs.

#### Plastic Scintillator

The plastic scintillator is the active material of the ECal (and other ND280 detectors). The bars were extruded at FNAL and delivered to several sites in the UK for quality assurance testing. Each bar is coated with  $\text{TiO}_2$  to reflect escaping light back into the bar, thus increasing light capture in the fibre and providing light isolation between bars. The scintillator is polystyrene based and doped with 1% PPO and 0.03% POPOP. Maximum fluorescence occurs at wavelengths around 340 - 400 nm. The scintillation process starts with the excitation of the base polystyrene plastic. This excitation energy is transferred to the PPO via resonant dipole interactions. The PPO emits this energy as UV light (wavelength 340 nm). The UV light has a low transmittance in the plastic and so the POPOP is added to plastic. The POPOP serves as a wavelength shifter, absorbing the UV light and re-emitting it at wavelengths of around 410 nm where the attenuation length is much longer[51]. The production of usable signal relies on the deposited energy being transferred to the PPO dopant material.

#### Wavelength Shifting Fibres (WLS) Fibres

All ND280 scintillator detectors use Kuraray Y11 (200) S-35 multi-clad fibres for readout. These fibres have an attenuation length greater than 3.5 m while the maximum fibre length of any module is 3.9 m. To minimise signal loss through attenuation, these fibres are double ended. The shortest fibres are only single ended readout however. The wavelengths emitted by the scintillator have peak intensity in the blue region of the light spectrum. However,

MPPCs have peak sensitivity in the green region of the spectrum around 500 nm. Therefore, the Kuraray Y11 fibres were chosen as they offer optimal performance as a green shifting fibre with an emission peak of 474 nm.

For single ended readout fibres, one end was coated with a thin, polished mirror to compensate for the single ended readout and reduce signal loss. Each fibre is a polystyrene core surrounded by two layers of polymer cladding to enhance light yield. The diameter of the fibres is 1 mm.

### 3.3 Detector Electronics and Readout

#### 3.3.1 Multi-Pixel Photon Counters (MPPCs)

The photosensors used in ND280 must be capable of operating in a magnetic field and compact enough for use in the confined space of the magnet. Traditional multi-anode PMTs used in previous neutrino experiments are both too large and incapable of operation in magnetic fields. R&D was performed by several companies to develop the new photosensor design. The Hamamatsu MPPC was chosen from several candidates. Figure 3.2 shows the appearance and active area of an MPPC.

An MPPC is compact, insensitive to magnetic fields, operates at a relatively low voltage of 70 V and offers performance comparable to that of a traditional PMT as shown in Table 3.2. The active region of the MPPC consists of 667 pixels in a  $1.3 \times 1.3 \text{ mm}^2$  square. Each pixel is a Silicon, pn-junction based, avalanche photo-diode operating in Geiger mode. The sum of the output of these pixels is the output of the MPPC. When a photon interacts in the absorption region of the pixel it triggers an avalanche. As the avalanche develops, the electron-hole pairs created reduce the effective voltage across the junction until it falls below the breakdown threshold. The amount of charge output from each pixel is therefore dependent only on the operating and breakdown voltages of the device. This makes the readout of each pixel essentially binary. Despite this, the MPPC itself as a whole is an analogue device with a readout range limited by the number of pixels. The final readout of the MPPC is directly proportional to the number of pixels fired which in turn is proportional to the number of incident photons. The probability of a photon triggering an avalanche (photon detection efficiency, PDE) in a pixel is characterised by the overvoltage,  $dV$ , applied to

	MPPC	PMT
Gain	$10^5 - 10^6$	$10^6 - 10^7$
Applied Voltage	$\sim 70$ V	$\sim 2000$ V
Active Area	$1\text{mm} \times 1\text{mm}$	$\sim 10$ cm diameter
Photon Detection Efficiency	$\sim 30\%$	$\sim 15\%$

Table 3.2: Comparison of MPPCs to traditional PMTs

the MPPC. Putting this together, the overall gain of the device is calculated as,

$$G = (C/e) \times dV \text{ where, } dV = (V_{op} - V_{br}) \quad (3.3)$$

Where  $C$  is the capacitance of a pixel,  $e$  is the electron charge and  $V_{op}$  and  $V_{br}$  are the operational and breakdown voltage respectively. In practice each MPPC will have a slightly different breakdown voltage due to variation in the MPPCs themselves. The high voltage power supply provides only a single output voltage and so, in order to mitigate the variation in breakdown voltage, the voltage from the high voltage power supply is reduced by a given amount for each MPPC. This reduction is called a 'trim' and it's functionality is provided by the front end board the MPPC is attached to.

There are two sources of noise inherent to MPPCs. The first is pixel cross talk. Cross talk occurs when the firing of one pixel causes a neighbouring pixel to fire without an incident, signal, photon. Cross talk is due to optical photons being produced in a Geiger avalanche and trigger another avalanche in an adjacent pixel[52]. The second and larger source of noise is dark current. This is due to thermal excitations in the pixels initiating an avalanche and mimicking a photon count. The probability of a dark noise avalanche is independent and random for each pixel and so most dark noise will be a 1 photoelectron signal with the 2 photoelectron signal being an order of magnitude smaller. The dark noise rate is dependent on both the temperature and the overvoltage of the MPPC making it useful for detector monitoring and calibration.

### 3.3.2 TripT Front-end Boards (TFBs)

Each TFB hosts 4 Trip-T chips[53][54] and can readout up to 64 MPPCs at a time. Each Trip-T chip can read out 16 MPPCs into 32 channels. Each channel has two amplifiers,

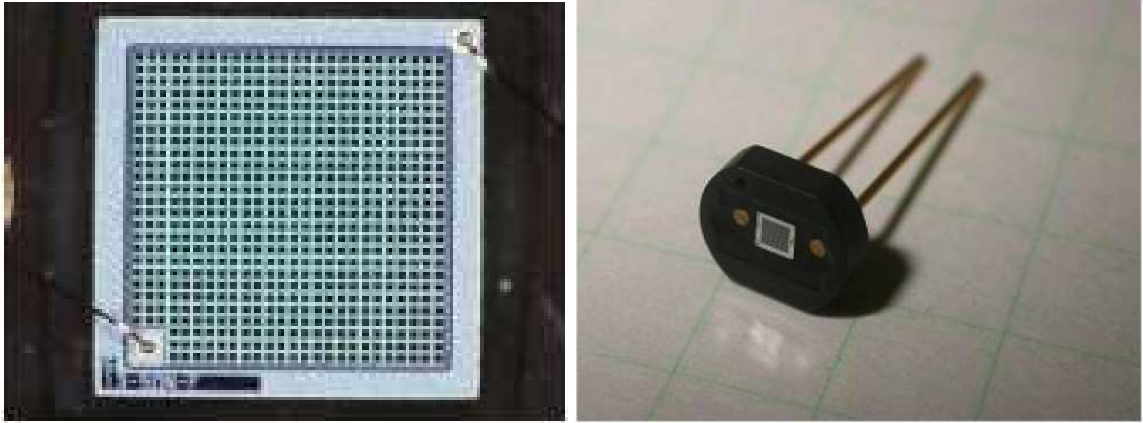


Figure 3.2: Left: The active area of an MPPC showing the array of  $50\mu m$  pixels and the electrode in the bottom left corner. Right: An MPPC in its ceramic package

a discriminator with a programmable threshold and an analog pipeline. This allows two channels per MPPC, a high gain and a low gain channel, each with separate gains and discriminator thresholds. The output from the discriminators is passed to a multiplexer that decides which signal is transferred off chip. A TFB with connected MPPCs can be seen in Figure 3.3. The TFB as a whole is controlled by an FPGA (Field Programmable Gate Array) which also timestamps the output. The Trip-T chips integrate each channel in 23 time bins with programmable integration and reset times. The ECal modules use an integration time of 256 ns and a 50 ns reset time. The output for each integration cycle is stored in a capacitor array for each channel. When all 23 integration cycles have been stored for a given trigger they are read out by two ADCs (Analog to Digital Converters) to digitise the signals.

The TFB also has several functions beyond pure readout. The TFBs supply the high and low voltages to the MPPCs via the co-axial cables. The low voltage provides the MPPC trims mentioned in the above subsection.



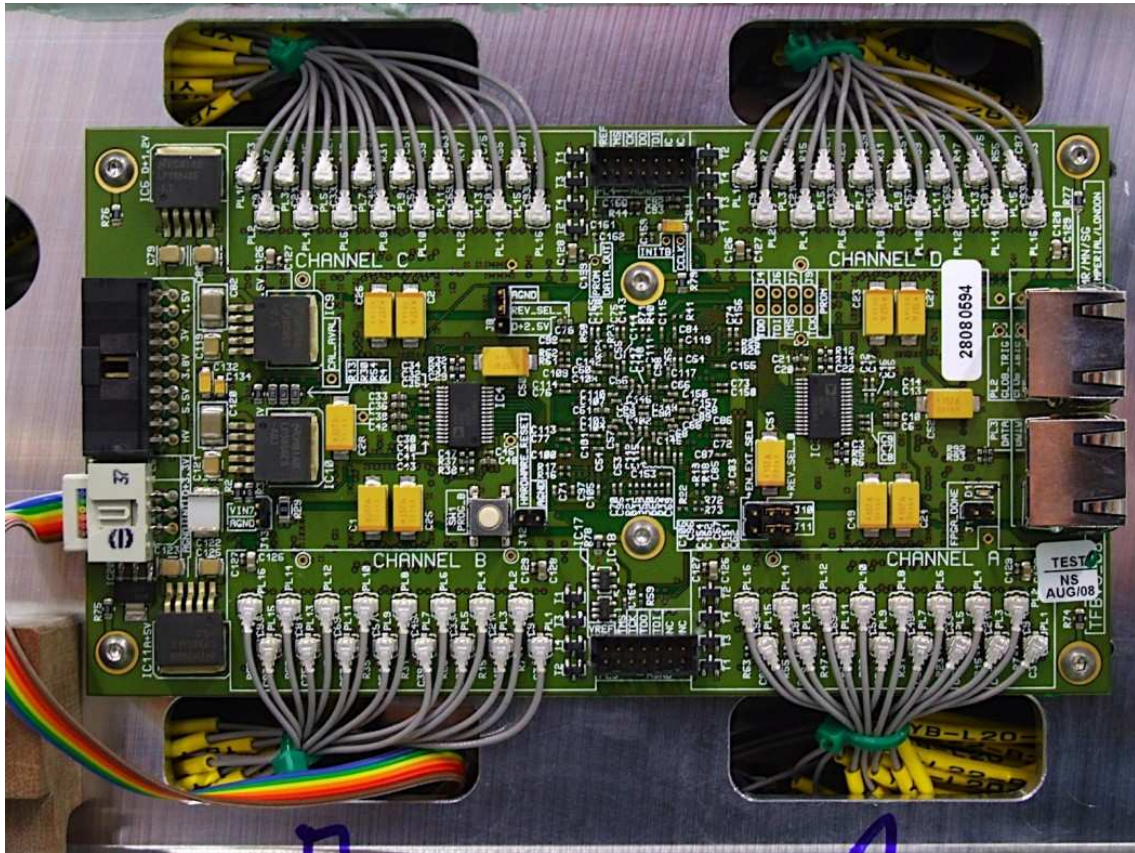


Figure 3.3: A TFB in place on a cooling plate with 64 MPPCs connected. The rainbow cable is connected to a temperature sensor which is thermally connected to the bulkhead

### 3.4 Construction of the Barrel ECAL modules

#### 3.4.1 Preparation

The Barrel ECAL modules were constructed in parallel at two sites in the UK: The University of Liverpool and Daresbury Laboratory. From these construction sites the modules were shipped directly to the experimental site in Japan.

Before construction could begin, a robotic scanner and a metallic base were assembled at each site. The scanner was designed to use a robotic arm to pass a radioactive source over newly inserted layers in a predefined pattern to test for defects. Each scan was performed and analysed overnight for efficiency and safety reasons.

Next, the module base and the stainless steel bulkhead are assembled in the scanner. The module base is composed of a carbon-fibre outer skin surrounded by a large aluminium

frame (Figure 3.4). The bulkhead is bolted vertically to the aluminium frame. The bulkhead had a height of 40 cm and a thickness of 2.5 cm. The length is defined by the dimensions of the module being constructed. Each bulkhead has an array of holes drilled into it so that the WLS fibres may be passed through and into the centre of the scintillator bars. Below each of these holes is a smaller, threaded hole to fix the MPPC casing in place.

After this the first layer of the module is laid on top of the carbon fibre base and centred. The layer is then screwed to the module base. This allows the Light Injection (LI) system to be attached to the carbon-fibre around the edge of the layer. The LI system is a single strip of LEDs glued down along each readout edge of the carbon fibre frame. Carefully chosen focussing lenses are then glued on top of the LED strips. After this the WLS fibres can be inserted and the layer insertion proceeds as normal.



Figure 3.4: An assembled module base and bulkhead.

### 3.4.2 Layer Construction

ECal layers were constructed in parallel at both Daresbury lab and the University of Lancaster and shipped to the appropriate build sites. To start the process, an aluminium frame is screwed to a construction table. This frame formed three edges of the layer. After this



several locator pins were inserted into the frame to ensure the correct placement of the bars inside the frame. The frame was filled with the bars that would be used to form the layer to ensure a good fit before being fixed in place. After this, the lead sheets to be used were vacuum lifted into position and marked so that the lead could be trimmed to fit the layer exactly before adhesion. The lead and scintillator bars were then removed from the frame.

Araldite epoxy adhesive was applied to the 1 cm thick edges of the bars to be inserted into the layer, this would glue each bar to the next. After this the bars were placed into the frame and forced together to ensure strong adhesion. When moving each bar great care was taken to ensure that significant flexing of the scintillator did not occur. At this point, quality assurance had already been performed on the bars and thus any damage to them would go undetected until it was too late to replace damaged bars.

After this more Araldite epoxy was applied to a lip on the frame and the top of the scintillator bars. The epoxy was spread out into a thin layer over the entire layer of bars. The lead sheets were then vacuum lifted back on top of the scintillator bars so that it overlapped the lip on the aluminium frame. The whole layer was then covered in plastic sheeting and sealed so as to be airtight. A vacuum was then applied to the layer overnight to cure the adhesive and form a strong bond. The completed layer was then stored until being inserted into a module or shipped to a build site. A completed layer is shown in Figure 3.5

### 3.4.3 Layer Insertion

A vacuum lift was required to move completed layers. The weight of completed layer meant that no section of the layer could be unsupported during the lift without destroying the layer. As such, the suction pads of the vacuum lift were placed at regular intervals on the lead surface of the layers to prevent any damage to the layer during movement. The layer was roughly aligned to sit on top of the previous layer (or carbon skin in case of the first one). A set of grub screws threaded through the bulkhead were then used to achieve precise alignment with the previous layer. At this point the new layer was fixed to the previous layer by inserting screws into holes in the aluminium frame. The screws were inserted and tightened from one corner of the module to the other in a linear fashion. This method served to avoid any tensions being introduced to the layer as a result of slight



Figure 3.5: A completed layer for the left side barrel module.

misalignments between the layer. Any tension from misalignments would be 'squeezed' out along the module edge instead of becoming trapped between already fixed screw holes. Figure 3.6 shows the un-instrumented end of several inserted layers.

Once the layer was firmly secured the robotic scanner was used to profile the layer's surface. In the larger modules some layers started to sag in the middle, far from the supporting frame. In this case padding material wrapped in plastic sheeting was introduced on top of this layer to prevent further sagging and maintain alignment in the next layer. The padding material was lightweight but strong so as not to interfere with detector operation.

#### 3.4.4 Fibre Insertion

WLS fibres were inserted through the bulkhead by hand and into the central hole of each bar. A guide was used so that the fibre could be easily passed through the 1 cm gap between the bulkhead and the layer. This guide protected against multiple insertion attempts which could easily damage the end of the fibre. During insertion each fibre was handled wearing Nitrile gloves to avoid deposits being left on the fibre surface which might diminish light transmission. Further to this, the fibres were gently wiped with non-fibrous wipes to remove any dust.



Figure 3.6: An end view of several ECal layers showing the lead-scintillator sandwich structure and the alternating orientation of the scintillator bars.

A plastic ferrule was required at each readout end of a fibre so that the MPPC and it's housing may be securely attached to the fibre whilst damaging neither. The fibres for short scintillator bars were delivered with the ferrule already glued to one end. For the longer, double ended readout fibres the ferrule was attached at the build site. The ferrules were attached using BC-600 Optical Cement with a refractive index close to that of the plastic scintillator bars. The glue was applied to the fibre with care being taken not to obscure the end of the fibre with the glue. The ends of the fibre were polished and very flat to minimise optical distortions in light exiting the fibre, any glue on the end would ruin the benefits of both the polishing and the flat surface.

After application of the glue the ferrules were slowly placed on the fibre. The ferrules were held in place by springs mounted in plastic caps. These caps ensured that the fibre protruded the correct amount beyond the ferrule so that a good optical connection would be formed without damaging the MPPC that would later be attached. It was also important to ensure that the ferrules were not putting the fibre under too much tension which could cause damage over time. The plastic caps were removed after the optical cement had set. Figure 3.7 shows several layers worth of attached ferrules in the module bulkhead.

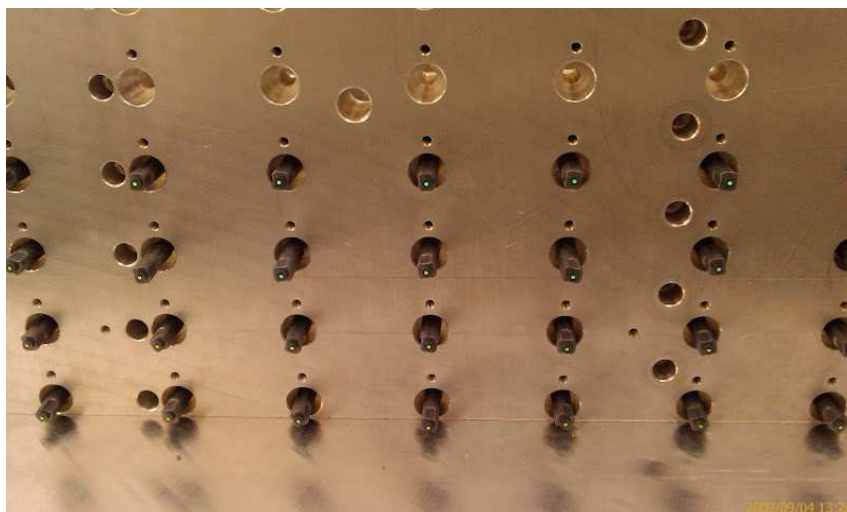


Figure 3.7: The ends of the WLS fibres in the bulkhead with plastic ferrules attached.

### 3.4.5 Layer Scanning

In order to test the quality of the newly inserted layer it was scanned using a collimated radioactive source. The source was 115 Mbq Cs-137 housed in a protective casing. Due to the activity of the source the construction room had to be vacated whenever scanning was taking place and the source had to be stored in an iron housing when not in use. The scanning was performed overnight for efficiency and safety. Before the scan was started the whole module was made light tight using a black industrial covering, without this light tightening the MPPCs would saturate even in a dark room. The scanning source was held roughly 1 cm from the surface of the module and thus great care had to be taken when attaching the light tight covering. If the covering protruded too far from the layer surface it could cause an obstruction, damaging the scanner and delaying construction.

Due to the potential for damage during construction the final readout electronics were not attached until the very end of the module construction. Instead, a test set-up was used on each layer during the scanning process. Two TFBs and the associated MPPCs were fixed to metal trays so that they could be attached and removed to each layer as needed. The MPPCs were clipped onto the fibres of the new layer and the metal trays fixed to the bulkhead to provide readout. The whole module was then covered in light tight material and optically sealed for the duration of the scan.

The scanner was programmed to hold the source over 20 points along each bar allowing an attenuation curve to be plotted for each sensor in the layer. This tested the quality of the bar, fibre and optical connection. Any damage to a bar or fibre would appear as a kink in the attenuation curve whilst a bad optical connection would not give an attenuation curve. Any bad fibres or connections were replaced and rescanned. After this the layer installation was complete and the next layer could be inserted.

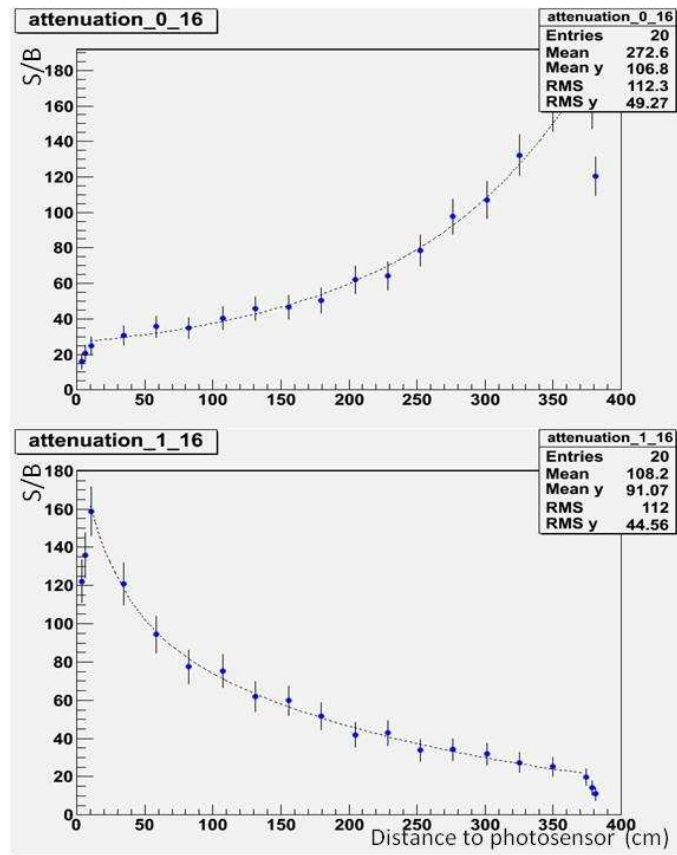


Figure 3.8: Fibre attenuation curves for a good fibre and connection. Significant signal loss occurs at the ends of the bars as can be seen in the plots.

### 3.4.6 Finalisation and MPPC Connection

When the the final layer is inserted the skin and electronics could be attached to the module along with the necessary service structures. MPPCs were clipped onto the end of each fibre in a specially designed shrouding as shown in Figure 3.9. The coaxial cable, used to connect the MPPC to the front end board, was attached to the PCB. The two pins protruded out of



the PCB on either side of the co-axial connection. It was vital to make sure that the end of the co-axial cable did not touch these pins. Any contact between the cable and pins would create a short circuit and prevent that channel from being read out. A screw was placed through the hole in the shroud and screwed into the bulkhead to hold the MPPC assembly in place. Each MPPC and cable was pre-labelled with an assigned channel number and TFB. This is used downstream to produce a channel mapping for the software geometry. Each co-axial cable was then grouped together based on which channel on which TFB they would be connected to.

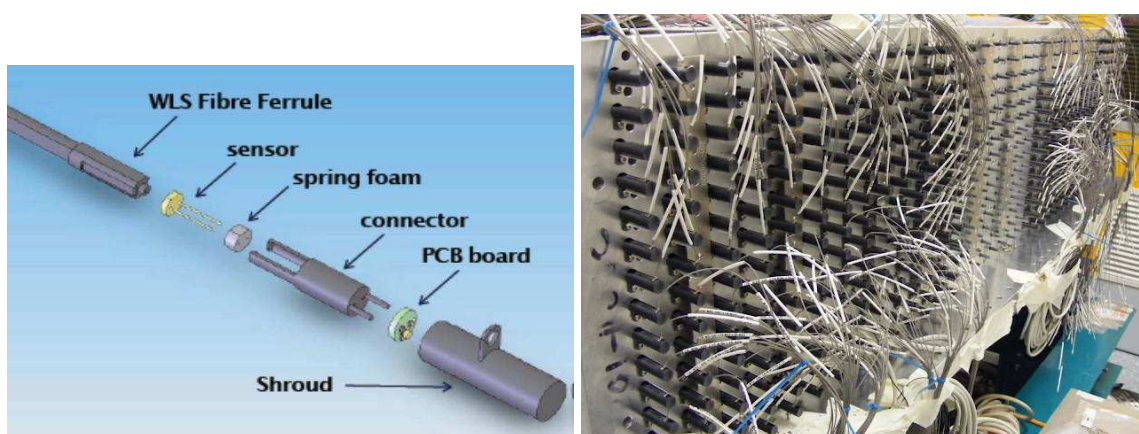


Figure 3.9: Left) The sensor-fibre connector shrouding. The setting tool clipped onto the ferrule holding the MPPC in place at the end of the fibre. Right) A picture of the MPPCs attached to the end of the fibres with the cables grouped by TripT.

During operation the TFBs require cooling to prevent overheating and damage to the boards. As a result the TFBs are affixed to stainless steel cooling plates using a thermal cooling plate, this allows the heat generated during operation to be dissipated much more quickly. The cooling plates were loosely fixed in place on the outer edge of the bulkheads and the co-axial MPPC cables were passed through the appropriate gaps in the cooling plates. At this point the cooling plate could only be loosely affixed at this point so that the MPPCs could still be accessed and, if necessary, replaced.

The label on each cable was used to clip the co-axial cable to the appropriate channel on the appropriate TFB. Each MPPC and TFB was tested to check for damage. Any damage was repaired or replaced. This ranged from faulty sensors, cables or boards to the simple short

circuit between the cable and pins. The length of the co-axial cables prevented complete removal of the cooling plates at this point without having to re-connect every MPPC (a lengthy process). This meant that any replacement or repair work had to be performed in the confined space that could be created behind the cooling plates without disconnecting or damaging the cables that were already attached.

The penultimate task was to add services to the module. First, five copper bus-bars were installed around the the centre of each module face hosting TFBs. These bus bars would be used to power the TFBs providing the four low voltage lines and one ground line. Metallic cooling pipes were also passed around the top and bottom of the modules. The cooling pipes were thermally coupled to the TFB cooling plates at several points on each face of the module. Finally, RJ45 patch cables were plugged into each TFB for readout to the back-end boards. These RJ45 cables were then passed through a patch panel to be inserted in the modules outer cover plate.

With the services and readout cables attached the final cover plates of the module were fixed in place. The module face without electronics readout was covered with a metal sheet. The other three sides were covered with metal plates, one of which contained the patch panel, the connection for the bus-bars, the intake for the dry air service and the inlets and outlets for the cooling water. The opposite face house two black vents as outlets for the dry air.

The second half of the module's LI system was affixed to the top skin of the module in the same manner it was affixed to the module base. Once the LI was installed correctly the module's top was bolted on top of the bulkhead. The module top was of the same construction as the module base for the side modules, i.e. a carbon fibre skin surrounded by an aluminium edging. For the top and bottom modules the top face was a thicker metallic construction with grooves so that the module could be fixed to the inner surface of the ND280 magnet on I-beam rails. An example of such a top face can be seen in Figure 3.10. At this point the module is completed and ready to be shipped to the experimental site.



Figure 3.10: A completed barrel bottom ECal module. The grooves on top of the module are for sliding the module onto the metal beam that will eventually attach it to the ND280 magnet.

### 3.4.7 Shipping

Before shipping, the module was enclosed in an air-tight wrapping and packaged in a wooden crate. The air-tight wrapping was included to protect the module from condensation during transport. If condensation water became trapped in the module it could have caused a number of problems including, short circuits and damage to the fibres or bars. An accelerometer was attached to the module during the shipping process to watch for any sharp jolts that could damage or move module components.

## 3.5 On Site Checkout and Testing

The DS-ECal was shipped and installed in 2009 for the initial data taking run. It was during this period that the barrel ECal modules were constructed. As the barrel modules arrived in Japan they were unpacked and visually inspected for damage. The air tight wrapping had been pierced during the packaging of one module which resulted in some cosmetic condensation damage. Due to time constraints imposed by the start of data taking, only the top left barrel module was installed for the winter 2010 run. A mechanical fault in the top



left module created short circuits preventing it being operated.

A replica DAQ system was set up to test the modules. This allowed any non-visible damage to be repaired before installation in the magnet. It also provided stress testing for the modules and TFBs. The DAQ test stand initially contained two RMMs and one clock module connected to two processing nodes. It is important to note that the test stand lacked a cosmic trigger module and thus could only take pedestal data. Pedestal data is sufficient to test the behaviour and integrity of the MPPCs and TFBs but any damage to the fibres or bars would remain unseen. It was deemed that this was not a real concern as fibres and bars could not be replaced at this point. A further constraint imposed by the testing area was the lack of water cooling and dry air services. During checkout procedures the module took pedestal data as much as possible (roughly eight hours per day). The modules had to be frequently monitored during data taking so that they did not overheat without cooling. This prohibited overnight data taking. Each module was subjected to roughly one week of running as a form of stress testing for the TFBs. Before this longer term testing a few short tests were performed to ensure all the readout electronics were functioning after shipping. This test was performed by coarsely scanning the high voltage supplied to the MPPCs so that all channels were operating above breakdown voltage and producing at least a single photoelectron peak.

## **Chapter 4**

# **ECal Commissioning and Operation**

The Downstream ECal was the first module to be installed in 2009, before the first T2K physics run. At this time a single barrel module was also installed (the top-south module) but did not operate during this run period due to a cabling failure. This failure was then repaired after the first data taking run. The rest of the barrel ECal modules were installed into the ND280 magnet during summer 2010, prior to the second physics run in autumn 2010. The whole ECal had been run as a full system and as such numerous tests and calibrations were required to ensure the entire ECal was ready to take physics data. From autumn 2010 until the beginning of 2012 I held the role of ECal expert and was responsible for commissioning the new ECal modules and ECal operation during data taking.

This chapter will discuss the major tasks involved in the commissioning and subsequent operation of the ECal. Firstly, a brief overview of the, relevant, DAQ and electronics systems will be given to define terms necessary for the following discussions. After this the work to commission the detector will be discussed, describing both the importance of the task and the techniques used. Then a brief discussion on the ECal data quality and detector operation will be given. Finally, this chapter will discuss the efforts to recommission the ECal after the earthquake damage in 2011.

### **4.1 Readout Electronics**

The readout electronics use TFBs (Section 3.3.2) and Readout Merger Module (RMM) back-end boards. These components will be described in enough detail to allow later discussion on operations work. The discussion will be specific to the ECal but the generalities

also apply to the other TripT systems.

#### 4.1.1 Electronics Front-End

TFBs provide the front end of the ECal readout. A basic description of the TFBs is given in Section 3.3.2 but a few further details will be noted here. More complete details on the front-end readout electronics can be found in [54]

For each MPPC, the TFB splits the readout signal and routes it to two different ADCs (Analogue Digital Converters). Each of the two ADCs operates at a different signal gain to maximise the readout range of the detector. For the ECal the low gain channel reads roughly 14 ADC counts for a single photoelectron (p.e.). The low gain channel saturates at a signal of 500 p.e.[54]. The FPGA on the TFB timestamps the output from the ADCs and sends this information to the back-end board. TFBs also record and transmit monitoring information for the detector such as temperatures and voltages. The TFBs have an internal temperature sensor and a slot for the connection of an external sensor. A number of TFBs in each module use a temperature sensor attached to the module bulkhead whilst the rest use the MPPCs for temperature monitoring.

#### 4.1.2 Electronics Back-End

The electronics back-end uses a single hardware board design, developed at Rutherford Appleton Laboratory. The individual hardware boards are configured to act as either a readout merger modules (RMM), a cosmic trigger module (CTM), a slave clock module (SCM) or a master clock module (MCM).

The signals from the TFBs are carried to the RMMs via shielded, Cat 5e cables. The maximum number of TFBs readout by an ECal RMM is 48, although, an RMM can readout up to 64. The RMMs distribute trigger and clock information to the TFBs in addition to reading and processing the signal output of the TFBs. The RMMs receive the trigger and timing signals from the SCMs. Each RMM has 500 MB of on-board memory allowing it to store up to 128 triggers. Triggers can originate from either the MCM or CTMs. The MCM can generate pedestal triggers at an adjustable rate. The MCM also receives signals from the accelerator, providing a means to trigger on beam spills. Each module also has an SCM, providing this functionality when the detector operates in a local partition, independently

from the global system. The CTMs are connected to a selection of front-end boards; one CTM is connected to the TripT detectors while the other is connected to the FGDs. The CTM produces triggers based on coincident, above threshold, signals from the front-end boards. Seven TFBs from the DsECal are connected to the CTM. A programmable prescale is applied to the cosmic trigger to optimise the detector coverage.

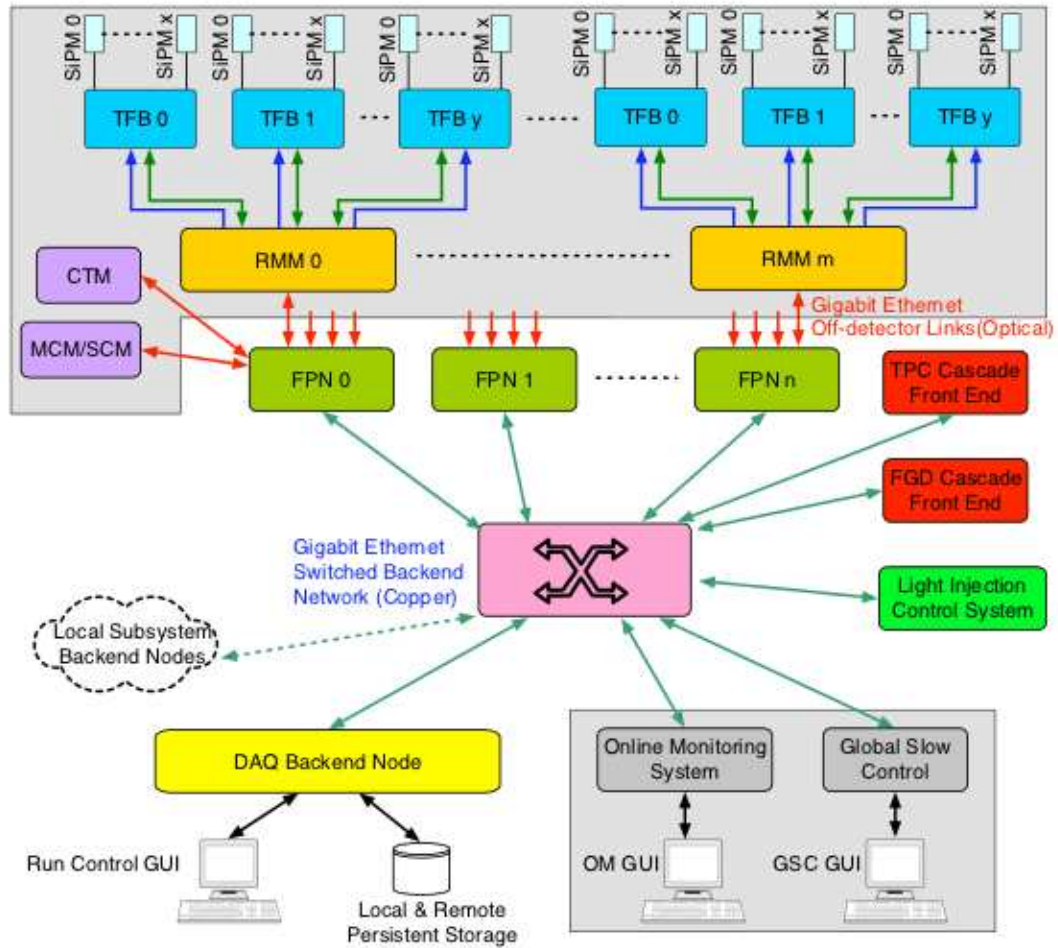


Figure 4.1: A generic schematic of a Trip-T sub-detector DAQ[23]

## 4.2 Data Acquisition

The ND280 data acquisition is split into two parallel parts, the DAQ that handles the data stream and the global slow control (GSC). The DAQ can be operated in either local or

global mode. Global mode is used for standard data taking and as such uses all ND280 detectors and components. The local mode allows each sub-detector to operate independently in its own partition of the DAQ. This is used to perform ECal-only calibration runs in preparation for beam data taking. In local mode the ECal SCM provides the same functionality as the MCM in global mode. The Trip-T CTM is inaccessible to the ECAL local DAQ and so cosmic ray data cannot be taken. This limits calibrations in local mode to using pedestal data. A schematic of the DAQ layout is shown in Figure 4.1

The GSC is accessed through web pages and, like the DAQ, uses a MIDAS interface. The low voltage and high voltage power supplies can be controlled through the GSC allowing them to be controlled remotely. The GSC also allows for detector monitoring using a series of history plots. The data for the GSC history plots is provided by TFBs for the most part.

#### 4.2.1 Processor Nodes

The RMMs are controlled and readout by the front-end processor nodes (FPNs). The ECal uses five FPNs to control the detector RMMs and one for the ECal SCM. The FPNs run three processes, one readout configuration task, a data processing task (DPT) and a final buffering and dispatch process. The DPT performs data reduction and some basic processing. An important function for the purposes of this document is the raw data histogramming. As it receives data, the DPT fills histograms with signal amplitudes on a per channel basis before zero suppression. These are called DPT histograms and they are integrated into the output stream and are a useful tool for detector calibration and monitoring.

### 4.3 Detector Commissioning

The ECal was integrated into the ND280 DAQ system and debugged by experts from Rutherford Appleton Laboratory (RAL) before being passed on to the detector expert for commissioning. The DAQ system is discussed in more detail in Section 4.2. The first task was to ensure that the ECal was set-up correctly. It was found that, whilst in global mode, fewer TFBs were included in the data output than were operating in the modules. This irregularity was not observed in the local ECal DAQ where all TFBs were producing data. The issue was traced back to an error in the mapping of RMMs in the global DAQ as shown

RMM	Expected Number of TFBs	RMM Number of TFBs
0	28	28
1	28	28
2	15	15
3	44	15
4	44	44
5	26	44
6	26	26
7	15	26
8	26	26
9	26	26
10	44	44
11	44	44

Table 4.1: The expected and observed number of TFBs being readout on each RMM after integration of the ECal into the global DAQ.

in Table 4.1. RMMs seeing more than the expected number of TFBs would still only record data for the expected number leading to data loss. By changing the mapping variable in the global DAQ this issue was rectified.

The modules were then made ready for physics data taking. The most important task was the online calibration of the ECal modules. This included the initial setting of MPPC gain and pedestal values. There was a vast difference between the environment and settings between the checkout area and the interior of the ND280 magnet rendering any previous calibrations invalid. The new calibration was performed from scratch for the new modules. The calibration process was already working for the DsECal but extensions to include the Barrel and POD modules were necessary.

The gain calibration is of particular importance as any error cannot be corrected later in the calibration chain, rendering any data taken useless. The method for the gain calibration is based around scanning the high voltage supplied to the MPPCs and is discussed in detail in Section 4.4. The initial calibration was lengthier and more complicated than subsequent calibrations. The further the MPPCs are from the desired operational range, the larger the range of the high voltage scan must be. Due to some necessary assumptions made in the calibration process, the efficiency of a high voltage scan decreases if it's range become too large. A set of initial gain values were boot strapped from independent data but an iterative

procedure was required to give the best possible calibrations.

The pedestal signal also has to be calibrated for us in zero suppression. The pedestal has a smaller impact and can in most cases be corrected later in the calibration chain. The main purpose of the pedestal calibration is to identify the position of the pedestal peak at the beginning of the run to provide a baseline to measure pedestal drift and to be subtracted from detector hits.

When the ECal was fully calibrated, the next task was to update the online monitors and slow control alarms. The functionality of the monitors and alarms was, again, already in place for the DsECal but required upgrading to work for the newly installed modules. The monitors were less of a priority as they do not directly effect the quality of the ECal data. It was, however, very important to have the alarms operational as soon as possible to avoid any damage to the ECal during data taking.

With the detector calibrations complete and the monitoring infrastructure complete, the ECal was ready to take physics quality data before the start of T2K Run 2 in Autumn 2010.

## 4.4 MPPC Gain Calibration

The online calibration of the ECals is centred around setting the gains of the photosensors to the correct value. Poorly calibrated MPPC gains will result in poor quality data from the ECals and many of these effects cannot be calibrated out in the later data processing stages. MPPC noise rates are directly related to the MPPC gains, large changes in noise rates can effect event reconstruction and physics analysis background rates. More important, given the purpose of the ECal, is the change in energy response caused by poor calibration. If the MPPCs are set to incorrect gains, the energy scale of the detector will deviate from the expected region for large variations. This will cause the ECal to incorrectly reconstruct the energy of particles entering it.

The gain of an MPPC is directly related to it's overvoltage by Equation 3.3. However, the breakdown voltage is temperature dependent, meaning that the operational voltage required to give the desired overvoltage will also vary with temperature. The ECal is thermally coupled to the water cooled magnet, however temperature variations still occur. Diurnal variations are observed but are small and unavoidable. Larger, seasonal tempera-



ture variations can significantly change the gain spectrum of the ECal and therefore requires careful monitoring and correction. The nature of the calibration process and DAQ means that this task can only be performed during long enough periods with no neutrino beam. It is therefore beneficial for this process to be as quick as possible. The implementation of an improved method was one of my major contributions and will be discussed below. The overvoltage, and thus gain, is set using high voltage trims discussed in Section 3.3.1. It is the trims that are calculated and set during this calibration.

#### 4.4.1 Calibration Method

To be effective the calibration method requires that the MPPC gains are set approximately correctly at the start of the procedure. This is not an issue during data taking as the previous trim values are available and usually of the right magnitude. However, for the initial calibration Hammamatsu provided data on their own tests, allowing trim values to be bootstrapped.

This calibration needs to be performed in local mode to maximise the use of beam down-time. It is unfeasible to use the global DAQ to perform ECal only calibrations. The local ECal DAQ only has access to a clock module and not a CTM. The clock module is only capable of creating pedestal triggers, effectively limiting any MPPC calibration to using these. The only signal observable in a pedestal trigger is that of dark noise and so any local calibrations must be performed on this data. The properties of dark noise were discussed previously in Section 3.3.1. Each data run in the calibration must contain enough event triggers so that the single photoelectron, dark noise peak is well defined in each channel. Dark noise occurs randomly and independently in integration cycles within a single trigger. There is, therefore, no correlation between dark noise hits in separate integration cycles, each of the 23 cycles in a trigger can be treated as an independent measurement for the purposes of gain calibration. Each trigger therefore provides 23 measurements in the MPPC spectra, reducing the number of triggers required.

A single pedestal run is not sufficient to calculate the breakdown voltage of the device. By scanning over the applied voltage and characterising the change in gain, the breakdown voltage can be calculated and the desired overvoltage can be set. A MIDAS XML sequencer



is used to take a series of automated pedestal runs with a range of global offsets to the high voltage trims, thus altering the supplied overvoltage. This gives a range of ADC spectra for each channel at slightly different voltages.

For each point in the high voltage scan, the low gain ADC spectrum for each channel is analysed. To extract the gain, a peak finder is applied to the spectra to identify the 0 and 1 photoelectron peaks. This is then used to find the first minimum in the spectrum by calculating the integral in slices of 2 ADC counts after the 0 pe peak. Once the trough is found two Gaussian distributions are fitted to the data as shown in Fig 4.2. The gain is then taken to be the difference in means of the two fitted Gaussian distributions. If two peaks cannot be found in the spectrum, the fit is abandoned for this offset point.

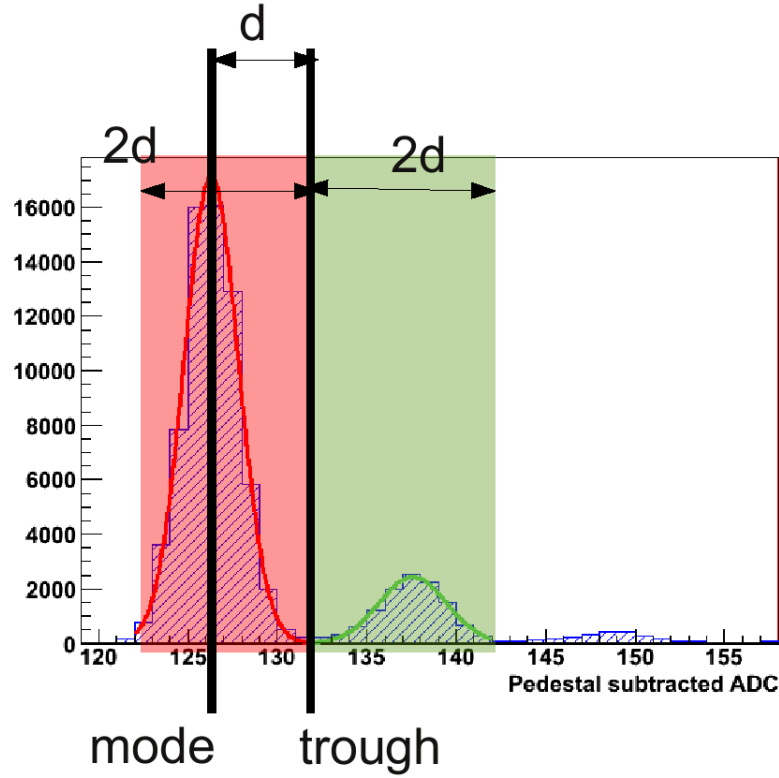


Figure 4.2: An example MPPC spectrum with the shaded regions showing the ranges for the Gaussian fits.

The gains for each channel are then plotted as a function of the applied trim (nominal trim + high voltage offset). The MPPCs are assumed to be operating in breakdown mode and so a straight line is fitted to this plot. The breakdown voltage is then taken to be the

y intercept of the line fit. From this the trim is set so that each MPPC will be operating at an overvoltage of 1.336 V, roughly corresponding to a gain of 14 ADC counts per photoelectron.

If some channels are operating with gains outside of the acceptable values, the results of the scan can be analysed and these channels can be manually corrected. When the number of poorly calibrated channels is too high, each bad channel has its trim set to the average for MPPCs on the same TripT and the scan is performed again. MPPCs on the same TripT are generally from the same production batch and so have similar breakdown voltages. This means that setting a bad channel to the average for the TripT will bring it in to the range where another scan will work.

This process performs within specification, producing a spread of channel gains centred around 14 ADC counts with a width of less than 10%. Figure 4.3 shows an example of the spread of gains before and after the calibration procedure has been applied.

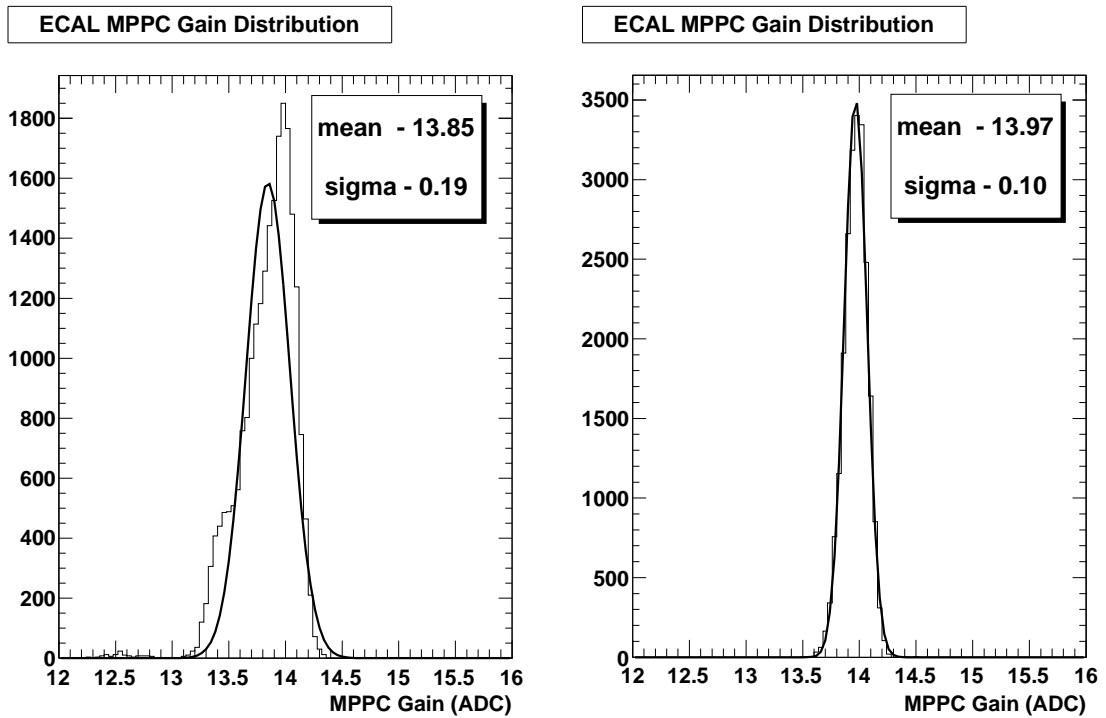


Figure 4.3: Both plots show the gains for all channels in all ECal modules. The left shows the gains before a voltage scan. The right shows the gains after a voltage scan and has a good Gaussian shape with a mean close to 14 ADC counts.

#### 4.4.2 Calibration Issues

The calibration process can fail if the assumption that the MPPC will be in breakdown mode is not true. When the trim value is such that an MPPC is turned off or saturating, the peak finder will fail to find two peaks and the analysis will be abandoned for that spectrum. The case where the MPPC is on the verge of saturating or turning off is more problematic. In this case the peak finder stage will usually succeed. However, the ADC spectrum will often be distorted causing the peak finder to incorrectly identify peaks and so give an incorrect gain value. This can then skew the line fit producing a bad calibration. Another possibility is that the MPPC is operating just outside of breakdown mode and thus the linearity assumption fails for some region of the scan. This will skew the calculation of the breakdown voltage and produce a poorly calibrated channel. This second failure mode is less severe than the first and will generally give a gain estimate close to the acceptable range.

The failure modes mentioned above are the reason that this calibration will generally not work if the MPPC trims are not set to begin with. Attempting to use this calibration in this manner requires a wide range to be used in the voltage scan. This will result in a scan taking data in several of these problem regions and thus becoming unreliable. This highlights the importance of selecting an appropriate range for the voltage scan.

#### 4.4.3 Procedure Improvement

The frequency of this calibration in data taking is limited by the frequency of sufficiently long beam downtime. Therefore, reducing the time taken for this calibration increases how often it can be performed. The taking of the pedestal data is relatively efficient and could not be made any faster without reducing the quality of the spectra. The largest contribution to the calibration time was preparation of the data for analysis which used roughly 70% of the processing time.

The initial method took the raw MIDAS files as the inputs and converted the data to the ND280 raw data format before starting the analysis. Then the charge deposit in each integration cycle was used to fill a histogram, to give the ADC spectra for each channel. The data conversion makes this a lengthy process. As mentioned in Section 4.2.1, the

DPT stores raw charge spectra in histograms before any data compression and saves these histograms in the MIDAS files. By accessing and using these DPT histograms the lengthy conversion and histogram filling can be avoided allowing the programs to immediately begin the analysis after fetching the histograms.

#### 4.4.4 Pedestal Calculation

Pedestal calculation is a much simpler process than gain calibration. A single, sufficiently long run is taken with a 0 trim offset. This run is then analysed to find the 0 p.e. (pedestal) peak in each channel. The method for this is the same as that described for the gain calibration. The pedestal value is taken to be the mean of the Gaussian fit to the 0 p.e. peak. The runs used for pedestal calculation need to be significantly longer than those used for gain calculation as a separate pedestal is calculated for each integration cycle (capacitor) on each channel.

There are two types of pedestal calculation, beam/pedestal and cosmic. The need for two different calibrations is due to the difference in integration behaviour between the two types of trigger. For cosmic triggers the channels cycle continuously. The 23 most recent integration cycles are stored and the capacitors are only discharged to read a new cycle or when a trigger signal is received. When a trigger is received, a predefined number of cycles are readout before and after the signal are recorded. During beam and pedestal trigger mode, the boards wait for a trigger signal before integrating. This leads to slightly different charge accumulation on the capacitors than in cosmic trigger mode.

### 4.5 Detector Operation

The detector operation for the ECal involved three main tasks, monitoring the ECal status, liaising with the data quality group and updating online calibrations where necessary. The calibration of the detector has already been discussed in detail in the previous section and the techniques used remain the same during operation. For this reason, this section will concentrate on the detector monitoring and data quality. This document does not provide a comprehensive guide to the duties of an ECal expert but only offers an overview of the most important tasks.

### 4.5.1 Calibrations

Frequent recalibration is necessary to ensure optimal data quality during operation due to intrinsic drift in the electronics and changes in environmental variables such as temperature. Re-calibrations must be performed after any change in the magnet operation i.e. when the magnet opens/closes or powers up or down. These changes affect significant changes in temperature that take of order a day to stabilise. Due to the cost of operating the magnet, it is usual to only power up the magnet days before the start of neutrino beam, giving a small time period available for detector calibration. This expounds the need for quick and efficient calibration methods. Beyond this, the necessity of re-calibration is determined by examining the online monitoring plots.

### Charge Injection

The TFBs have the capacity to inject charge directly to the capacitors of a channel. This allows calibration of the electronics readout independent of MPPC signal and using a known amount of charge. To perform this calibration, a series of runs are taken with the MPPCs operating far below breakdown voltage, turning them off. During these runs the TFBs inject and readout charge in each channel. Taking this sequence of charge injection runs takes of order 14 hours and so requires a significant length of beam downtime. Due to the rarity of beam downtime of sufficient length, charge injection runs are a high priority when they do occur.

### 4.5.2 Data Quality

The ECal data quality group is responsible for producing a series of plots showing low level ECal information on a weekly basis. Based on this information a flag is applied to data to indicate whether or not the ECal was operating correctly during data taking. The data quality group and ECal experts were required to liaise frequently to ensure optimal data quality. Much of the data quality work will not be discussed here, only those parts directly relevant to expert duties and monitors developed by the author.

### Dead Channel Counting

The number of dead channels in the detector is a good indicator of performance. An initial dead channel count is required to define the baseline number of active channels and initial quality of the ECal construction. Dead channels are then counted on a weekly basis and any new dead channels are investigated by the ECal expert. For Run 2 data taking there were 42 unrecoverable dead channels out of 22336 across all ECal modules.

Pedestal triggers are taken at the rate of roughly 0.5 Hz during data taking. The DPT (Section 4.2.1) uses these pedestal triggers to produce the raw data histograms as previously mentioned. These DPT histograms are analysed as they are acquired during data taking. A channel is flagged as being dead if it is both instrumented and no photoelectron peaks can be found in its low gain ADC spectrum. The ADC low gain spectrum and the high voltage trim are investigated for new dead channels. An incorrect trim setting can cause a channel to appear to be dead. If the trim is too high, not enough voltage will be supplied to the MPPC and effectively turn it off, giving no p.e. peaks in its spectrum. If the channel trim is too low, then the channel's gain will become too high and width of the p.e. peaks will increase until they overlap. In extreme cases the channel may begin to saturate meaning that it reads out a maximum charge signal. These 'dead' channels are recoverable by altering the voltage trim to bring the channel into the correct operational voltage region. This is done using the same method to correct failed calibrations from a high voltage scan.

However, a hardware fault can also produce similar failure signals but will be unrecoverable. Setting the trim to a maximal or minimal value will show if the channel is recoverable as the channels should turn off or saturate respectively. Any channel saturating with a maximal trim or not responding with a minimal trim is classed as unrecoverable due to a hardware fault and marked dead so that it is ignored in offline reconstruction and data analysis.

### Trip-T Occupancy

For beam triggers we can check the performance of Trip-T chips by monitoring the number of channels that give hits with valid timestamps. Valid, non-noise, hits within the detector should have a TDC (Time to Digital Converter) timestamp associated with them. By inte-

grating over all channels on a Trip-T for 10 beam spill triggers it is expected that almost all will have at least one valid hit. The frequency of these timestamped hits is the constraining factor on the granularity of the quality check. When integrating over fewer than 10 beam spills the effectively random occurrence of timestamped hits leads to a fluctuating number of unoccupied Trip-Ts. These fluctuations make it difficult to establish a baseline activity leading to the check becoming ineffective. At the 10 spill level, no more than 3 Trip-Ts are receiving no hits with valid timestamps during Run 2. The frequently unoccupied Trip-Ts read out a far lower number of channels than average causing the integration time to be too short. The increase in integration time to account for these channels would have a negative impact on the quality of the check and so they are absorbed into the baseline measurement. An example of the output of this check is shown in Figure 6.2.

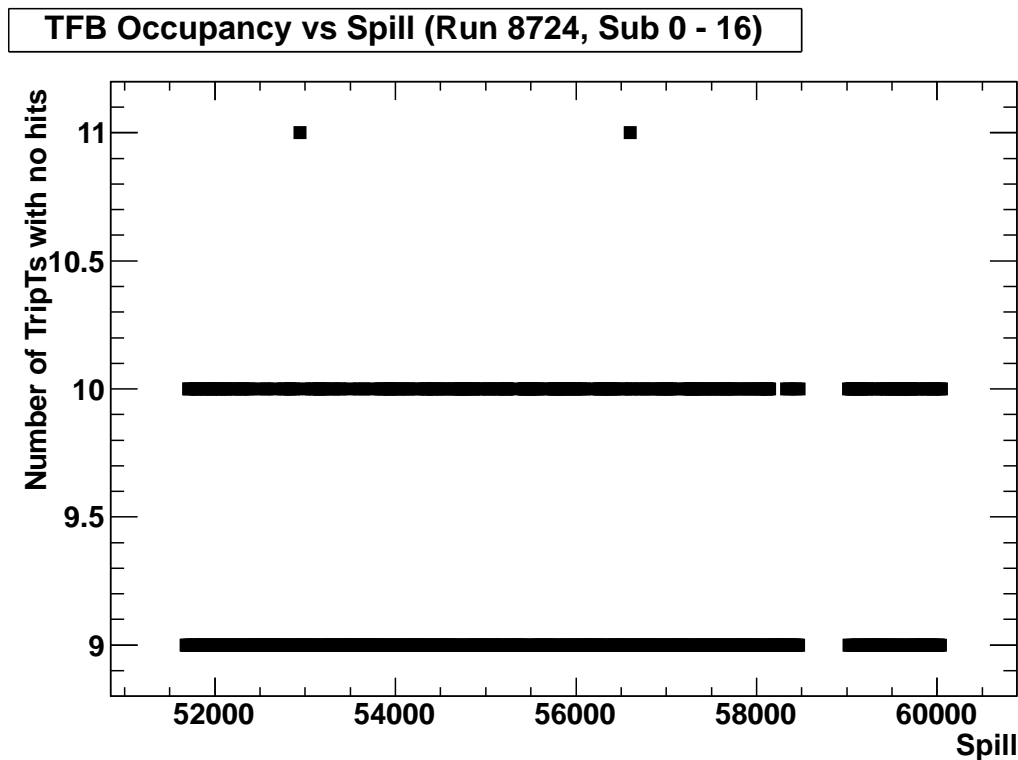


Figure 4.4: Trip-T occupancy plot during the Run 3 data taking period. The number of dead Trip-T chips is inflated compared to Run 2 due to damage sustained during the earthquake.

### 4.5.3 Detector Monitoring

The online monitoring for the ECal is performed using histograms produced by the GSC and an 'online monitor' task analysing the DPT output in real time. It is the responsibility of ECal experts to check these plots on a daily basis and where necessary, use them to identify and debug problems. The GSC logs detector information provided by the TFBs, creating a series of history plots. These plots show variables such as temperature, voltages, currents and flow rates against time. They do not generally indicate the quality of the data being read by the ECal but are used to diagnose problems observed more directly in the DPT plots. After the installation of the new modules for Run 2, scripts were upgraded to produce the GSC history plots for all ECal modules. An online monitoring program analyses the DPT histograms produced periodically during data taking and plots the results.

#### Temperatures

Two temperature measurements are made per TFB. The first is an internal temperature measurement made on the board itself. This is the hotter of the two measurements due to the thermal output of the TFB electronics. The second is an external measurement and is provided by either, a dedicated thermal sensor on the module bulkhead, or using the MPPCs themselves.

Diurnal fluctuations are clearly seen in these temperature plots and should not exceed  $1^{\circ}\text{C}$ . It is not unusual to observe a small increase in temperature during the initialisation of a TFB as the heat output increases with the activity. The range of the time axis can be extended, showing slower seasonal shifts in temperature more clearly. Figure 4.5 shows example monitor plots for both a long and short time scale.

Section 4.4 discussed how temperature directly effects the gain calibration of the MPPCs. Therefore, any large fluctuations in temperature have a direct impact on calibration quality. After correcting for seasonal temperature drift, any fluctuation large enough to impact the calibration significantly would be an indicator of a larger problem. Either a fault on a TFB or a problem with the detector cooling. In addition to the history plots the GSC runs an alarm program that triggers if a TFB reads a temperature less than  $16^{\circ}\text{C}$  or more than  $30^{\circ}\text{C}$  for two readings consecutively. These limits are conservatively based on the design



operation range of the module,  $0^{\circ}\text{C}$  to  $40^{\circ}\text{C}$  Operation outside of these limits presents the possibility of damage to the module.

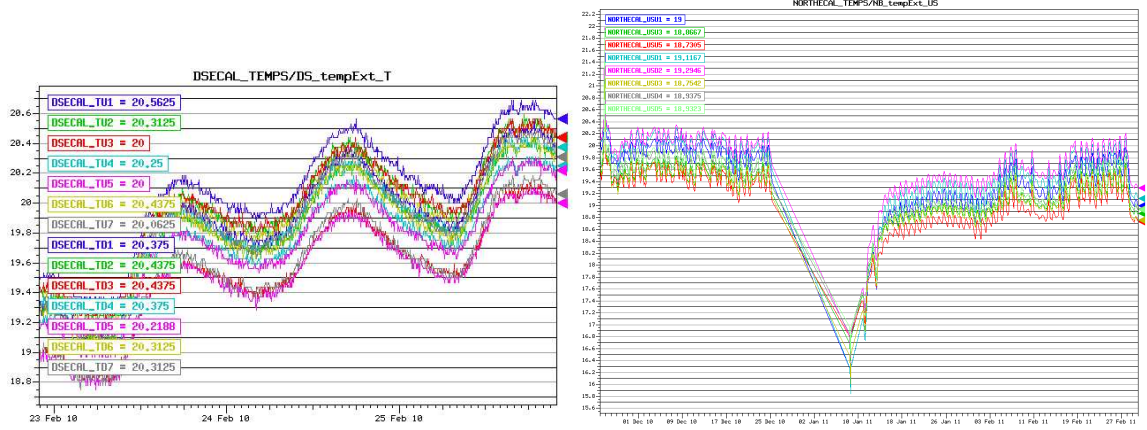


Figure 4.5: Two temperature history plots taken from the GSC. Measurements over 3 days on the left and over Run 2 on the right. Each line on the plots shows the temperature measurements of a single TFB with time. The differences in temperature between TFBs is caused by physical location within the detector. In the Run2 plot the seasonal change in temperature is visible. The New Year shut down period is shown along with the magnet ramp-up afterwards.

## Voltages

For each TFB, the 4 voltage lines (2.2 V, 3.2 V, 3.8 V, 5.5 V) are monitored with both the voltage and current drawn being read out. The monitoring of the voltage lines is more difficult than the temperature monitoring. A number of TFBs have voltage lines displaying erratic behaviour in the monitor plots but all other TFB performance checks show that the boards are functioning properly. The unusual voltage readings are likely caused by problems with the board readout[55] in the absence of any other observed issues. Also, the current draw plots often show some transient fluctuations shortly after initialisation of the board and show small variations depending on detector activity.

The voltage lines are used to both power the TFBs and to readout the charge collected in each channel, therefore unusual behaviour in the voltage supply plots can explain irregularities in other plots. During Run 2, the pedestals began to vary wildly on one TFB. The voltage across TFBs was too low for the 2.5 V line, as shown in Figure 4.6. The voltage output from the power supply for this line was increased to 3.5 V to fix the problem. The

voltage across a TFB is regulated on board to some extent and so although the output from the supply was increased to 3.5 V, the voltage across the TFBs only increased to the desired 2.5 V.

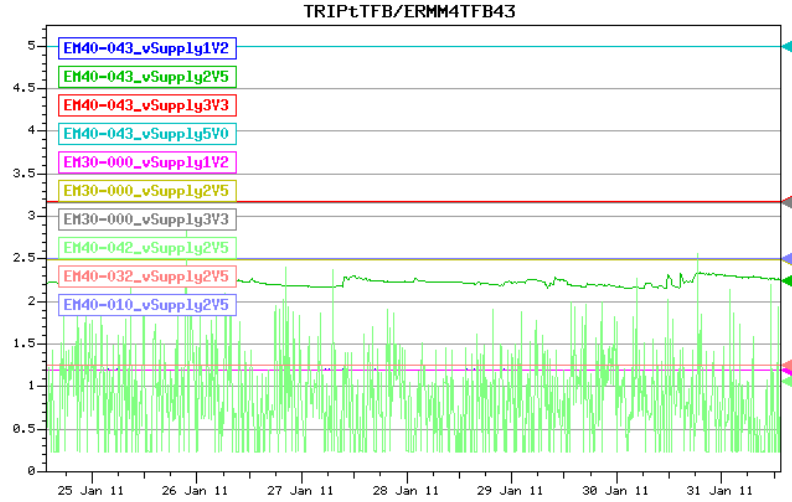


Figure 4.6: The voltage monitoring plot for 2 TFBs. One with wildly drifting pedestals and another operating normally. The 2.5 V line for the first TFB is shown to be constantly lower than 2.5 V. A second 2.5 V line shows erratic, oscillating behaviour due to a sensor error.

## Cooling

The ECal electronics are water cooled to prevent damage due to over heating. This is particularly important for the RMM boards which consume a lot of power during operation. The cooling water is vacuum pumped from a large reservoir of water chilled to  $7^{\circ}\text{C}$  at negative pressure. The negative pressure prevents any small leaks from damaging the module electronics. The flow for each ECal is monitored in a GSC history plot filled with data from a flow meter attached to each loop. The flow rate in each should remain between 4 to 5 l/min with only small fluctuations. Any degradation in the flow rate can indicate a leak in the loop that will require intervention at the next opportunity. No irregularities were observed in the ECal loops during Run 2 data taking. An example plot is shown in Figure 4.7.

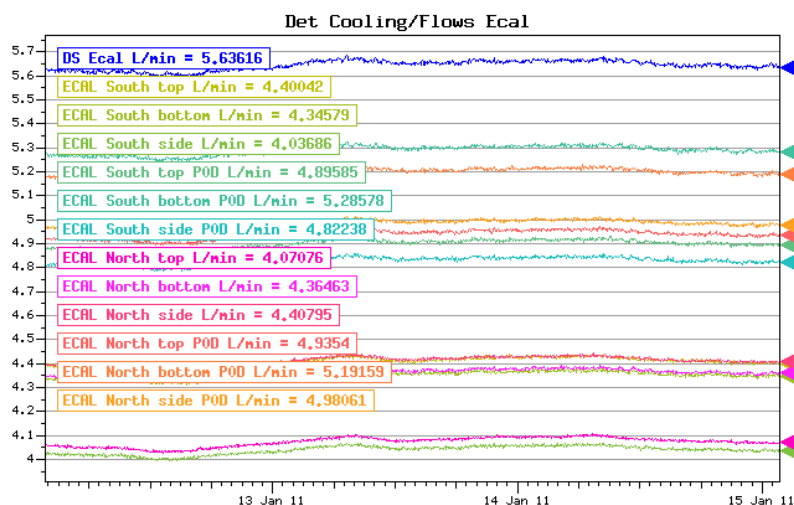


Figure 4.7: The ECal flow rate history plot showing the rate for each module.

### Noise Rates and Pedestal

The online monitoring program analyses the DPT histograms to produce plots of pedestal, noise rates, status and gain for every channel. These plots give a clear, instantaneous, measure of detector performance, both per channel and per RMM. The regularity and the coarseness of these plots make them essential for observing any issues with the ECal data output. The data quality information is only produced on a weekly basis due to processing constraints and so incurs some time disparity between observing a problem and having the opportunity to correct it. The online monitoring plots can be checked multiple times per day allowing a much faster response. This is at the cost of granularity, it is much more difficult to see single dead channels appearing in the monitoring plots, whereas the data quality plots will show them very clearly. The online plots are most useful for observing calibration drifts in larger groups of channels and so planning the use of the next beam downtime. Figure 4.8 shows a case where the gains of channels on two RRM's have drifted and need to be re-calibrated.

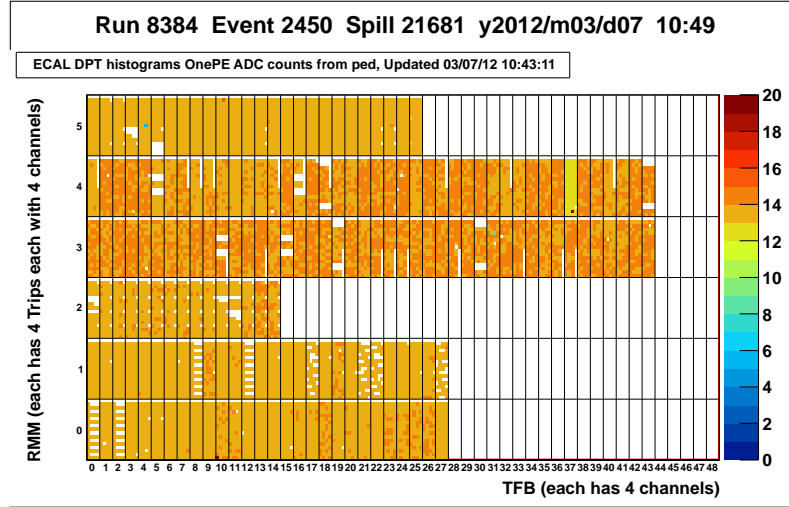


Figure 4.8: An online monitoring plot showing the gain per channel for 6 ECal RMMs. It can be seen that a number of channels (particularly on RMM 3-4) are drifting from the desired gain of 14 ADC counts.

## 4.6 System Recovery

In March 2011 a 9.0 Richter scale earthquake occurred off the east coast of Japan. The experimental site (and the local area) experienced levels of shaking rated as a 6+ (the second highest rating) on the Shindo scale. J-PARC experienced power loss and in some areas, several meters of subsidence. An inspection and recovery period began shortly after and lasted until December 2011. Physics data taking was resumed in January 2012, after successful recovery of all systems, for T2K Run 3. The recovery took a great deal of work from many institutions and people on all aspects of the experiment at the JPARC site. This section will only cover the recovery and recommissioning of the ECal system, in which, I played the leading role.

### 4.6.1 Hardware Inspection

Among the first operations was the opening of the ND280 magnet. This was done so that visual examinations of the module could be performed and any necessary repairs could be made. In this case it was particularly important to drain the ECal cooling loops during the magnet opening. There existed an increased possibility that, during the intense shaking, a cooling pipe could have shifted, become trapped or simply been punctured. In any of

these cases, the movement of the magnet could lead to a large enough leak to overcome the negative pressure of the cooling system and pump water into the detector system. Once the magnet had been opened, the cooling loops were visually inspected where possible and then refilled as the inspection showed no damage. The refilling process was carefully monitored to spot any previously unseen damage quickly and thus minimise any further damage in this case. No additional damage to the cooling loops was observed in this process due to the secure fastening of the cooling loop positions.

The modules themselves were directly examined for any external damage. Due to the space limitations inside the ND280 magnet, the clearances of various components was kept deliberately small, for example the clearance between the ECal and the basket. If the components moved relative to each other it is possible that some impact damage could have occurred during the earthquake. No visible damage was observed beyond documented, pre-existing cosmetic damage.

It is also possible that the components acquired a large shift in relative alignment and so all ECal clearances were remeasured prior to magnet closure. This measurement was performed using a laser level placed on the ECal surface faces. The laser level had an offset of 10 mm from the ECal face, the limit for acceptable clearance. As the magnet closes, it moves  $\sim 3$  mm relatively in the vertical direction compared to the basket, therefore, the lower modules required an enlarged clearance of 15 mm. All clearances were found to be sufficiently large so as not to cause damage during magnet closure.

During the final magnet closure during December 2011, the ECal touch strips were monitored as shown in Figure 4.9. Some cables had been re-routed for some basket detectors and may have been sheared during closure if their clearances were not sufficient. These cables were positioned parallel to the ECal inner edge and so the laser level could not measure the clearance. If the clearance was not sufficient, the touch cables would give a signal and the closure could be stopped. A touch strip triggered a signal once, the closure was stopped and the cause was investigated. It was found to be due to the sagging of some TPC service cables on the underside of the basket. It was judged that the tension exerted on the cable after full closure would have been unacceptable and so the cables were repositioned to ease the tension. No other issues arose during the magnet closure.



Figure 4.9: Monitoring the ECal touch strip sensors during magnet closure.

#### 4.6.2 Re-commissioning

Hardware inspections could only reveal any outer signs of damage. To declare the detector ready for operation again, software and data checks had to be performed and the detector recalibrated. Much of this work was the same as the original commissioning work described in Section 4.3. However, some new checks were implemented for fibre and bar integrity. During this recommissioning period I was responsible for training a new ECal expert to take on the duties for Run 3 and the re-commissioning activities.

As the DAQ was brought back online by experts from RAL, it was found that two ECal TFBs had become unresponsive and could not be repaired. Both TFBs were located on the north, side, barrel ECal. One of the damaged TFBs read out a bar with double ended readout, lessening the impact. Other than this, there was no significant damage in the ECal DAQ. After this was established, the recommissioning proceeded as before, the online calibrations were performed and the dead channel count was updated. Only an additional eight channels were lost in addition to those on the two damaged TFBs. This work verified the status of the readout electronics but could not give an indication of the state of the scintillator bars and WLS fibres. Any damage to these was deemed unlikely but worth

investigating.

A dedicated cosmic trigger run was taken over the course of a day accumulating a large number of events. A simple track fitter was applied to this data to produce a map of cosmic ray start and end positions in the ECal modules. With enough statistics the spread distribution of track positions should be roughly even across the module faces. This method relies on real detector hits as opposed to MPPC noise and so depends on the status of the whole channel, from scintillator bar to TFB channel. Some hit maps are shown in Figure 4.10. The distributions shown are roughly as expected. The empty space in the Y-Z plot is due to one of the damaged TFBs.

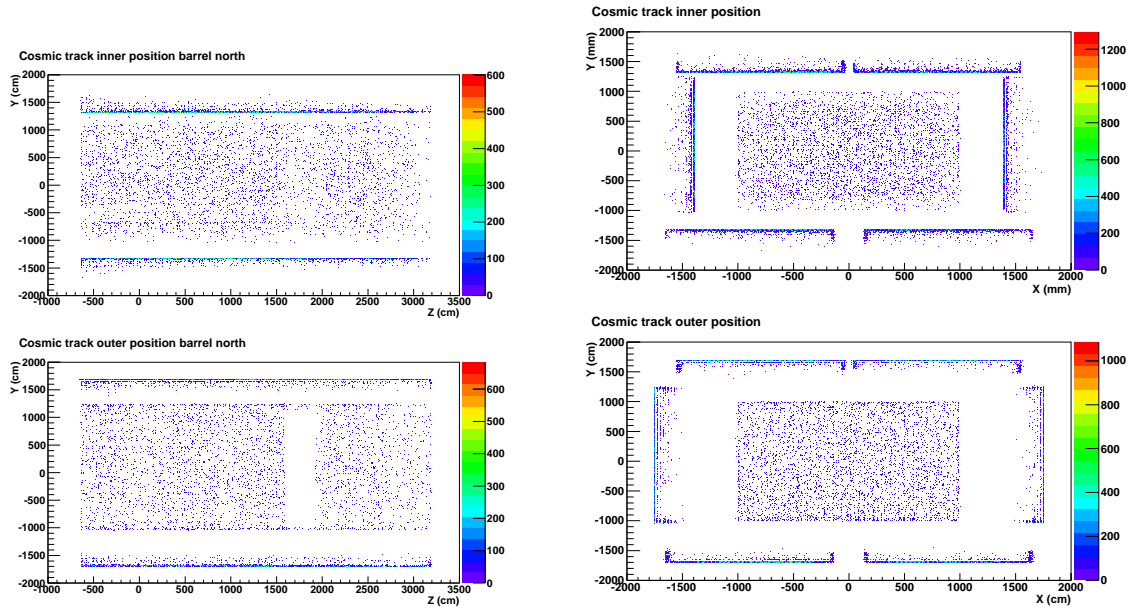


Figure 4.10: Plots showing the inner (top plots) and outer (bottom plots) track positions of cosmic rays passing through the ECal modules. The left plots show the north side view. One of the dead TFBs is clearly shown as the empty region in the bottom plot. The right plots show the downstream view looking anti-parallel to the beam-direction.

The energy deposit per unit length for MIPs in the detectors was also checked in the cosmic run and compared to pre-earthquake data. The data for each bar in the ECal is corrected for bar-to-bar variations and the charge deposit is normalised to 100 cm distance



from the photosensor. A histogram of energy deposit per unit length is filled for many muons per bar. In the ideal case this will produce a Landau-Gaussian distribution and a fit is applied to find the most probable value (MPV), called the 'MIP scale' of the channel. Any damage along the length of the bar or any change to the optical connection with the MPPC should affect a change in the MIP scale of a channel or cause the MPV fit to fail. The number of channels that failed the MIP scale fitting process was found to agree with the dead channel count from pedestal data. Also, the MIP scale of the detectors agreed well with previous values, with variations being of the order of calibration uncertainties. Both these results imply there was no damage in addition to that observed in the ECal electronics and DAQ. With the damage quantified and recorded and the detector successfully recommissioned, the ECal was ready for the start of Run 3 data taking having sustained very low levels of damage.



## Chapter 5

# ND280 Event Reconstruction

In order to properly describe the event selections used for the final cross section ratio measurement, the ND280 event reconstruction must first be described. The reconstruction of the TPC, FGD and ECal subdetectors will be discussed along with the combination of the sub-detector reconstructions. The FGD provides the neutrino interaction target and the TPC provides the PID of the produced particles. The vertex reconstruction in the tracker region will also be discussed due to its importance in selecting multi-track events. ECal reconstruction will also be described briefly. The global reconstruction takes the output from the sub-detector reconstruction algorithms and combines by matching sub-detector objects to each other using the RecPack Kalman Filter[56]. It is this global reconstruction output that will be used in the final measurement.

### 5.1 The ND280 Offline Software Chain

The ND280 offline software suite handles the processing of both data and MC files through a variety of different packages. Figure 5.1 shows a visual interpretation of the ND280 offline software. There are essentially three event formats in each chain. The chains begin with a raw format, which differs slightly between the chains. This raw format is then converted into a format referred to as 'oaEvent' format. It is common to both data and MC and is used to store data during the calibration and reconstruction phases of the software chains. The oaEvent format retains detailed information and so a stripped down file format is produced at the end of the processing chain to reduce final file size. This final event format is called 'oaAnalysis' format. oaAnalysis is an almost pure ROOT[57] format allowing small

file sizes and fast analysis.

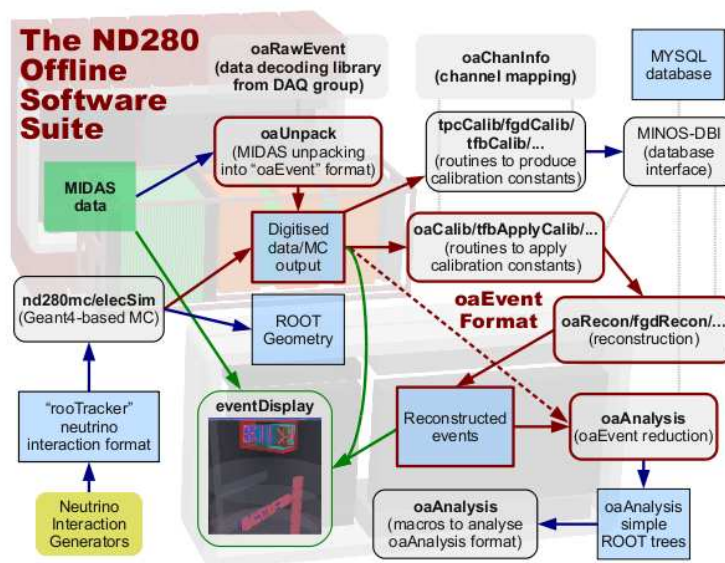


Figure 5.1: A visual Overview of the ND280 Software Suite[23]

The MC chain starts with a neutrino interaction generator to produce the simulated neutrino interactions based on neutrino flux inputs. The GEANT4[58] package is then used to propagate the secondary particles through the detector and simulate the energy deposit. After this the detector response is converted into the oaEvent format in both the simulation and data chains.

The data chain begins with raw MIDAS data which is unpacked into an oaEvent format. After conversion to oaEvent format the processing proceeds the same for both data and MC. Calibration is then applied to the oaEvent format events using a series of packages and calibration constants stored in a MYSQL[59] database. The calibrated events are then input to the reconstruction packages. The oaEvent output from the reconstruction is then reduced down to oaAnalysis format files to be used for final analysis.

## 5.2 ND280 Reconstruction

The ND280 reconstruction takes calibrated oaEvent files as input. The events are first passed through individual sub-detector reconstruction packages. The outputs for FGD and TPC reconstruction are then passed through a tracker reconstruction algorithm to combine

the two outputs. Finally these outputs are passed through a global reconstruction package to combine information from all the sub-detectors. Only parts of the reconstruction chain relevant to the event selection shall be briefly discussed. More information can be found elsewhere [60].

### 5.2.1 Tracker Reconstruction

The ND280 tracker provides the interaction target regions in the form of the two FGDs discussed in Section 2.5.3. The TPCs provide the tracking and PID tools to accurately reconstruct event topologies and are discussed in detail in Section 2.5.2. Both the FGDs and TPCs have their own stand alone reconstruction packages. The results from these packages are then combined in a tracker reconstruction package.

The FGD and TPC reconstruction will only create tracks traversing a single TPC. Tracker reconstruction attempts to create longer tracks that cross multiple TPCs by matching several of these shorter tracks together. A simple algorithm is used that loops over all track pairs in adjacent TPCs. RecPack[56] is then used to extrapolate the tracks and calculate a chi-squared per degree of freedom for each of the track pairs. If the chi-squared per degree of freedom is below 100, the two tracks are then combined and refit using the RecPack Kalman Filter.

### 5.2.2 TPC Reconstruction

The TPC reconstruction package reconstructs tracks in single TPC volumes. Tracks passing through multiple TPCs will create a single track in each TPC. These tracks will be joined later at the tracker and global reconstruction stages. The TPC reconstruction first performs some final calibrations and creates a series of time ordered waveforms from ADC counts. These waveforms are then clustered together if they overlap in time and are adjacent in space. The reconstruction then attempts to form track segments by connecting clusters according to a cellular automaton algorithm. The clusters are combined to give the longest reconstructed track segment possible. Finally, the track segments are combined using a likelihood method based on charge deposition.

### 5.2.3 TPC PID

After track reconstruction, the PID algorithms are applied to the tracks. The TPC PID is based on the truncated mean energy deposit per track segment measure as,

$$C_T = \frac{1}{\alpha N} \sum_i^{\alpha N} C_C(i) \quad (5.1)$$

where  $C_C(i)$  is the energy deposit in cluster  $i$ ,  $N$  is the number of cluster measurements and  $\alpha$  is the truncation factor.

The truncated mean in this form is dependent on track length and so it is useful to define a more general measurement called the calibrated truncated mean,

$$\bar{C}_T = \frac{1}{\alpha N f(N)} \sum_i^{\alpha N} g(d_i) C_C(i) \quad (5.2)$$

where  $f(N)$  and  $g(d)$  are factors dependent on the number of clusters and the track length respectively[61]. These factors are chosen to be unity for horizontal tracks, parallel to the MICROMEAS readout pad plane.

For a given momentum we can calculate the expected calibrated truncated energy loss  $C_E(i)$  and its Gaussian width  $\sigma_T(i)$  for a given PID hypothesis  $i$ . Using this data we can construct PID pulls for different particle hypothesis such that,

$$\delta_E(i) = \frac{\bar{C}_T - C_E(i)}{\sigma_o(i)} \quad (5.3)$$

where  $\delta_E(i)$  is the PID pull for particle hypothesis  $i$  and  $\sigma_o(i)$  is the total width combining  $\sigma_T$  and the uncertainty on the momentum measurement. The pull distribution for a given particle type should be a Gaussian with mean zero and width of 1 for a pure sample of tracks of the given particle type. Therefore, a cut of  $|\delta_E(\mu)| < 2$  would select any tracks that match the predicted energy deposit for a muon to within two sigma.

#### 5.2.4 FGD Reconstruction

The FGD reconstruction is performed after the TPC reconstruction. The hits are initially grouped into time bins. If a TPC track has been reconstructed in a given time bin, the FGD hits in that time bin are then matched to reconstructed TPC tracks using the RecPack Kalman filter. The TPC track is extrapolated to the nearest FGD layer and a matching chi-squared is calculated for that hit. If the chi-squared is below a given threshold, the hit is added to the track. This process is repeated for each consecutive layer until there are no more layers or more than one layer has no FGD hits matched.

#### 5.2.5 Vertex Reconstruction

$CC1\pi^+$  events generally have 2 or 3 tracks originating from a single vertex. Therefore a reliable vertex finding algorithm is invaluable for signal selection and background rejection. A brief overview of the global ND280 vertex reconstruction method will be given here. A more detailed description is found here[62].

The vertex reconstruction takes the results of the tracker reconstruction as an input. The first step is that of track clustering. The clustering method is constrained to the XZ-plane of the detector so that magnetic field effects can be ignored. For a given pair of tracks, the distance of closest approach is calculated using a straight line fit between the high and low z ends of the track. The algorithm then checks that the pair of tracks are not part of a longer, broken track by cutting on the cosine of the opening angle between the tracks and the spatial separation of the track ends. If one track is found to cross the other, a cut is made on the distance from the end of the intersected track. Finally, cuts are made on the distance of closest approach. This is done for all pairs of tracks. Track clusters are then merged based on spatial proximity.

The resulting track clusters are then passed to a Kalman filter method. A vertex candidate is calculated from the track cluster. The tracks within the cluster are then propagated to the candidate position using RecPack and their covariances are updated. Tracks passing a chi-squared cut are then added to the vertex and used to update the vertex position. If multiple tracks are associated to the vertex an inverse Kalman filter is applied to the tracks using the final vertex position and the updated track covariances. The chi-squared values

calculated using the inverse filter are used to remove any outlying tracks.

### 5.2.6 ECal Reconstruction

The ECal reconstruction takes the output of the calibration algorithms as input. The hits from the calibration are first sorted into groups based on the hit times and bar orientation. There is a minimum of 50 ns between any two groups of hits, calculated from the last hit of the earlier group to the first of the later group. A charge threshold cut is also applied to the hits at this stage. The hits for double ended bars are then combined so that each bar has only a single hit in each time grouping. After this regrouping stage, some further calibrations are applied to standardise the hits with respect to a normalisation point.

The hits are then passed to a basic clustering algorithm. The clustering starts by using the hit with the highest charge deposit as a seed within a time grouping. Hits are clustered with the seed hit if it is a neighbour, or next to neighbour, of the seed hit by layer and bar and it has a time stamp within 15 ns of the seed hit time. The clustering is run recursively with each hit that has been clustered becoming the seed in turn. This continues until no more hits are clustered. The process then starts over with the highest charged, un-clustered hit. Any cluster with less than three hits is rejected.

Another algorithm takes the clusters created previously and attempts to increase the cluster size. The cluster with the highest number of hits is used as the seed. It is then matched to nearby clusters based on timing and spatial proximity based on a charge weighted principal component analysis.

There are further steps to combine the 2D clusters to create 3D clusters and apply PID to them and estimate the energy of EM showers. These steps are not used in this analysis and so will not be detailed here.

### 5.2.7 P0D Reconstruction

The P0D electronics are the same as the ECal readout and so the first step in P0D reconstruction is also to separate the hits into time groups associated with electronics readout cycles. Some noise cleaning is applied to the hits in the form of several charge threshold cuts dependent on the proximity of the closest neighbour hit. These hits are then passed to a 2D tracking algorithm. A Hough Transform[63] is used to select seed hits forming

a straight line in the detector. The seed tracks are required to have a minimum of 4 hits. The seed is then extended layer by layer, adding hits in a 60 mm wide path along the track trajectory. Several hits within a layer may be added to the track within the path.

The reconstruction then attempts to match the 2D tracks together to form 3D tracks. Each 2D track is compared in turn to 2D track in another view or previously constructed 3D tracks. Each pair is assigned a weight based on the number of overlapping layers, the relative charge deposited in each track and whether the track was already matched. The pairing with the best weighting is then selected and matched and the process begins again with the next 2D track. Once no more track pairings score above a matching threshold the matching is stopped and fitting algorithms are applied to the created 3D tracks.

Further algorithms are run to provide shower reconstruction and PID. This analysis is only concerned with the POD activity and so the PID and shower information is irrelevant. It is enough to know that a particle created a track in the POD and so reconstruction beyond this point will not be discussed or used.

### **5.3 Global Reconstruction**

The global reconstruction is the final step in the reconstruction chain and uses the output of all the sub-detector reconstruction algorithms. It is the output of the global reconstruction that is used in the analysis described by this document. The global reconstruction uses the RecPack Kalman filter to match reconstructed objects between adjacent sub-detectors. The reconstruction first attempts to match each tracker object to each object in the surrounding detectors in turn. If the pair of tracks pass cuts on matching chi-squared and time difference, the objects are merged and refitted using the Kalman filter. The matching scheme only attempts to match two objects at a time. The algorithm then attempts to match the combined object to further objects, allowing three or more objects to be matched. The process continues to iterate over tracks, both matched and unmatched, until no further objects are combined together.

## Chapter 6

# A $CC1\pi^+/CCQE$ Cross Section Ratio Measurement

This chapter will describe the selection of  $CC1\pi^+$  and CCQE events using the ND280 tracker. The motivation for such a measurement will be given initially, followed by the definition of signal events and datasets. The event selection cuts and the motivation behind them will be described for both processes. Finally, the methods used to evaluate the systematic uncertainties will be described. The systematic uncertainties fall into three categories, those relating to detector efficiencies, those due to uncertainties in the cross-section and interaction models and those due to uncertainties in the neutrino flux at ND280.

### 6.1 Measurement Motivation

The main physics goals of T2K are to measure the neutrino mixing angles  $\theta_{13}$  and  $\theta_{23}$  via  $\nu_e$  appearance and  $\nu_\mu$  disappearance respectively. In order to measure these processes the neutrino beam must be profiled at both the near and far detectors. A part of this profiling is the measurement of the  $E_\nu$  spectrum at the far detector. The  $E_\nu$  measurement is performed using a selection of CCQE events. At the neutrino energies produced by T2K  $CC1\pi^+$  interactions are the biggest background to the CCQE measurements. If the pion is not detected in a  $CC1\pi^+$  interaction it will appear in the detector as a CCQE interaction. This occurs due to detector inefficiency and final state interactions. Due to the different kinematics,  $CC1\pi^+$  events reconstructed as CCQE events will have a lower reconstructed energy. Many higher energy pion events will reconstruct as CCQE events at peak neutrino



flux energies where the oscillation maximum lies. Therefore, the  $CC1\pi^+$  contamination of the CCQE sample will introduce a systematic uncertainty on the  $E_\nu$  spectrum measurement and the disappearance analysis. The effect of this systematic uncertainty can be somewhat reduced by precisely measuring the  $CC1\pi^+$  cross section. The current uncertainty on the  $CC1\pi^+$  cross-section on water is too large at low neutrino energies and more accurate measurements must be made for T2K to achieve its design precision. ND280 is designed to measure the  $CC1\pi^+$  cross-section using a subtraction method using the carbon scintillator and water targets in the FGDs and POD. Currently the statistics recorded by T2K[23] are too low for such a measurement to be made, instead this analysis is designed as an initial development of a  $CC1\pi^+$  event selection and measurement using the well understood FGD1 and TPC2 sub-detectors.

The targets for T2K and future experiments must use heavy nuclei in order to achieve the high statistics required for precision measurements. When using large nuclei as targets final state interactions occur that obscure the nature of the true neutrino interaction. The final state interactions are relatively small for CCQE events due to the weak interaction of muons with the nucleus. However, measurement of  $CC1\pi^+$  cross sections will contain many contributions from these nuclear effects. Interaction models, such as NEUT[64] and GENIE[65], exist to simulate the neutrino and final state interactions (FSI). However, current interaction models have been shown to differ from recent data unless large error bars are assigned. These large errors are then propagated to oscillation measurements. This measurement uses signal definitions based on the final state particles and does not correct for final state interactions. This is done so that the basis of the selection is not dependent on the final state interaction model used. Dependence on the interaction model is introduced later during the analysis of the selections due to mitigating factors such as low statistics. As more statistics are acquired and the reconstruction improves, a more sophisticated analysis can be performed on the selection and a model independent measurement made.

The final goal of this analysis is to measure the  $CC1\pi^+/CCQE$  cross section ratio as a function of neutrino energy on a polystyrene scintillator ( $C_8H_8$ ) nuclear target. A cross section ratio measurement was chosen over a straight cross section measurement to reduce the size of systematic errors. Many, large, systematic errors such as the flux normalisa-

tion uncertainty will cancel in the ratio calculation whilst others, such as the flux shape uncertainty, will be reduced due to correlation between samples. A ratio measurement of the  $CC1\pi^+$  cross section is more directly comparable to the CCQE measurement to which the  $CC1\pi^+$  interactions are a background. The ratio measurement is also capable of constraining the interaction models by limiting the relative cross sections. FGD1 is chosen as the target detector for several reasons. Firstly, the systematic uncertainties associated with FGD1 and TPC2 are better understood than those of the other FGD and TPC modules. This is particularly true for the B-Field distortions within the detector. Moreover, at the current time, a subtraction analysis is not possible to extract the cross-section on water and so the use of FGD2 will only introduce uncertainty as to the nature of the nuclear target.

### 6.1.1 Defining the Signals

#### $CC1\pi^+$

Nuclear re-interactions will be an important issue in any  $CC1\pi^+$  cross section measurement. Re-interactions within the nucleus such as, charge exchange, pion absorption or pion production, will obscure the initial reaction products and so the true neutrino interaction process. As such, only the particles exiting the nucleus can be detected by experiment. Therefore the most appropriate definition is an 'effective'  $CC1\pi^+$  signal that depends only on particles exiting the nucleus, not those produced in the initial neutrino interaction. For the purposes of this analysis, the signal definition is any event with the following particles exiting the nucleus:

- A single  $\mu^-$
- A single  $\pi^+$  and no other pions
- Any number of nucleons

A single  $\mu^-$  and a single  $\pi^+$  must exit the nucleus in  $CC1\pi^+$  interactions. Any number of nucleons are allowed in the final state to allow nuclear break-ups that can produce many nuclear fragments and one high energy nucleon. It is expected that only the high energy nucleon will be reconstructed with the nuclear fragments leaving little to no signal in the detector.

Bin Number	1	2	3	4	5	6	7	8
$E_\nu$ (GeV)	0-0.4	0.4-0.5	0.5-0.7	0.7-0.9	0.9-1.2	1.2-2	2-3	3-10

Table 6.1: Neutrino energy binning.

**CCQE**

True CCQE events are relatively unaffected by the nuclear effects due to the lack of strong interaction by the muon. However, events may migrate from true  $CC1\pi^+$  to CCQE-like through pion absorption, this must be taken into account in the signal definition. Therefore, the definition of the CCQE signal used in this analysis is:

- A single  $\mu^-$
- 0 pions
- Any number of nucleons
- No other hadrons

As above, the presence of a single  $\mu^-$  is indicative of a  $CC\nu_\mu$  interactions. No pions are allowed to exit the nucleus as the interaction would then be classed as a single/multi pion interaction. Any number of nucleons may exit the nucleus but no other form of hadron.

**6.1.2 Event Binning**

The events in each selection are binned by neutrino energy,  $E_\nu$ . The bin boundaries are chosen so that the flux does not change too rapidly within a bin and thus gives finer binning around the peak neutrino energy. Sample statistics were also a consideration in choosing the event binning. The statistics in the  $CC1\pi^+$  selection are low and so the binning must be wide enough that each bin is sufficiently populated in this sample. The binning is shown in Table 6.1.

**6.2 Data Sets and Monte Carlo**

This analysis uses the data collected by ND280 in Run 1 and Run 2. The total delivered POT in this period is  $1.39 \times 10^{20}$ . After data quality and beam quality cuts the data flagged

as good in both run periods is  $1.12 \times 10^{20}$  POT. This is split into,  $3.055 \times 10^{19}$  POT for Run 1 and  $8.171 \times 10^{19}$  POT for Run 2 after DQ cuts[55].

During Run 1 the neutrino beam power varied between 20-90 kW. The beam power was significantly upgraded for Run 2 data taking, consistently reaching a beam power of roughly 145kW. The data files used were produced as a part of the 4E ND280 data processing.

The MC data set used was also generated and processed as a part of the 4E ND280 processing and uses full beam simulation with neutrino interactions generated using the NEUT neutrino interaction generator. An equivalent of  $5.57 \times 10^{20}$  POT were simulated for Run 2 MC and  $1.975 \times 10^{20}$  POT were simulated for the Run 1 MC. This gives scale factors of:

$$\frac{Data}{MC_{Run1}} = 0.155 \quad (6.1)$$

$$\frac{Data}{MC_{Run2}} = 0.147 \quad (6.2)$$

### 6.2.1 Data Quality

Beam spills must meet a set of criteria to be flagged as 'good'. Each beam spill has associated with it two quality flags, the first indicates the quality of the beam spill provided by the beam group and the second is based on the status of the ND280 detector and magnet.

The ND280 data quality flag is set to 'good' if all ND280 subsystems are operating within normal parameters. The magnet flag is based on the operating current, if the current drops below 2.55 kA the data quality is marked 'bad'. The data quality for the sub-detector system is generally based on the voltage supplied, the temperatures and the online calibrations. More detail on these flags can be found in[55]. The POT before and after data quality cuts are shown in Table 6.2.

Run	Delivered POT	POT After DQ	Eff (%)
1	$0.320 \times 10^{20}$	$0.305 \times 10^{20}$	95
2	$1.08 \times 10^{20}$	$0.817 \times 10^{20}$	71.6
1+2	$1.40 \times 10^{20}$	$1.12 \times 10^{20}$	77.6

Table 6.2: The delivered POT and POT after DQ cuts.

### 6.3 Selecting Charged Current Events

A series of cuts are common to both selections. The initial cuts are designed to select beam events in the target region of interest to the analysis. The second stage is to select only charged current events from those occurring in the interaction target region. This is done by identifying the muon indicative of a CC interaction. The CC selection cuts were developed as part of the official ND280  $\nu_\mu$  analysis[30] and have been taken directly for use here. Once a CC event has been selected, further cuts have been implemented to distinguish QE and  $\pi^+$  interactions. One exception is the cut on vertex multiplicity which occurs at the same stage in each analysis.

A summary of the CC selection cuts is:

1. Vertex must be in a bunch time window
2. Vertex must be within FGD1 FV
3. Vertex Multiplicity (selection dependent)
4. Only one negative track is associated with the vertex
5. The negative track has good TPC2 track quality
6. The negative track has PID pull  $|\delta_E(\mu)| < 2$  in TPC2

Cuts 1 to 3 are those used to select events in the target region whilst the further cuts are designed to tag the muon produced in the interaction. Each cut is described and motivation given in turn. The cuts used in each selection are placed successively on each vertex in an event.

### 6.3.1 Beam Timing

The beam spills contained six proton bunches for Run 1 and eight proton bunches for Run 2. To select only beam events occurring inside of ND280, cuts are placed on the vertex timestamp. The distributions of beam induced vertices within the time bunches has a Gaussian shape. Only vertices that have a timestamp within a given range of the bunch's Gaussian mean are accepted. This cut is designed to reduce contamination from non-beam induced interactions. Example distributions of vertex timestamps in Run 2 are shown in Figure 6.1. The eight bunches can be seen clearly over the background distribution. The plot produced from beam data shows eight additional smaller peaks shifted left from the main peaks. This is due to a change in the beam trigger time during Run 2 data taking. This has been accounted for in the beam timing cut. The timing cuts are set either side of the bunch centres shown in Table 6.3 at roughly,  $\pm 64ns$  for Data and  $\pm 80ns$  for MC data. The cut is wider for MC to account for the larger bunch width.

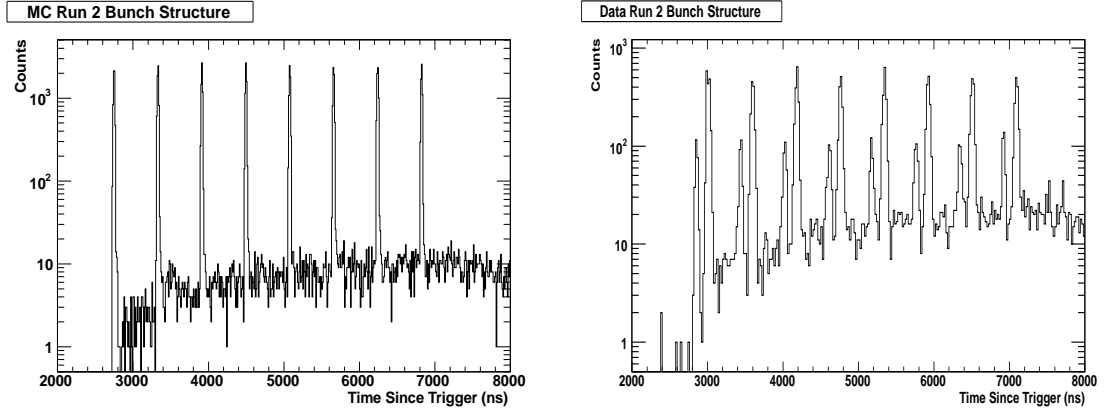


Figure 6.1: The Run 2 bunch timing structure shown for MC (left) and Data (right). The eight peaks for the beam bunches are clearly visible. In the data plot an additional eight peaks are seen, this is due to a shift in the beam trigger time during Run 2 data taking.

### 6.3.2 FGD Fiducial Volume

This analysis uses FGD1 as the target mass for the neutrino interactions, therefore some cuts must be placed on the vertex position to select only events in the desired detector. To

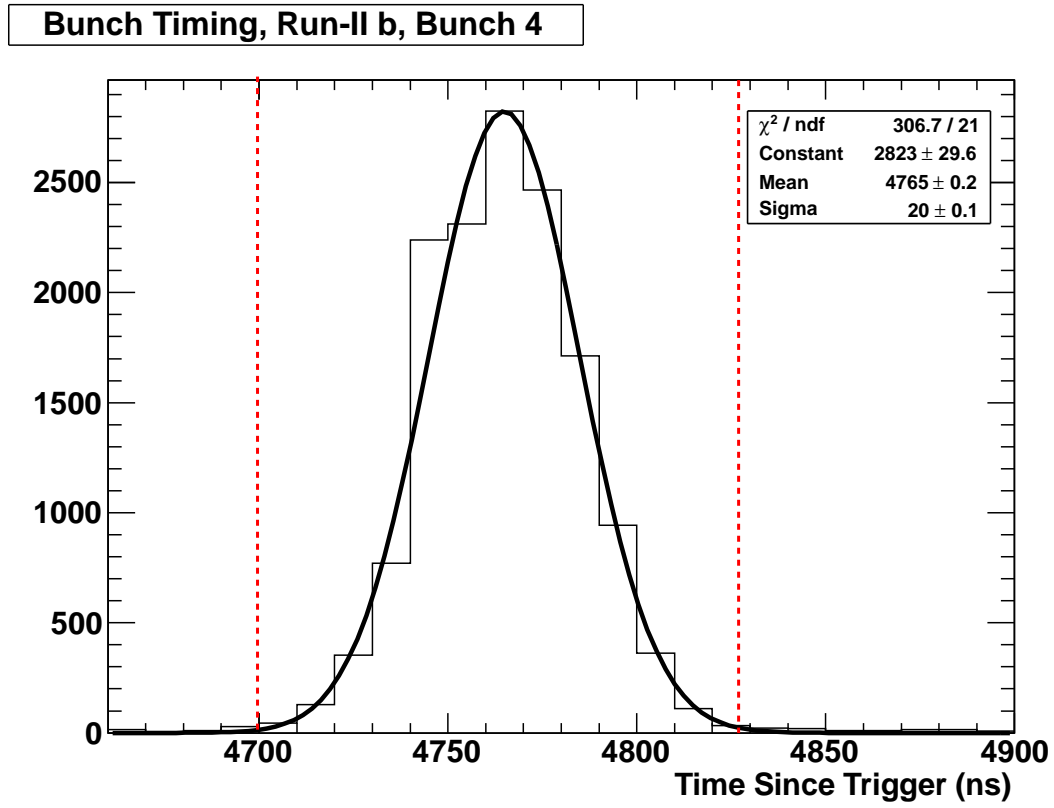


Figure 6.2: A close up of Bunch 4 taken from Run 2 data. The dotted, red lines show the positions of the bunch 4 timing cuts.

	MC	Data Run 1	Data Run 2a	Data Run 2b
JPARC Beam Run	MC	31-34	36	37-38
Bunch 1	2749	2839	2853	3019
Bunch 2	3330	3423	3444	3597
Bunch 3	3914	4005	4030	4180
Bunch 4	4494	4588	4620	4763
Bunch 5	5075	5172	5180	5346
Bunch 6	5657	5754	5770	5927
Bunch 7	6236	---	6343	6508
Bunch 8	6817	---	6924	7093

Table 6.3: Bunch positions for each data run and MC.

select neutrino interactions that occurred within the detector a fiducial volume is defined. Cutting vertices outside this fiducial volume will reduce background from cosmic rays and interactions occurring outside the FGD. The fiducial volume definition used in this analysis is the same as that used in the official T2K  $\nu_\mu$  analysis[66]. This fiducial volume is optimised in efficiency and purity of the official MC CC-Inclusive sample[67]. The use of these fiducial volume cuts also allows for easy comparison to official results from the T2K collaboration.

The fiducial volume is defined as  $|x| < 874.51mm$ ,  $|y - 55| < 874.51mm$  and  $136.875 < z < 446.955mm$ . The x and y cuts exclude the 5 outermost bar widths in the x and y planes. The offset in the y co-ordinate is due to a global offset of the centre of the FGD to the centre of the co-ordinate system. The z cuts exclude the first FGD1 XY module but includes all modules downstream of this.

### 6.3.3 Muon Identification

Any CC- $\nu_\mu$  interaction will produce an outgoing muon particle. Identifying this muon distinguishes the event from both NC and  $\nu_e$  interactions and so is the next step in both CCQE and  $CC1\pi^+$  selections. In both cases we expect only one negative track in the final state. Therefore, first cut to select CC events is that there must be one and only one negatively charged track associated with the vertex. The negative track becomes the muon candidate for vertex.

The PID, momentum and charge measurements in ND280 are performed by the TPC. The reliability of the TPC information is dependent on the length of the track in the TPC and so a track quality cut is implemented. The negative track is required to contain at least 18 vertical clusters in TPC2. All PID and momentum information is taken from TPC2 to reduce systematic uncertainties from magnetic field distortions in TPC3. TPC1 is upstream of the interaction volume and due to interaction kinematics it is expected that few, if any, muons will enter TPC1. Muon-like tracks in TPC1 are much more likely to be particles created in and exiting the POD.

To identify the negative track as a muon, the TPC PID pull is used. The PID pull is discussed in detail in Section 5.2.3. A straight cut is placed on the TPC muon pull,



requiring  $|\delta_E(i)| < 2$ .

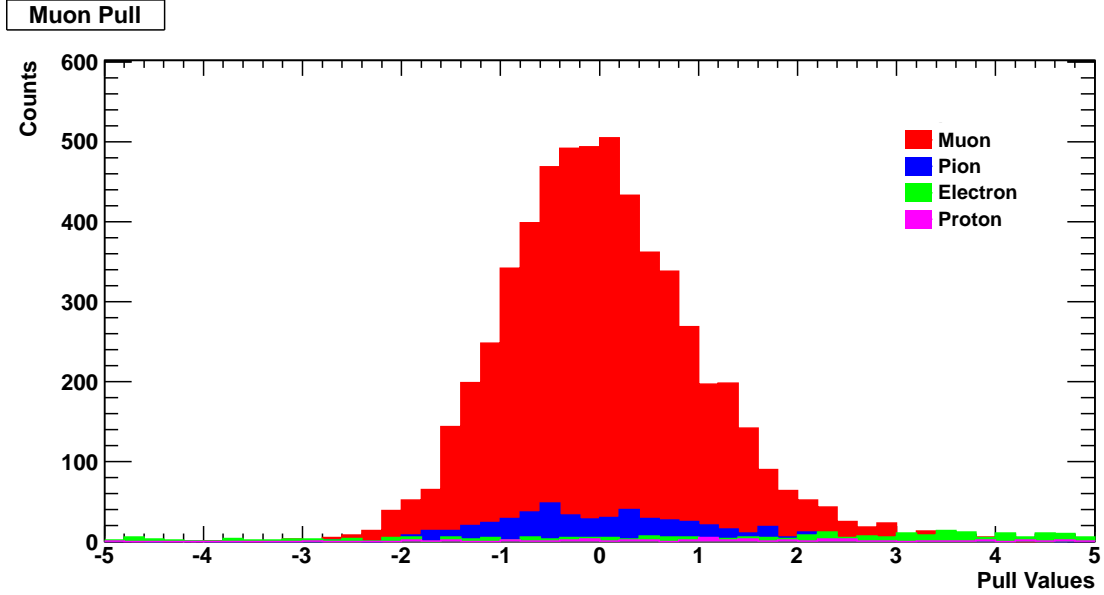


Figure 6.3: The muon hypothesis PID pull for negative tracks in TPC2 in MC. Different colours represent the true particle type. Muon signal dominates the region  $-2 < \delta_E(\mu) < 2$ .

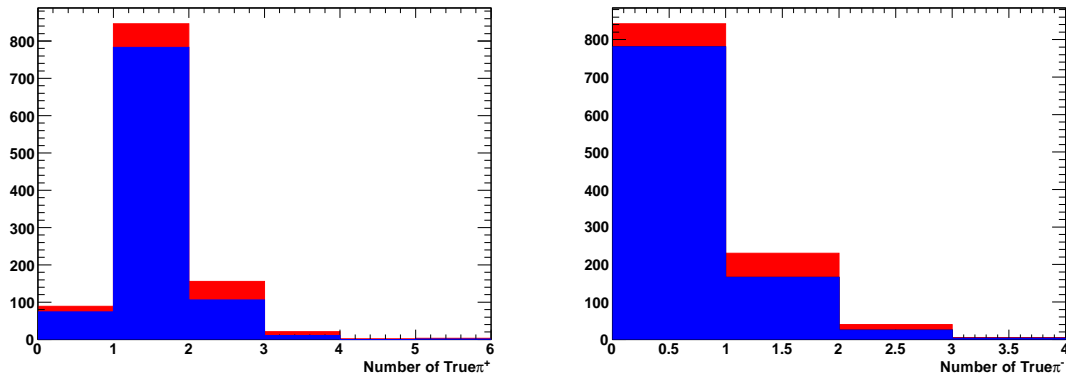
Ideally the muon pull distribution should be centred on zero and have a width of one for a pure muon sample. This however was not the case and before the pull cut can be applied the  $C_T$  scale must be corrected. The measured  $C_T$  is scaled by a given amount depending on the data run and the TPC number. The scale applied to  $C_T$  is determined by using a sample of negative tracks in beam events that pass through all three TPCs. This gives an almost pure muon sample from which the necessary correction factor can be extracted. Figure 6.3 shows the muon pull for negative tracks and the true particle types for those tracks.

#### 6.3.4 Veto Cuts

These vetoes are the final cuts made in each selection but are common to both the CCQE and  $CC1\pi^+$  selection cuts. These cuts are designed to reject various background as will be described.

### FGD-TPC Track Multiplicity

A cut is placed on the number of tracks reconstructed in the tracker. We search for additional tracks that start in the FGD FV during the same beam bunch as the vertex. Events are then cut if there are more tracks in the FGD than are associated with the vertex or other FGD activity. The intention of this cut is to remove events where the reconstruction has missed a track that should be associated with a vertex. This typically happens at higher multiplicities where the final tracks must have very low chi-squared values to pass the cuts. The relative efficiency of this cut is 95% and a 6% increase in purity is achieved for the  $CC1\pi^+$  selection. For the  $CCQE$  selection we find a relative efficiency of 98.1% and a 2.2% increase in purity. Figure 6.3.4 illustrates the signal and background removed in MC by this cut.



### ECAL Activity

The ECal reconstruction during production 4 processing was not fully optimised and included mapping errors and un-validated PID in the barrel modules. Preliminary studies were performed using DsECAL testbeam data on the discrimination of muons and pions. This discrimination is possible in the ECal if the pion starts to shower. However, this only occurs for roughly 50% of pions setting a hard limit on the efficiency of such PID. Due to the low statistics of the data sample such an efficiency loss would not be viable in this study.

Although using ECal PID information was deemed unviable, the ECal could be used as a veto to reject backgrounds. The intent of this cut in the  $CC1\pi^+$  selection is to reduce the

multiple pion, neutral pion and inelastic backgrounds. The effect of this cut in the selections is to reject events where the global track matching between the tracker and the ECals has failed or the tracker reconstruction fails to reconstruct pions exiting the detector. The cut also removes events with a large number of neutral clusters which are more indicative of an inelastic scattering event than a  $CC1\pi^+$  event. The probability of undetected pions is much higher in inelastic events and so cutting them increases sample purity.

First, the number of ECal hits clusters in the same time bunch as the vertex is counted. Any cluster with total energy deposit below a noise threshold is not counted. The vertex tracks are then extrapolated to the ECal surfaces using RecPack. Any ECal clusters within 35 mm of the extrapolated track's entrance position are removed from the count. If more than three clusters are found, the event is cut. This cut increases the selection's purity by 5% to 70% and has a relative efficiency of 87.5%.

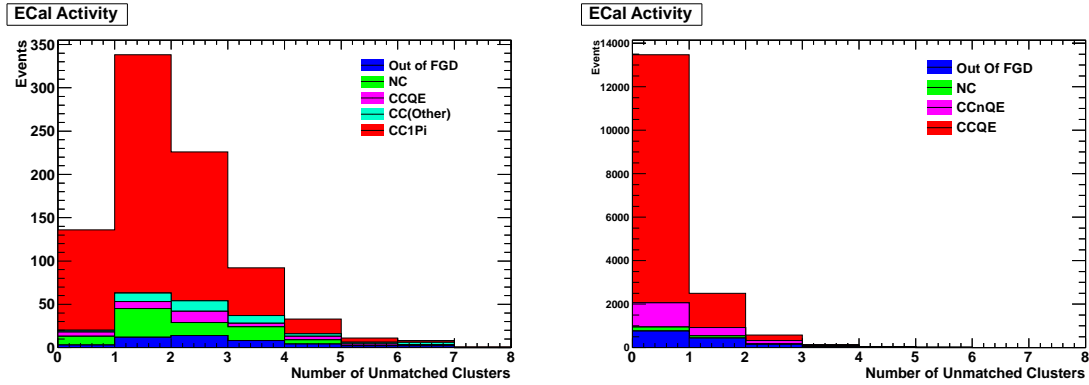


Figure 6.4: The distribution of the number of unmatched ECal clusters in an event for the  $CC1\pi^+$  selection (right) and the CCQE selection (left).

## 6.4 CCQE Event Selection

The CCQE selection used in this analysis follows the official ND280  $\nu_\mu$ -CCQE selection detailed here[66] closely and is not the main focus of this analysis. However, three additional, activity veto cuts have been used in this analysis. Two of these veto cuts are common to both the CCQE and  $CC1\pi^+$  selections. The cuts used are listed below in sequential order:

1. Vertex must be in a bunch time window and within the FGD FV

2. Vertex must have no more than 2 associated tracks
3. Only one of these tracks is negative
4. The other track must stop within FGD1
5. The negative track has good TPC2 track quality
6. The negative track has an absolute muon pull less than 2
7. There must be no Michel electron signal in FGD1
8. Tracker Multiplicity less than 2
9. Unmatched ECal clusters less than 1
10. Number of P0D tracks less than 1

## **2.)Vertex Multiplicity Cut**

Cuts one and two have previously been discussed. Cut two places a restriction on the number of tracks associated to the vertex. For a QE interaction we expect at most two outgoing particles, a  $\mu^-$  and a recoil proton, therefore we expect at most two reconstructed tracks associated with the vertex. It is not expected that multiple nucleons will be energetic enough to leave tracks in the FGD.

## **4.)Recoil Proton**

After one of the tracks has been selected as the muon candidate a cut is placed on the other track requiring that it stops within the FGD. This second track is expected to be a recoil proton in a CCQE event. Recoil protons are heavy and generally have low momentum, thus, they are far less likely to enter the TPC than pions. This simple cut effectively tags protons and rejects pions.

## **7.)Michel Electron cut**

A CCQE interaction should have no Michel electrons associated with it. Michel electron is the name given to an electron produced in the decay of a stopped muon. Any muons

produced in the decay of a stopped pion will stop within the detector themselves and thus create a Michel electron. Therefore, the presence of a Michel electron signal indicates that one or more unseen pions were produced or that the track stopping in the FGD was a pion rather than a proton. The Michel electron signal is created from time delayed hits in the FGD. The hits for a Michel electron signal must be neighbouring, within 100 ns of each other and deposit at least 200 p.e. of charge. The Michel signal must also be outside of the beam time windows to avoid false signals caused by beam events.

### 10.)P0D Veto

A veto is placed on activity inside the P0D in the CCQE selection. This is to reduce the background from interactions which occur inside the P0D but are incorrectly identified as starting in the FGD-FV. This background is only large in the single track category of events and thus is only included in the CCQE selection. This veto was used in the ND280  $\nu_e$  analysis[68] but has a beneficial effect and so has been added to this  $\nu_\mu$  analysis. The cut simply requires no tracks to be found in the P0D in the same bunch as the FGD vertex.

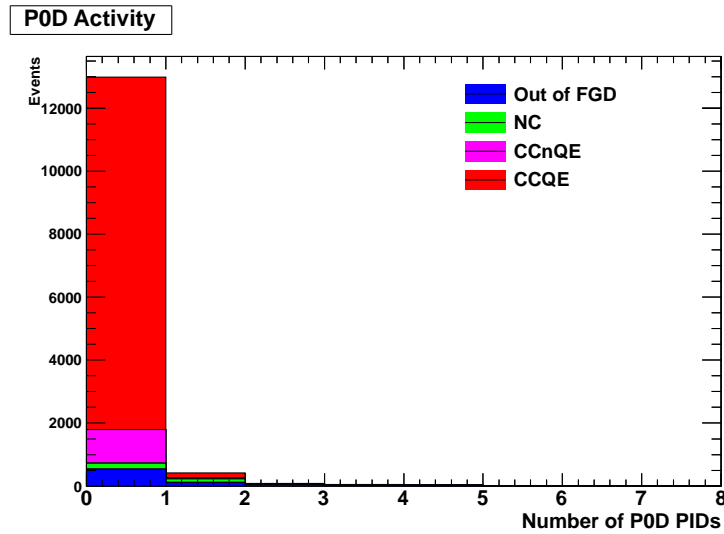


Figure 6.5: The distribution of the number of P0D tracks in an event.

#### 6.4.1 CCQE Overview

There are several measures of the selection performance available. Figure 6.6 to Figure 6.12 show how the kinematic distributions of the muon change with the successive cuts

in the selected CCQE events in MC. These plots show that no regions of phase space are being unintentionally excluded by the cut. It shows that the TPC track quality cut removes the majority of the events in the first  $P_\mu$  bin. These events are those where the muon does not enter the TPC or does not leave a long enough track to be reconstructed properly. We can see that the  $\cos\theta_\mu$  distribution remains unchanged in shape for this cut. The veto cuts greatly reduce the out of FGD background. At this point the  $CC1\pi$  background is largely irreducible. Figure 6.13 shows the true momentum and true trajectory length of the final state pions after all selection cuts have been applied. The momentum distribution peaks below 200 MeV and few of these pions reach the TPC. It is currently not possible to distinguish between pions and protons in FGD only tracks and so there is no way to remove this low momentum pion background. Finally, Figure 6.14 shows how the efficiency and purity change with the successive cuts.

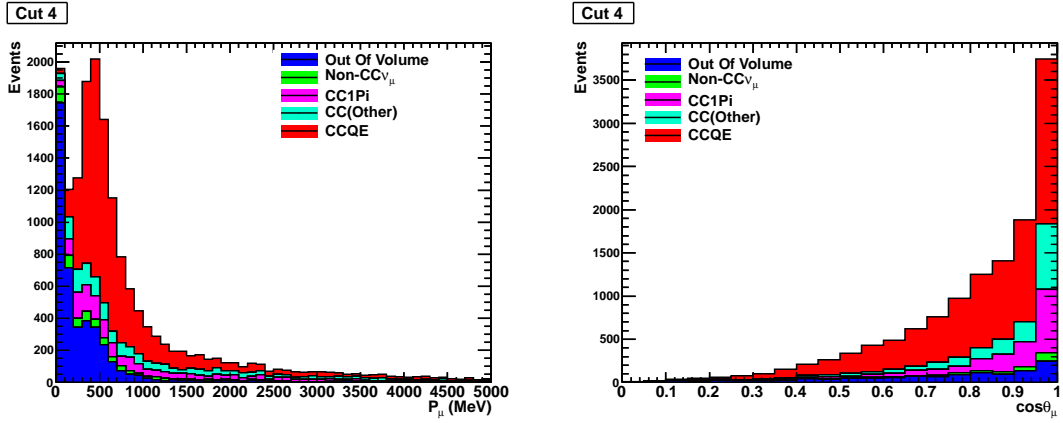


Figure 6.6: Distributions for  $P_\mu$  (left)  $\cos\theta_\mu$  (right) after cut 4 has been applied. This is the requirement that the recoil track stop in the FGD.

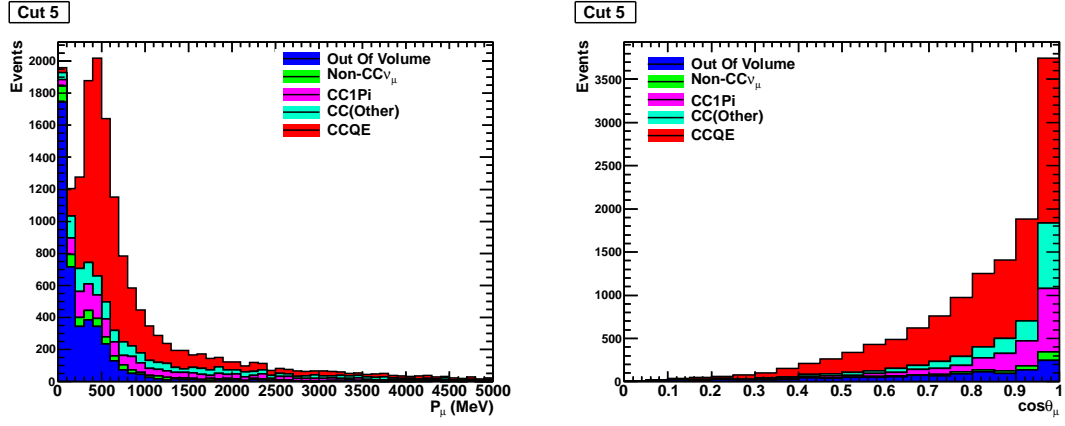


Figure 6.7: Muon kinematic distributions after applying the negative track requirement in the CCQE selection.

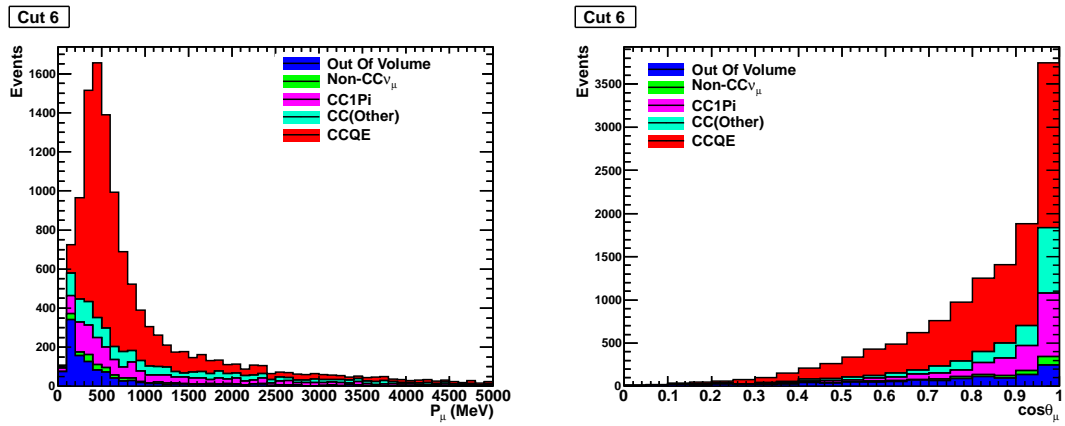


Figure 6.8: Muon kinematic distributions after applying the Muon Pull cut in the CCQE selection.

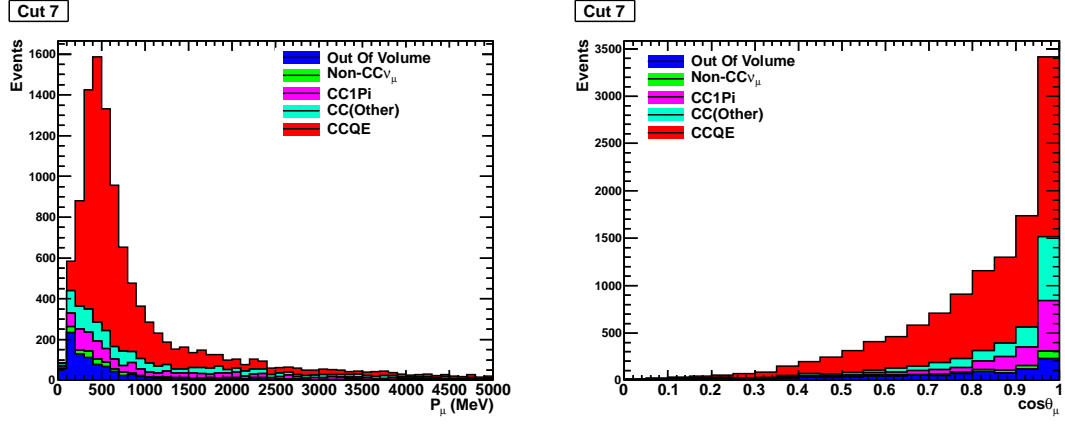


Figure 6.9: Muon kinematic distributions after applying the Michel electron cut in the CCQE selection.

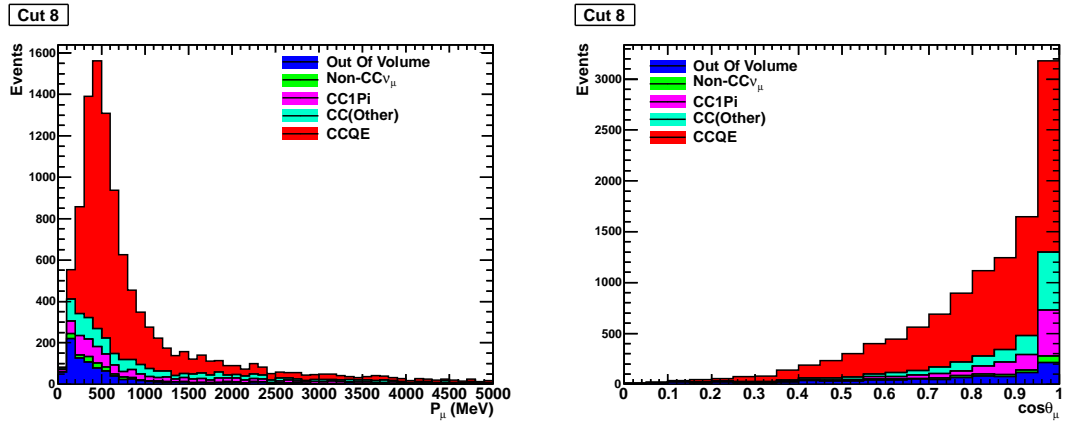


Figure 6.10: Muon kinematic distributions after applying the FGD-TPC activity cut in the CCQE selection.



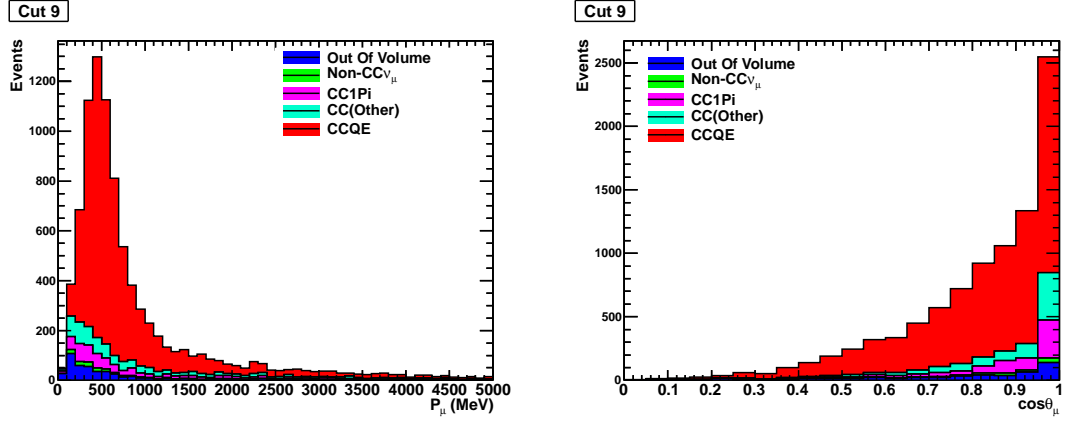


Figure 6.11: Muon kinematic distributions after applying the ECal activity veto in the CCQE selection.

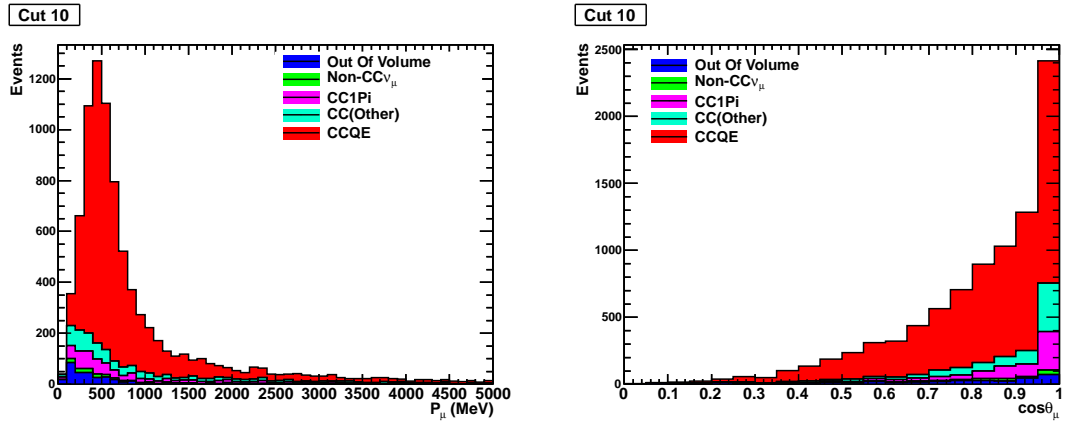


Figure 6.12: Muon kinematic distributions after applying the POD activity veto in the CCQE selection.

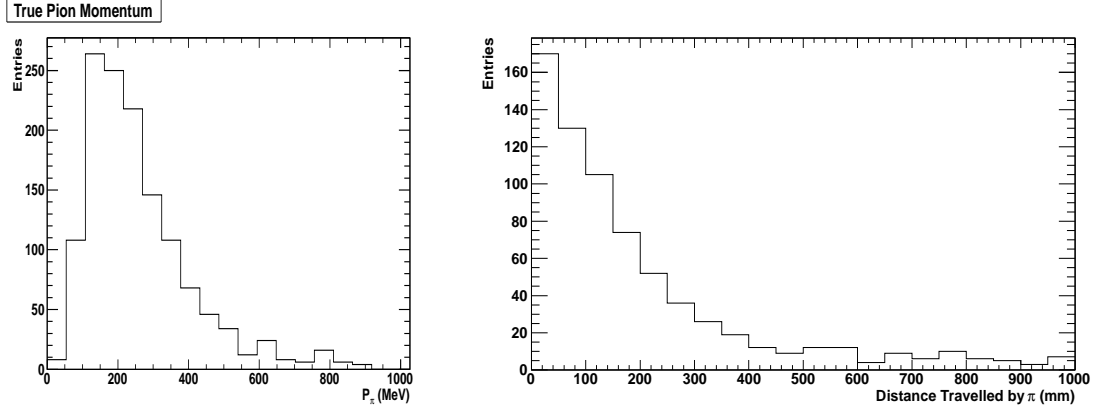


Figure 6.13: Left) The pion momentum spectrum for final state pions in events that pass all CCQE selection cuts. Right) The length the pion travelled according to MC. The FGD is 365 mm deep, implying that most of the pions stop in the FGD and would therefore be tagged as protons with no further PID available at this stage.

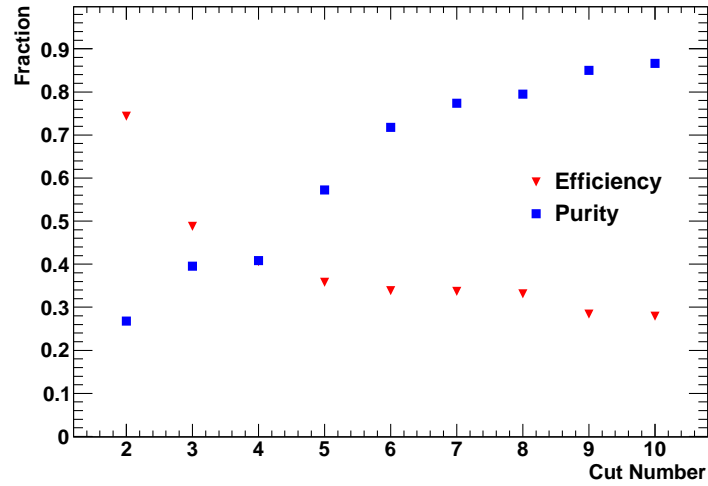


Figure 6.14: The efficiency and purity of the CCQE selection by cut number.

## 6.5 $CC1\pi^+$ Event Selection

The selection of  $CC1\pi^+$  events follows the cuts described in section 6.4 with the addition of three further cuts to select pions and three veto cuts to eliminate out-of-volume backgrounds and backgrounds from deep inelastic scattering events. The full chain of cuts for the  $CC1\pi^+$  selection are:

1. Vertex must be within FGD1 FV and Vertex must be in a bunch time window
2. Vertex must have 2-3 associated tracks
3. Only one of these tracks is negative
4. The negative track has good TPC2 track quality
5. The negative track has an absolute muon pull less than 2
6. One of the positive tracks must have good TPC quality, with absolute pion pull less than 3 and absolute proton pull greater than 2
7. Tracker Multiplicity less than 3
8. Number of unmatched ECal clusters less than 3

### 3.)Vertex Multiplicity

The track multiplicity for a  $CC1\pi^+$  interaction is two or more dependent on the detection of recoil nucleons. However, as the track multiplicity increases, the fraction of single pion events decreases and multi pion and inelastic scattering fractions increase. Therefore, to reduce these backgrounds, only vertices with 2-3 tracks are considered, allowing only a single recoil nucleon.

### 6.)Pion Selection

The cuts to select the pions are similar to those used previously to select the muon. We apply a series of cuts to the positive track(s). Firstly, a cut on TPC track quality is made, i.e. the track must have a TPC component with greater than 18 segments. This cut is

necessary to ensure the PID information used is reliable. Next, a TPC PID cut is applied. To be tagged as a pion the track must have an absolute pion pull less than three and a proton pull greater than two. The cut on the pion pull is to select only MIP-like particles. The cut is wider than that used on the muon pull to increase the acceptance of the cut. Widening the pull to three sigma improved the efficiency of this cut whilst having a negligible effect on the sample purity. The cut on proton pull is to remove background from the small number of protons that reach the TPC. These protons are usually from inelastic scattering events but a small number originate from CCQE-like events. Being the dominant type of positive particle produced in the neutrino interaction at ND280, protons form the biggest background to pion identification. Using the proton and pion pull cuts together reduces the major background in the selection, allowing the pion pull cut to be wider than the pull cut to identify the muon.

If a track passes all three cuts it is tagged as pion-like. The number of pion-like particles is counted and a cut is performed, where only vertices with a single pion-like track are selected. This attempts to select only single pion events whilst rejecting multi pion and inelastic events. It also rejects a small number of QE events.

### **6.5.1 $CC1\pi^+$ Overview**

Figure 6.15 to Figure 6.20 shows how the muon momentum distribution changes throughout the selection. The plots are divided into their signal and background fractions showing the purity increase with successive cuts. Figure 6.21 shows how the purity and efficiency of the selection change by cut.

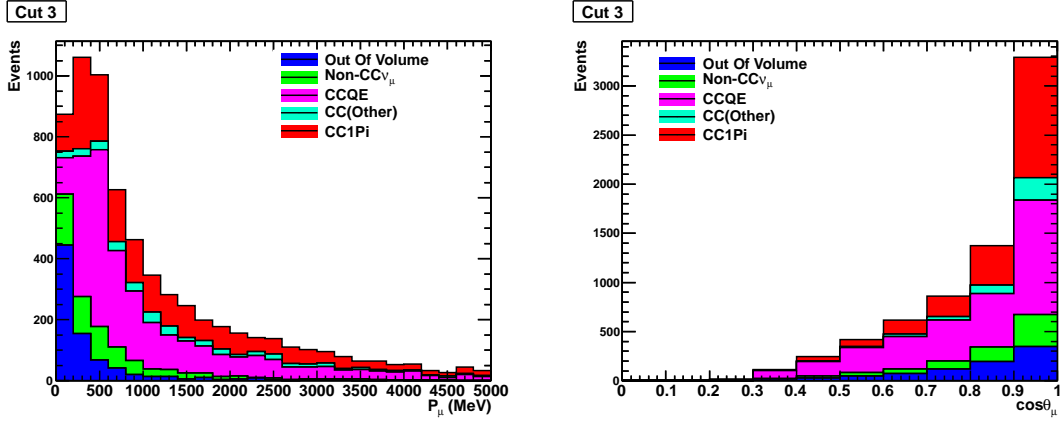


Figure 6.15: Distributions for  $P_\mu$  (left)  $\cos\theta_\mu$  (right) after the  $CC1\pi^+$  cut requiring only a single negative track.

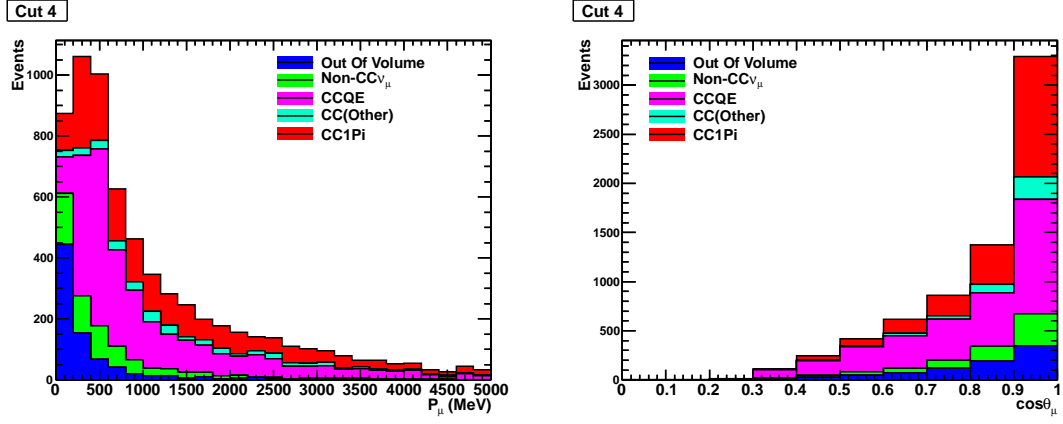


Figure 6.16: Muon Kinematic distributions after the  $CC1\pi^+$  cut requiring the negative track has good TPC quality for the  $CC1\pi^+$  selection.

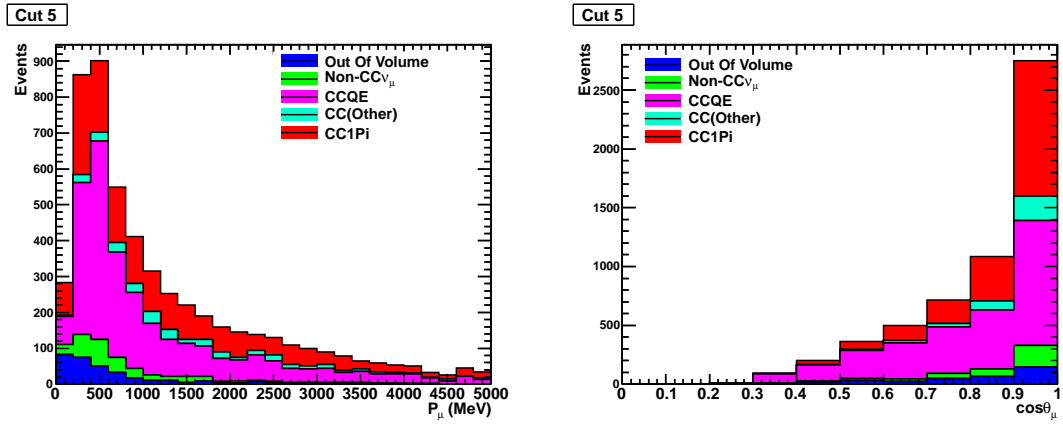
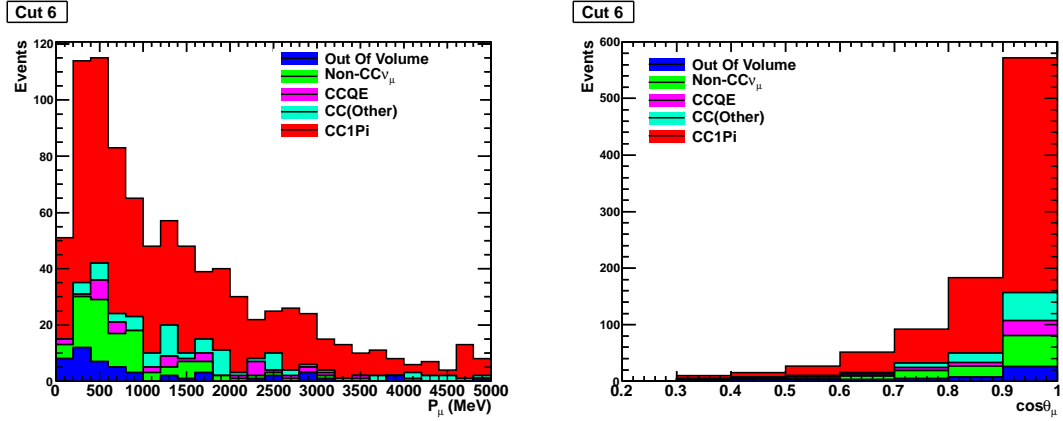
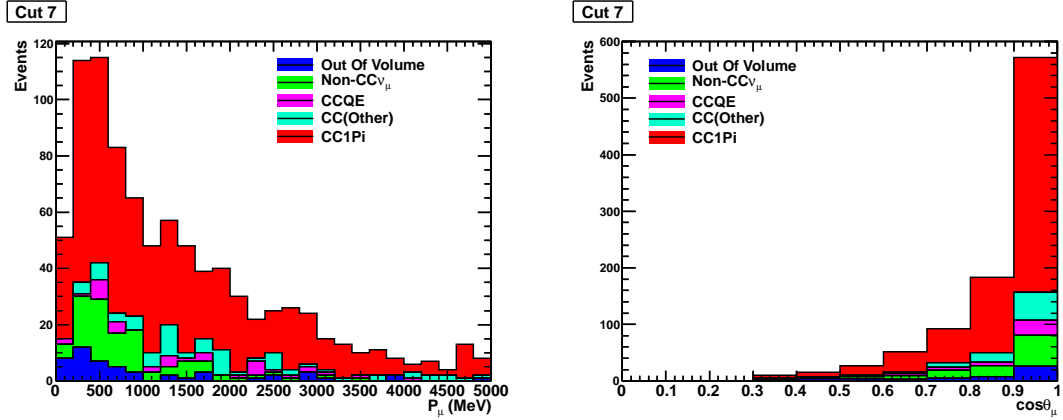
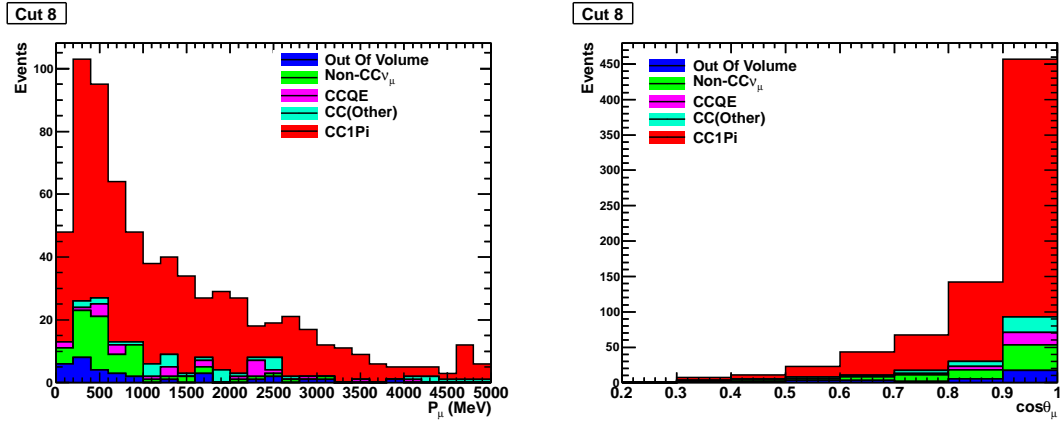


Figure 6.17: Muon Kinematic distributions after the  $CC1\pi^+$  muon pull cut.

Figure 6.18: Muon Kinematic distributions after the  $CC1\pi^+$  single pion selection cut.Figure 6.19: Muon Kinematic distributions after the  $CC1\pi^+$  FGD-TPC track multiplicity cut.Figure 6.20: Muon Kinematic distributions after the  $CC1\pi^+$  ECal activity cut.

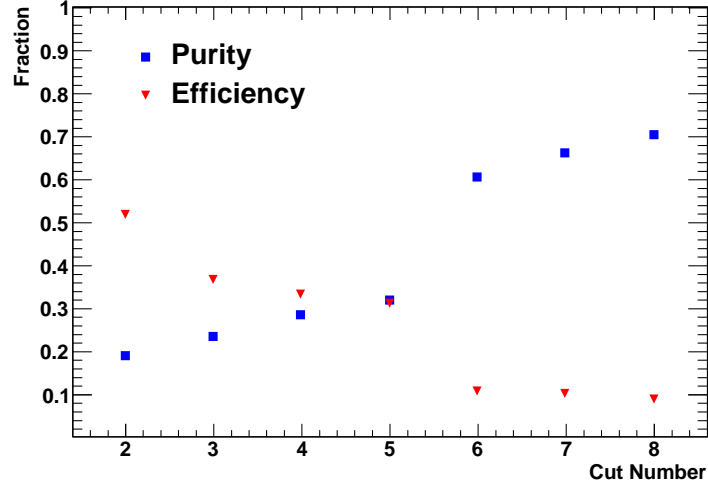


Figure 6.21: The efficiency and purity of the  $CC1\pi^+$  selection by cut number.

## 6.6 Neutrino Energy Reconstruction and Ratio Calculation

For the selected CCQE events we use the muon 4-momentum to reconstruct the neutrino energy. In the majority of cases, the proton momentum is not reconstructed and so is not available to use in the energy reconstruction. In reconstructing the neutrino energy, we assume a 2-body quasi-elastic scatter process with the target nucleon at rest and use,

$$E_\nu^{QE} = \frac{2m_n E_\mu - m_\mu^2}{2(m_n - E_\mu + |P_\mu| \cos \theta_\mu)} \quad (6.3)$$

where  $m_n$  and  $m_\mu$  are the neutron and muon mass respectively and  $E_\mu, |P_\mu|, \theta_\mu$  are the energy, 3-momentum magnitude, and angle between the z-axis and the trajectory of, the muon.

For  $CC1\pi^+$  events we have both the muon and the pion kinematics available to reconstruct the neutrino energy. We once again assume that the target nucleon is at rest. We also assume that the third particle is a nucleon. Using 4-momentum conservation we find,

$$E_\nu^{CC1\pi} = \frac{m_\mu^2 + m_\pi^2 - 2m_N(E_\pi E_\mu) + 2P_\mu \cdot P_\pi}{2(E_\mu + E_\pi - |P_\mu| \cos \theta_\mu - |P_\pi| \cos \theta_\pi - m_N)} \quad (6.4)$$

where  $m_N$  is the nucleon mass,  $P_{\mu,\pi}$  are the four momenta of the muon or pion and the

other symbols retain their meaning from the previous equation and the subscript denotes the particle.

In order to calculate the ratio, several quantities must be taken from MC. Firstly, the background expectation must be determined for each selection. This is done by using the true information in the MC to identify how many background events were selected in a given neutrino energy bin. The number of background events is then scaled to data POT. The efficiency with which we select events is also taken from MC. The efficiency is taken to be,

$$\epsilon_i = \frac{N_i^{Sel}}{N_i^{Total}} \quad (6.5)$$

where  $\epsilon_i$  is the efficiency in a given bin,  $N_i^{Sel}$  is the number of signal events selected in bin  $i$  and  $N_i^{Total}$  is the true number of signal events in bin  $i$ . These quantities are all taken from MC.

We then use these values to predict the number of events present in the data sample from the number of events selected in the data. To do this, for each bin, the background expectation is subtracted to leave a sample of expected signal events. The sample of expected signal events is then divided by the efficiency to select signal events to give,

$$N_x = \frac{N^{Sel,Data} - Bg^{scaled,MC}}{\epsilon} \quad (6.6)$$

where  $N$  is the predicted number of events of type  $x$ ,  $N^{Sel,Data}$  is the number of events selected in data as being of type  $x$ ,  $Bg^{scaled,MC}$  is the expected number of background events scaled from MC and  $\epsilon$  is the MC efficiency of selecting  $x$ -type events.

The cross-section of a process is defined as,

$$\sigma_x = \frac{N_x}{\phi_\nu T N_{Targets}} \quad (6.7)$$

where  $N_x$  is the number of  $x$  type events,  $\phi_\nu$  is the neutrino flux,  $T$  is the duration of the neutrino flux and  $N_{Targets}$  is the number of nuclear targets. However,  $\phi_\nu, T, N_{Targets}$  are all fixed variables within the experiment and so will be common to both processes. This



means that when calculating the ratio all variables cancel except for  $N_x$  giving,

$$R = \frac{\sigma_{CC1\pi^+}}{\sigma_{CCQE}} = \frac{N_{CC1\pi^+}}{N_{CCQE}} \quad (6.8)$$

Substituting Equation 6.6 and labelling each energy bin  $i$ , then gives,

$$R_i = \frac{\epsilon_i^{QE}}{\epsilon_i^{CC1\pi}} \frac{N_i^{Sel,CC1\pi} - Bg_i^{MC,CC1\pi}}{N_i^{Sel,CCQE} - Bg_i^{MC,CCQE}} \quad (6.9)$$

## 6.7 Detector and Reconstruction Systematics

A number of systematic errors have been considered during the analysis. The final goal of this analysis is a cross section ratio and so, where possible, the effects of the systematic uncertainties have been calculated directly for the ratio rather than for the two separate selections. This ensures that any partial cancellation of systematic uncertainties will be treated accordingly and will not be artificially inflated or reduced when calculating the ratio. Most of the methods used for calculating and propagating these errors come from studies performed for the official ND280  $\nu_\mu$  and  $\nu_e$  analyses. The method used will be briefly explained for each error.

### 6.7.1 TPC Track Finding Efficiency

Losing a TPC track to inefficiency can cause both event loss and event migration between selections. In the case that the pion track is lost, the event will appear to be CCQE-like and thus the event will be migrated from the  $CC1\pi^+$  selection to the CCQE selection. Finally, the loss of additional tracks in high multiplicity events can also cause the acceptance of additional background if a second pion is created but the track is lost due to inefficiency. Any difference in the rate of these processes between data and MC will effect a systematic uncertainty in the final measurement.

The systematic uncertainty on this process is taken from a previous study into the track finding efficiency[69]. The study used a sample of through going muons from both beam events and cosmic triggers. The efficiency of TPC2 was measured by selecting events with a track in both TPC1 and TPC3. The TPC1 and TPC3 tracks must have  $\leq 60$  nodes and

energy deposit compatible with a muon, i.e.  $|\delta_E(\mu)| < 2.5$ . Finally the tracks are required to extrapolate into TPC2 to ensure the event is a through going muon and not a random coincidence of two tracks. The track finding efficiency is then calculated based on how many of these events contain a TPC2 track with more than eighteen nodes. The efficiency is then binned in momentum and the systematic uncertainty is conservatively taken as the quadratic sum of largest difference between data and MC and their statistical errors. The uncertainty is found to be 0.5%.

To evaluate the effect of this systematic, 50 MC toy experiments were performed where 0.5% of all tracks were artificially removed in each event. The systematic error assigned to each bin in the ratio is then taken to be the spread of the ratio measurement over the 50 toy experiments. There is no mechanism to randomly create additional tracks within an event and so this error is taken to be symmetrical. The error values are given in Table 6.7. Figure 6.22 shows the spread obtained for a set of toy MC experiments for reference.

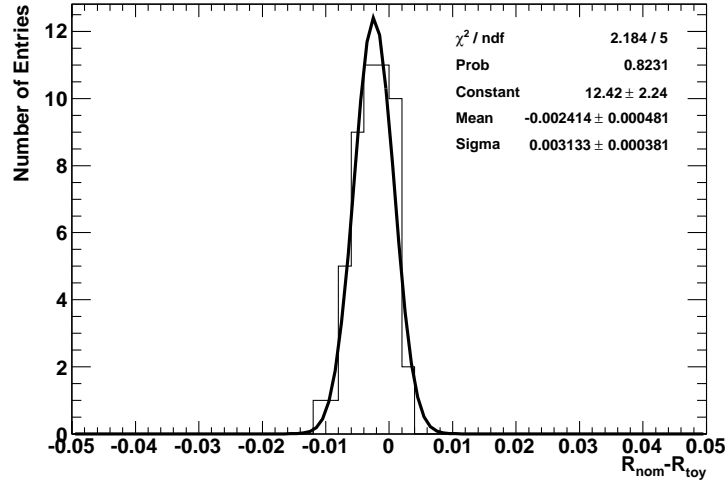


Figure 6.22: The spread in the ratio obtained from a set of toy experiments to determine the effect of the TPC tracking efficiency systematic. The plot shown is for nergy bin 6.

### 6.7.2 TPC Broken Tracks

The TPC broken track systematic is described in [69]. This systematic is due to a mode of reconstruction failure where a single track produces two or more TPC tracks. In general these tracks will be matched to some FGD hits. When a muon or pion track is broken, a

second muon-like or pion-like track will be produced and cause the event to be rejected. A study into this effect measured a 0.6% effect on TPC tracks. The statistics of the sample were limited and so the effect was not binned in track momentum or angle. The effect of this track was calculated in the same manner as the TPC tracking efficiency systematic.

### 6.7.3 FGD-TPC Matching Efficiency

Much of the tracker reconstruction relies on TPC tracks being matched to FGD hits. The drift time of electrons in the TPC are of order microseconds and so much larger than the beam spill widths. FGD hits are used to determine the T0 of TPC tracks accurately. Failures in T0 measurements cause the TPC-FGD matching to fail. The failure of this matching can prevent the track being matched to a vertex and so lost for the purposes of the vertex selection cut. The size of this systematic uncertainty is measured in a previous study[69] and is taken to be 0.4% for all track angles and momenta. The loss of tracks in this manner will have the same effect on event migration as the track loss due to TPC inefficiency. A set of 50 toy MC experiments were performed where tracks were randomly removed from vertices. The systematic associated with this is taken to be the mean difference between the toy experiments and the nominal ratio values. Again, this error is taken to be symmetrical.

### 6.7.4 Charge Confusion

Charge confusion affects both the CCQE and  $CC1\pi^+$  selections. In this CCQE selection the main effect will be to cause signal events to be rejected as the muon is reconstructed with a positive charge. In the  $CC1\pi^+$  selection there can be multiple effects. Once again, the muon may be reconstructed with a positive charge and thus the event will be rejected. Also, a pion may be reconstructed with the wrong charge, causing the event to be rejected in the case of  $\pi^+$  production or causing a background event to be accepted in the case of  $\pi^-$  production.  $\pi^-$  production is somewhat infrequent however and the effect due to this will be small.

A charge confusion study was performed using a sample of through going muons in beam data[70]. Tracks were selected starting in the P0D fiducial volume and traversing all three TPCs. By requiring all three TPCs, almost all backwards going and mismatched tracks are removed from the selection reducing the uncertainty on the charge confusion

Momentum (GeV)	Charge Confusion (%)				
	0 – 1.3	1.3. – 2.6	2.6 – 4.0	4.0 – 5.3	> 5.3
Data	$0.75 \pm 0.20$	$1.8 \pm 1.2$	$2.8 \pm 1.2$	$6.0 \pm 3.0$	$10.5 \pm 2.4$
MC	$0.55 \pm 0.09$	$2.1 \pm 0.3$	$5.1 \pm 0.8$	$5.4 \pm 1.2$	$13.0 \pm 0.18$

Table 6.4: The probability of charge confusion for long tracks in data and MC as a function of track momentum. The values shown are for TPC2.

rates. The charge confusion probability can be extracted by comparison of the three charge measurements. The probabilities for charge confusion are shown in Table 6.4. To evaluate the size of the systematic error introduced by this effect, a set of 100 toy MC experiments was performed where the charge of tracks was randomly flipped. For each momentum bin a Gaussian distribution was created with a mean of zero and a width equal to the quadratic sum of the data to MC probability difference plus the statistical error on the measurement the probabilities. Each MC experiment then drew a random number from the Gaussian distributions to use as the probability of charge confusion. The systematic error on the ratio is then taken as the width of the ratio measurements from the toy experiments.

### 6.7.5 Michel Electron Tagging

Michel electron tagging is only used in the selection of CCQE events and so the systematic error is calculated for the CCQE selection and propagated through to the ratio measurement. This error has two components. This first is due to a random coincidence faking a Michel electron signal and thus causing the event to be rejected. The second is due to the probability that a Michel electron signal is missed and a background event is accepted. The systematic errors due to both these effects were previously investigated using a sample of stopping cosmic rays and empty beam spill triggers[71].

Using the cosmic ray sample, the cut is found to have detection efficiencies of  $(59.3 \pm 0.4)\%$  and  $(64.2 \pm 0.4)\%$  in data and MC respectively. The Michel electron cut in the CCQE selection removes 7.39% of the events in the MC. From this and the measured data-MC efficiencies, it is expected that  $(6.83 \pm 0.21)\%$  of events will be removed by the cut in the data. In actuality the cut removes 7.37% of events from data, giving a systematic error of 0.54%.

The empty beam spill sample was used to evaluate the uncertainty due to the acciden-

tal coincidence. By selecting only empty beam spills any real Michel electron signals are removed leaving only background events in the out of bunch time periods. Random coincidence was found to cause  $(0.15 \pm 0.008)\%$  of signal events to be rejected in data and  $(0.0339 \pm 0.0004)\%$  in MC. Taking the quadrature sum of the difference and it's error gives a final uncertainty of 0.116%.

### 6.7.6 Vertex Reconstruction

So far there has been no evaluation of the systematic uncertainty due to the vertex reconstruction. It is not possible to determine the true vertex location in real data and so the calculation of this systematic relies purely on the MC. Uncertainties in the Vertex resolution could cause events to migrate into and out of the fiducial volume. The vertex resolution in the X and Y positions were found to be symmetrical and identical between the vertex finding methods as shown in Figure 6.23. Therefore any systematic error from the X and Y vertex resolution will cancel in the taking of the ratio. Therefore, this analysis only evaluates the effect of the Z position resolution where a significant difference was observed between the two methods.

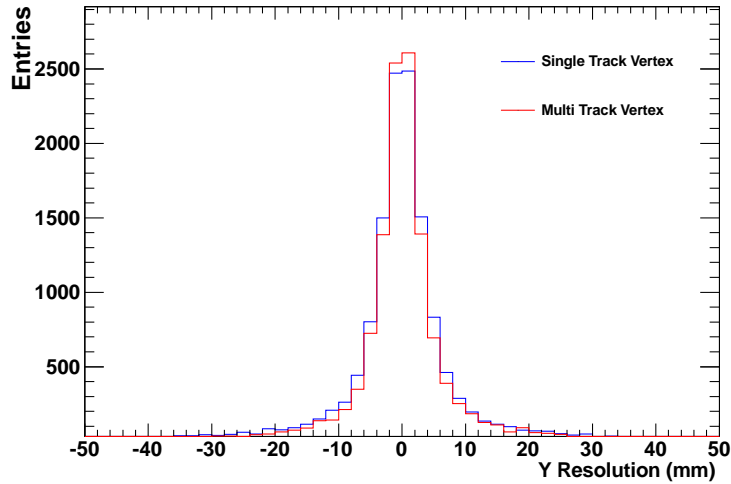


Figure 6.23: Comparing the Y position resolution for the single and multi track cases.

In order to evaluate this source of uncertainty, the vertex resolution was compared for both the single track and multiple track cases. The  $1\sigma$  vertex Z position resolution was

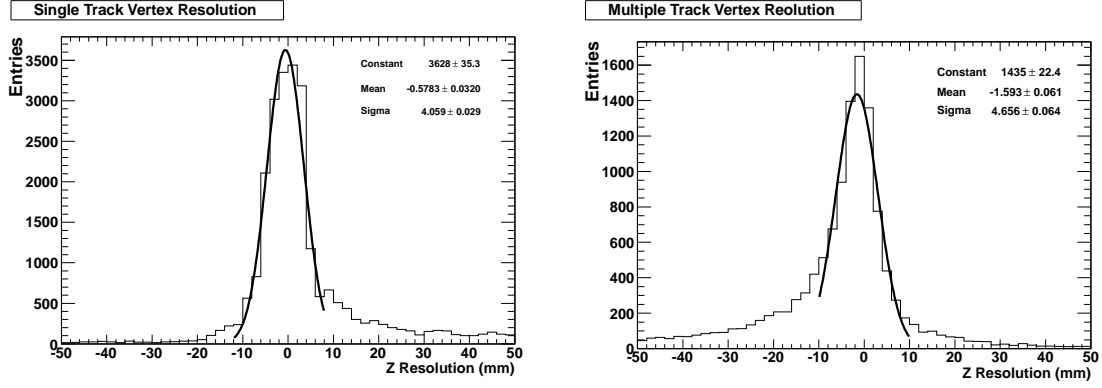


Figure 6.24: Vertex Z Resolution for the single track case (left) and the multi track case (right).

found to be  $4.6\text{mm}$  for the multiple track vertices and  $4.0\text{mm}$  for the single track vertices as shown in Figure 6.24. A set of 50 toy MC experiments were performed where each reconstructed vertex Z position was smeared by a Gaussian with mean 0 and width equal to the vertex Z resolution. The effect of this smearing is too small to be reliably calculated in each bin and so it is calculated as an overall effect on the un-binned ratio. As per the usual method, the RMS of the ratios from the toy experiments was taken to be the systematic uncertainty on the measurement and was found to be 0.9%.

### 6.7.7 TPC PID

There remain differences in the TPC calibration at the end of the processing chain due to various effects[72]. To correct for this, a correction factor is applied to the  $C_T$  of the tracks. This correction factor is dependent on the run period being analysed. The correction factors are calculated using a selection of beam events containing a single, negative track reconstructed in the tracker with more than 35 TPC hits and a momentum over 200 MeV. These selection criteria give a sample of MIP-like tracks that is over 99% pure. The  $C_T$  measured in these tracks was corrected to the expected  $C_T$  for muons. This correction is taken to be the correction factor.

A further source of systematic error is the difference in the pull widths between data and MC as shown in Table 6.5. Any difference in the pull widths will result in different efficiencies for the PID cuts. An additional Gaussian smearing is applied to the pull of

Run Number	Pull Width	
	Data	MC
1	$1.024 \pm 0.001$	$0.951 \pm 0.001$
2a	$0.981 \pm 0.001$	$0.948 \pm 0.001$
2b	$0.972 \pm 0.001$	$0.948 \pm 0.001$

Table 6.5: A comparison of data-MC pull widths for the muon hypothesis in TPC2. It can be seen that the widths in MC are systematically smaller than those in data.

Veto Detector (Selection)	Number of Events Cut			
	MC	Scaled MC	Data	Ratio
P0D	$3760 \pm 61.3$	$521 \pm 8.5$	515	$0.988 \pm 0.016$
ECal (CCQE)	$794 \pm 28.2$	$110 \pm 3.9$	113	$1.027 \pm 0.036$
ECal ( $CC1\pi^+$ )	$172 \pm 13.1$	$23 \pm 1.8$	23	$1.00 \pm 0.078$

Table 6.6: The Data-MC efficiency comparison of the veto cuts. Good agreement is seen in all cases.

tracks in MC to give a pull width inflated to the size of the data pull widths. 50 toy MC experiments were performed using this smearing method and the RMS of the ratio in the MC experiments is taken as the systematic error in each energy bin.

### 6.7.8 Veto Systematics

The systematic errors introduced by the veto cuts are also considered. There are two possible causes of systematic error for each cut. The first is a random coincidence of events or cosmic rays in the FGD and veto detectors that causes signal events to be wrongly rejected. The second is the tracking efficiency of the detector in question that causes the rate of background accepted to differ between data and MC. The systematic errors on these cuts are expected to be small due to the small number of events rejected by these cuts and the good data-MC agreement in the number of rejected events as shown in Table 6.6.

#### P0D Veto Systematic

The probability for two interactions to occur in the P0D in a single bunch was studied in [73]. The pileup rate was less than 0.5% and its systematic error was found to be less than 0.05% for two interactions in the P0D. The lower mass of the FGD will reduce the probability of a P0D-FGD pileup further. As this error is small and the number of events rejected by the cut is small, this source of systematic error is ignored here.

The tracking efficiency of the P0D detector is studied in [73]. The efficiency of matching a P0D-TPC track is measured. This efficiency will be defined by the P0D reconstruction and the matching efficiency. This efficiency is conservatively used to estimate the systematic error due to P0D tracking efficiency. Averaging across the momentum range the systematic error for the reconstruction efficiency is found to be 3%. This error is then applied to the number of events removed by the cut to calculate the effect on the ratio measurement.

### **ECal Veto Systematic**

The tracking efficiency of the ECal has been studied using the testbeam data taken at CERN[74] and beam spill data[68]. The study from beam spill data used a sample of tracks passing through TPC 3. These tracks were extrapolated to the DsECal front face and those entering the ECal were selected. This sample was used to measure the efficiency of the ECal reconstruction and the tracker-ECal matching. Unlike the P0D veto, the ECal veto is concerned with both efficiencies as the cut is based on the number of unmatched clusters found in the ECal. A change in either the reconstruction or matching systematic will introduce a systematic uncertainty to the performance of this cut. Averaged over angle and momentum, the data MC difference was found to be  $0.04 \pm 0.05$ . Combining these in quadrature we take the systematic error to be  $\pm 0.064$ . As per the P0D veto cut, this error is applied to the number of events removed by the cut and the effect on the ratio is measured.

### **6.7.9 FGD Multiplicity Systematic**

The FGD multiplicity cut is sensitive to systematic uncertainties in the tracker reconstruction. These systematic uncertainties have been assessed elsewhere and are not considered again. Instead, they have been initially treated in such a way that any effect caused through the FGD multiplicity cut will be accounted for and included in their overall effect. The systematics that will effect the performance of this cut are the TPC track finding efficiency and the FGD-TPC matching efficiency. The TPC tracking efficiency and the FGD-TPC matching efficiency are relatively simple, any track lost to these effects is removed from the event as a whole and so their effect on the efficiency of this cut is folded into the overall effect for those uncertainties.



### 6.7.10 Momentum Resolution

The single TPC momentum resolution was studied for data and MC in [75]. The study used tracks crossing at least 2 TPCs to compute the difference between the reconstructed momenta. By using the three combinations of TPC pairs, the resolution of each TPC can be calculated. As it is more directly related to the track topology, the resolution of  $1/p_T$  is measured. There will be several contributions to the  $1/p_T$  resolution:

- Energy loss fluctuations from traversing the FGD(s).
- Variation in the distance travelled through the FGD(s)
- Multiple scattering in the FGD(s)
- The  $1/p_T$  resolution of the TPC(s)
- The correlation between these effects

The energy loss and multiple scattering contributions were extracted using the MC truth data. The distance through the FGD can be calculated using the position reconstruction. The correlation between the effects however cannot be assumed to be the same in data and MC. The only available reconstructed variable is the difference in the  $1/p_T$  resolutions measured by each TPC:

$$\sigma[\Delta \frac{1}{p_t^{rec}}] = \sigma[(\frac{1}{p_t})_i^{rec} - (\frac{1}{p_t})_j^{rec}] \quad (6.10)$$

. By expanding this equation adding and subtracting the true quantities in each TPC the covariance terms can be extracted. For TPC2 a resolution systematic of  $8 \times 10^{-5}(c/MeV)$  was found. This resolution was applied as an additional Gaussian smearing in the MC. No change to the MC results were found due to this smearing and so this systematic is taken to be so small as to have no effect on the analysis.

### 6.7.11 Momentum Scale

The MC used in this analysis assumes the magnetic field in the TPCs is uniform. In actuality there are distortions in the magnetic field at the edges of the detector. These distortions

will alter the momentum scale of track in the detector through two effects. The momentum reconstruction uses the curvature of the particle tracks to measure their momenta. If a particle passes through the magnetic field distortions its curvature will be altered and the momentum will be reconstructed incorrectly. The drift field in the TPCs is aligned parallel to the magnetic field so that the drift electrons will not be effected by the magnetic field. Distortions in the magnetic field will alter the path of drift electrons in the TPC and so will alter the position and shape of reconstructed tracks from the assumed perfect magnetic field case.

The magnetic field was surveyed using Hall probes before the installation of the ND280 basket detectors. The probes mapped a volume slightly larger than the basket detectors would occupy. The TPC region was mapped in detail using a 1000 A current and over 250000 measurement points. From this, a distortion map was produced and implemented in the MC. Details of the distortion mapping and subsequent correction in the MC are found in [76]. For the purposes of this analysis, the magnetic field distortions are taken to result in a -0.4% shift in momenta reconstructed using TPC2. This shift in the magnetic field was applied to the selections in this analysis and the effect measured. It was found that in many bins the effect was small due to limited statistics. As a conservative estimate we take the largest observed variation as an overall, symmetric error. A 2.5% systematic error is applied to all bins for the momentum scale systematic.

### **6.7.12 Fiducial Mass Uncertainty**

There exists a systematic uncertainty in the FGD fiducial mass. This will propagate through to cross-section measurements if there is a difference in the number of target nuclei between data and MC. However, as this analysis takes a cross-section ratio, any effect due to this uncertainty will be the same in both measurements and so will cancel and so is not relevant here.

Any difference in the fiducial volume between the selections will introduce a non-cancelling systematic to the ratio measurement. Both selections use the same target detector and fiducial volume, therefore, any systematic uncertainty in the fiducial volume must be a result of the reconstruction vertexing. If there is any difference in bias or reso-

lution between the samples, the fiducial volumes will differ. As shown in Section 6.7.6 the difference in Z position resolution is less than 0.5mm and the difference in bias is of order 1mm. Both of these differences are much less than the 10mm width of the FGD scintillator bars and any migration in the fiducial volume will be small compared to the full fiducial volume. For this reason, no systematic is assigned due to uncertainty in the fiducial mass.

### 6.7.13 Detector and Reconstruction Systematics Overview

Table 6.7 gives a summary of the reconstruction systematic errors applied per bin and Table 6.8 shows a summary of the reconstruction systematics applied uniformly across all bins.

	Neutrino Energy Bin							
	1	2	3	4	5	6	7	8
TPC Efficiency	2.3	2.2	2.0	1.4	1.25	1.25	1.3	0.8
FDG-TPC Matching	2.0	2.0	1.8	1.4	0.6	0.5	0.4	0.3
Broken Track	2.3	2.3	1.9	1.45	1.3	1.25	1.34	1.0
TPC-PID	17	5	2.6	1.7	1.9	1.4	0.8	2.4
Charge Confusion	9.3	3.1	2.5	2.8	2.8	1.8	2.8	3.9
Momentum Resolution	0.0	0.0	0.0	0.0	0.0	0.0	0.0	0.0

Table 6.7: A summary of reconstruction systematic errors applied to each bin. Each cell gives the percentage error.

Systematic Source	Percentage Error
Momentum Scale	2.5
Vertex Resolution	0.9
Michel Electron Tagging	0.54
POD Veto	0.12
ECal Veto	2.4
Sand Muons	0.46
Fiducial Volume	negligible
Total	3.62

Table 6.8: The list of overall reconstruction systematics and the assigned percentage errors assigned.

#### 6.7.14 Sand Muons

A number of neutrinos interact in the walls surrounding the ND280 detector. These interactions produce so called sand muons that may enter ND280 and fake a signal event. These sand interactions are not simulated in the nominal ND280 MC and so a set of special sand muon MC files was generated. This MC sand muon data set is equivalent to  $7 \times 10^{19}$  POT. The selection cuts were applied to these MC files to estimate the sand muon background. No events were found to pass all of the  $CC1\pi^+$  selection cuts and 5 events were selected by the CCQE cuts. Scaling to the total data POT gives an expected 7.7 events. This is 0.42% of the final CCQE selection. The number of CCQE events selected is varied by 0.42% and the effect on the overall ratio is taken to be the systematic error. This error is conservative but more precise methods are not feasible due to the low sand muon sample statistics.

### 6.8 Interaction and Model Systematics

The largest systematic errors come from the uncertainties in the interaction and cross section model used in the MC. The rates of different interaction processes are defined by parameters such as  $M_A^{QE}$  and  $M_A^{RES}$ . The values for these parameters are obtained from best fits to the results of previous experiments[77] and have associated uncertainties. To obtain the one sigma systematic error introduced by this uncertainty, the values of these parameters in the models must be varied and the effects on the predicted ratio must be quantified.

#### 6.8.1 Event ReWeighting

The full MC production chain takes years of CPU time and uses many terabytes of disk space making MC very expensive to produce and store. It is therefore unfeasible to create multiple sets of MC data using different interaction model parameters. In order to avoid the need for multiple MC sets we use event reweighting. For each event we calculate a weight based on the change of a parameter from  $\vec{x} \rightarrow \vec{x}'$  for event  $i$  such that:

$$w_i = \frac{\sigma(\vec{x}')}{\sigma(\vec{x})} \quad (6.11)$$

where  $w_i$  is the event weight,  $\sigma(\vec{x})$  is the nominal cross section and  $\sigma(\vec{x}')$  is the new cross section based on the varied model parameter. The reweighted MC data set can be considered equivalent to a new MC data set with modified parameters and is much less CPU intensive to produce. This conjecture only holds under a certain set of conditions. Firstly, the original MC must contain all the information required to generate event weights. If there are no events in a given phase space in the original MC, there will be no events in this phase space in the reweighted sample. Essentially, you cannot reweight zero. Secondly, the parametrisation must be sufficient for reweighting. The reweighting must properly represent the cross sections as a function of the interaction kinematics. Finally, the original MC set must have enough statistics such that the reweighting has meaning. Small contributions to a larger data set must populate the phase space smoothly.

The reweighting done in this analysis uses the T2KReWeight package. This is a general reweighting tool and links directly to the neutrino interaction generators (NEUT in the case of this analysis). In order to reweight the selected events the reconstructed vertex must be matched back to the true vertex that created it. This true vertex must then be matched to the vertex generated by the interaction generator. The output of the NEUT generator is copied directly and it is this output that is used in the reweighting.

### 6.8.2 Flux Uncertainty

The production of the neutrino beam is simulated by the T2K beam group and a predicted flux is provided to produce the ND280 MC files. Details on the production of the flux inputs can be found in [78]. The default flux used to produce the MC does not completely represent the beam spectrum actually provided in data. As such a tuned beam spectrum is provided by the beam group and the MC has been reweighted to this tuned beam spectrum.

Further to the tuning of the flux MC, a number of uncertainties exist in the prediction of the beam flux. The uncertainties are largely due to uncertainties in the rate of hadron production on a thin carbon target taken from NA61 and other experimental data[78]. A covariance matrix is produced for each source of uncertainty on the flux. These matrices are combined in quadrature to produce a total fractional covariance matrix as shown in Figure 6.25.

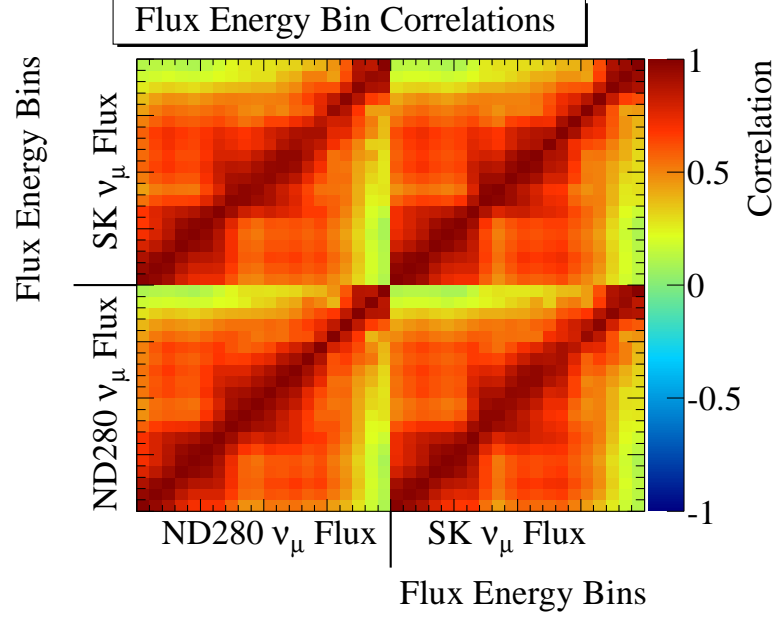


Figure 6.25: The total flux covariance matrix provided with the 11bv3.1 beam tuning for the ND280 and SK  $\nu_\mu$  flux. For this analysis only the ND280 covariances are relevant.

The covariance matrix describes the uncertainty on the  $E_\nu$  spectrum shape. This uncertainty will affect each selection differently but will cancel to some extent when taking the cross-section ratio, thereby reducing one of the largest sources of systematic uncertainty. To evaluate the size of the uncertainty the MC is reweighted using the covariance matrix. In order to make the reweighting quicker, the covariance matrix,  $V_{ij}$  is decomposed using Cholesky Decomposition to give the triangular matrix  $W_{i\alpha}$  such that,

$$V = W_W^T \quad (6.12)$$

We then create a reweighting factor,  $b_i$ , for each  $E_\nu$  bin  $i$ , defined such that,

$$b_i = 1 + \sum_{\alpha=1}^{nbins} W_{i\alpha}^b r_\alpha \quad (6.13)$$

where  $b_i = 1$  returns the nominal flux. The elements of vector  $r_\alpha$  are randomly generated from a Gaussian with mean 0 and sigma 1. The number of reweighted events in bin  $i$

$E_\nu$ Bin	1	2	3	4	5	6	7	8
Percentage Error	9.41	8.29	7.89	7.89	5.39	3.95	4.95	7.6

Table 6.9: The symmetric systematic error on the ratio due to the flux shape uncertainty.

$(N_i^{pred})$  is then given by,

$$N^{pred}_i = \epsilon(E_i)\sigma(E_i)b_i\phi_i \quad (6.14)$$

where  $\epsilon(E_i)$  and  $\sigma(E_i)$  are the selection efficiency and the cross-section in bin  $i$  respectively.

200 throws of  $r_\alpha$  are taken for each selection and used to reweight the flux. The ratio is measured for each reweighting and the RMS of the measured ratios in a given energy bin is taken to be the systematic error due to flux uncertainties. The percentage errors due to flux uncertainties are shown in Table 6.9.

### 6.8.3 Neutrino Interaction and Final State Interaction Uncertainties

The NEUT interaction generator is used to produce the interactions for the MC sample using a given set of interaction parameters. NEUT also simulates the nuclear re-interactions of the particles with a set of parameters. As such, NEUT is used in the reweighting of both sets of parameters. To calculate the systematic errors due to cross section and re-interaction uncertainties, each available interaction parameter is varied in turn by plus or minus one times its one sigma uncertainty. The reweighting is applied separately to the CCQE and  $CC1\pi^+$  samples. The ratio is then calculated for each pair of associated, reweighted, MC sets. The deviation of the cross section ratio from the nominal ratio is then taken to be the one sigma systematic due to the uncertainty on the varied interaction parameter. Table 6.10 shows the systematic errors due to various cross section parameters and final state interaction uncertainties. The largest contributions to the errors comes from the axial and vector masses governing the quasi elastic and resonance production rates. This is to be expected as these parameters have a most direct effect on the cross section ratio. The uncertainty due to the DIS (Deep Inelastic Scattering) background events is estimated by varying the normalisation of the DIS event rate. DIS is the main background in the  $CC1\pi^+$  selection and so has a relatively large effect on the cross section ratio. The CC

Parameter	Percentage Error per $E_\nu$ Bin							
	1	2	3	4	5	6	7	8
$M_A^Q E$	+5.1 -3.4	+7.2 -4.6	+7.6 -4.9	+8.8 -5.8	+9.6 -6.2	+8.9 -6.8	+8.9 -6.5	+7.6 -5.0
$M_A^R ES$	+7.7 -9.0	+11.2 -2.1	+3.3 -4.2	+2.1 -2.8	+2.6 -3.7	+5.2 -5.5	+5.4 -4.9	+8.8 -7.1
$M_v^R ES$	+7.3 -7.1	+2.6 -3.0	+2.8 -3.0	+2.8 -3.0	+1.9 -2.0	+4.4 -2.7	+3.5 -2.9	+5.5 -4.1
DISNorm	+3.9 -4.0	+9.0 -9.1	+1.7 -1.7	+3.6 -3.6	+6.0 -6.1	+7.9 -8.1	+10.1 -10.5	+11.0 -11.5
CCOtherNorm	+1.7 -1.7	+4.2 -4.2	+4.3 -4.3	+1.1 -1.1	+2.0 -2.1	+3.8 -3.8	+5.8 -5.9	+8.3 -8.2
Pion Production	+0.2 -0.4	+0.7 -1.8	+0.9 -1.4	+0.4 -0.4	+0.3 -1.0	+1.0 -1.5	+0.2 -0.0	+2.0 -2.2
Charge Exchange	+1.7 -2.3	+0.5 -2.7	+0.6 -0.2	+0.9 -1.6	+1.0 -1.0	+0.6 -0.8	+1.4 -1.9	+1.6 -1.5
Pion Absorption	+3.4 -5.5	+1.4 -2.0	+7.8 -9.2	+3.7 -5.1	+4.1 -6.2	+2.2 -3.1	+3.5 -4.6	+3.2 -3.9
Pion FSI Scattering	+2.4 -2.2	+9.7 -3.3	+7.7 -7.0	+4.6 -5.6	+2.6 -4.0	+6.0 -4.4	+3.1 -3.4	+4.8 -4.9
Total Error	+13.5 -13.8	+20.9 -15.5	12.0 -11.56	+12.0 -11.8	+12.87 -11.63	+16.5 -15.1	+17.7 -16.8	+19.8 -18.4

Table 6.10: The systematics errors due to cross section and interaction uncertainties. An asymmetric error is applied to cross section ratio in each energy bin.

other parameter is varied to evaluate the systematic error due to CC background processes such as multiple pion production events.

NEUT also provides the simulation of the intra-nuclear re-interactions. The entire NEUT particle cascade is saved, including the pion creation and exit positions and the positions of any FSI vertices. Using this detailed information, effects of various FSI parameters can be properly calculated without the need to regenerate the full MC[48]. The systematic errors due to the uncertainty on the FSI parameters are given in the lower half of Table 6.10. The effects of both pion absorption and production are considered using the NEUT nominal values and uncertainties. The probabilities for intra-nuclear pion scattering and charge exchange are also varied to produce systematic errors on the ratio. The effects due to absorption and charge exchange are relatively small.



## 6.9 Results

The results of both selections and the ratio measurement are presented in this section. As the ratio is the main result presented, the systematics are only calculated for the ratio. The number of events selected in each individual selection are presented only for context and completeness. The number of events selected by cut are shown in Tables 6.11 and 6.12 for the CCQE-like and  $CC1\pi^+$ -like Run 2 MC samples respectively. The total number of events selected in Run 1 MC are 365  $CC1\pi^+$ -like and 3753 CCQE-like. These scale to  $56.5 \pm 8.7^{stat}$  expected  $CC1\pi^+$ -like events and  $581 \pm 24^{stat}$  expected CCQE-like events at data equivalent POT. The actual number of events seen in data is 52  $CC1\pi^+$  and 548 CCQE. Therefore we have an overall data/MC ratio of  $0.92 \pm 0.143^{stat}$  for  $CC1\pi^+$  and  $1.06 \pm 0.043^{stat}$  for CCQE. For Run 2 804  $CC1\pi^+$ -like events and 8865 CCQE-like events are selected in MC which scales to  $117 \pm 10.8^{stat}$  and  $1298 \pm 36^{stat}$ . In data 106  $CC1\pi^+$ -like and 1285 CCQE-like events are observed giving data/MC ratios of  $0.940 \pm 0.088^{stat}$  and  $0.957 \pm 0.027^{stat}$ . Using the values from Tables 6.11 and 6.12 the flux integrated ratio is calculated. The systematic error is taken to be a weighted average of the binned errors. In MC a ratio of  $R^{MC} = 0.2349 \pm 0.0186^{stat} \pm 0.0467^{syst}$  is observed and a ratio of  $R^{Data} = 0.2370$  is measured in data showing a good agreement between the two.

Cut Passed	No. Selected	No. Signal	Signal Fraction (%)	Efficiency (%)
Vertex Selection	76253	20428	26.79	74.33
1 -tive Track	33963	13378	39.38	48.68
2nd Track Stops	27397	11161	40.74	40.61
TPC Quality	17234	9840	57.09	35.81
Muon PID	12967	9305	71.75	33.86
0 Michel Electron	11999	9267	77.23	33.72
FGD-TPC Mult.	11456	9101	79.44	33.11
ECal Veto	9189	7810	84.99	28.41
POD Veto	8865	7666	86.47	27.89

Table 6.11: The number of events selected in the Run 2 MC CCQE analysis. The efficiencies are measured as a fraction of signal events selected out of 27481 True CCQE-like events in the sample

Cut Passed	No. Selected	No. Signal	Signal Fraction (%)	Efficiency (%)
Vertex Selection	17439	3280	18.8	51.6
1 -tive Track	10063	2325	23.2	36.59
TPC Quality	7470	2109	28.2	33.19
Muon PID	6210	1974	31.78	31.07
Single Pion	1117	675	60.42	10.62
FGD-TPC Mult.	975	643	65.9	10.12
ECal Veto	803	563	70.1	8.86

Table 6.12: The number of events selected in the Run 2 MC  $CC1\pi^+$  analysis. The efficiencies are measured as a fraction of signal events selected out of 6353 True  $CC1\pi^+$ -like events in the sample

	Reconstructed Neutrino Energy Bin						
	2	3	4	5	6	7	8
Total percentage Error	+23.21 -18.50	+23.60 -20.41	+15.29 -15.14	+14.89 -13.78	+17.55 -16.24	+19.00 -18.17	+22.00 -20.76

Table 6.13: Total Percentage Systematic Errors by Neutrino Energy Bin

The errors calculated for the previously detailed systematics are combined in quadrature and the total percentage error is given in Table 6.13. These systematic errors are applied to the final cross-section ratio measurement only. Figure 6.26 shows the bin cross-section ratio for data with statistical and systematic errors compared to the true MC ratio. Further to this, Figure 6.27 shows the double ratio where the measured data is normalised to the MC expectation for each bin. In this double ratio the MC statistical error is added as a further systematic to the measurement. A goodness of fit with the  $y = 1$  line was calculated using Minuit and is found to have a  $\chi^2/NDOF$  of 6.6/6.

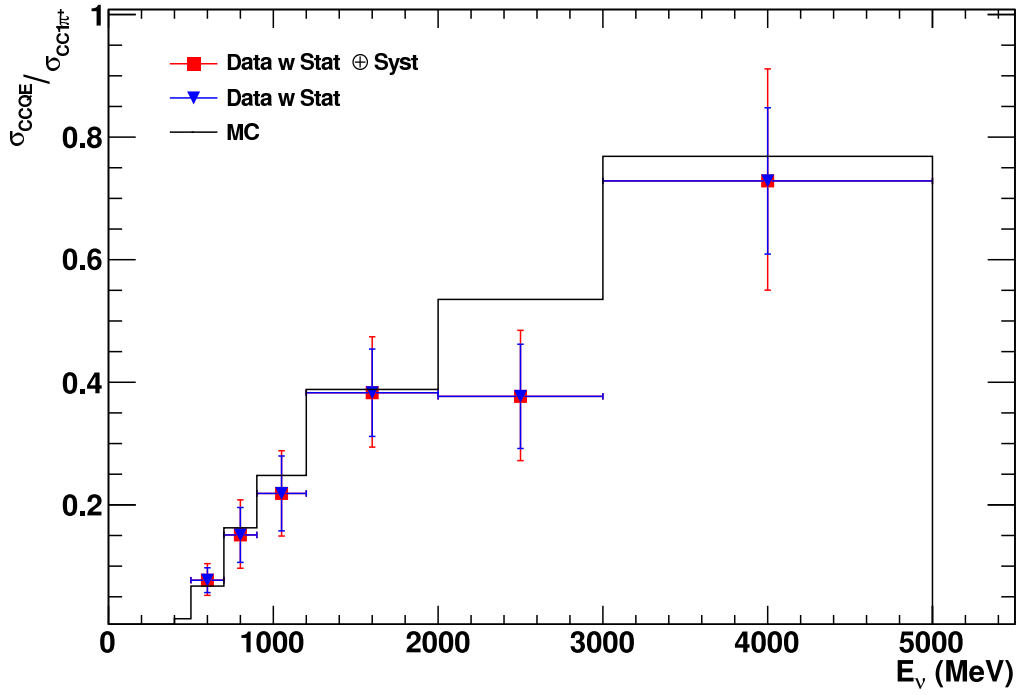


Figure 6.26: The measured  $CC1\pi^+/CCQE$  cross-section ratio with the true MC ratio for comparison. The data points show statistical errors and combined statistical and systematic errors. The final bin has been cut off at 5000 MeV to show the lower energy bins more clearly but contains events up to 10000 MeV.

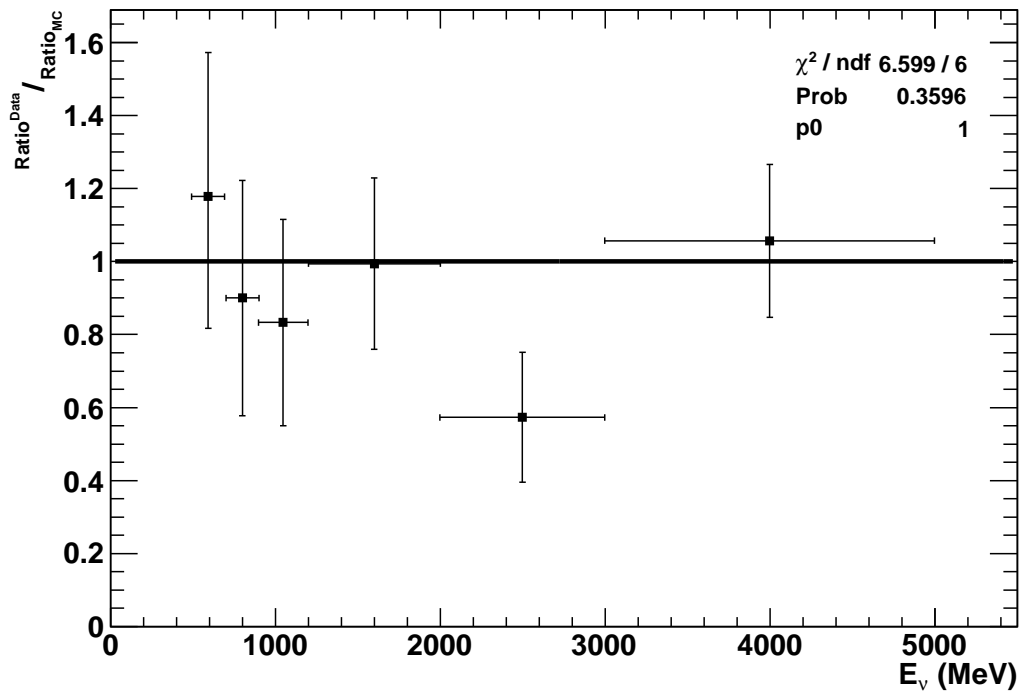


Figure 6.27: The  $CC1\pi^+$ / $CCQE$  cross-section double ratio. The ratio measured in each bin has been normalised to the MC ratio. As with the single ratio plot, the final bin is only shown up to 5000 MeV.

At this point we compare the results of this analysis with previous data from the MiniBooNE experiment[79]. The comparison is shown in Figure 6.28. A significant difference is seen between the result given here and the MiniBooNE result. It is also worth noting that the NEUT MC prediction is also different from the MiniBooNE data. Due to the model dependence introduced by the background subtraction and efficiency calculation methods, it is likely that the difference in the results stems from the difference in the MC. Unpublished work within the collaboration indicates that the difference in MC predictions is due to the inclusion of pionless delta decay in NEUT[80]. Pionless delta decay was not included in the MiniBooNE generator NUANCE. Pionless delta decay is a purely nuclear effect and should be removed if we correct for final state interactions.

An investigation was performed where the signal definition was defined by the particles produced at the true neutrino interaction vertex rather than those exiting the nucleus. With this new definition of signal, the ratio was recalculated. An additional scaling factor is applied to the FSI-corrected ratio in order to normalise the result to an isoscalar target. We use the factor 0.89 taken from K2K[81] since the target material is the same in this analysis. Figure 6.29 shows the comparison to MiniBooNE again but each data set has been corrected for final state interactions. As we can see the data sets now agree within statistical errors. This implies that some difference in the final state interaction models exists between the two MC generators and this is influencing the results through the background subtraction and efficiency correction. The hypothesis that this is due to the inclusion of pionless delta decay is favoured due to the size of the effect. As this process will effectively shift 20% of resonant events to the CCQE-like sample, migrating these events from the numerator of the ratio directly to the denominator.

To test how well the MC model matches observations, the kinematic distributions of tagged particles are plotted for events passing the selections without any corrections applied. This removes any dependence of the data on the background and efficiency predictions. Doing this also removes any models dependence introduced when reconstructing the neutrino energy. The rates from MC are scaled to the data POT and the raw distributions are compared. No systematic errors are applied to this comparison. Figure 6.30 shows the comparison of the muon kinematics for CCQE events. Good agreement is seen between the

data and MC, suggesting the MC is modelling the data well. Figures 6.31 and 6.32 show the same kinematic distributions for the muon and pion respectively in the  $CC1\pi^+$  selection. The data and MC agree well again, however, the small statistics create large error bars and some anomalies. In future analyses with increased statistics, more meaningful comparisons will be possible. Currently, the data and MC agree to the level that the MC appears to be modelling observations correctly.

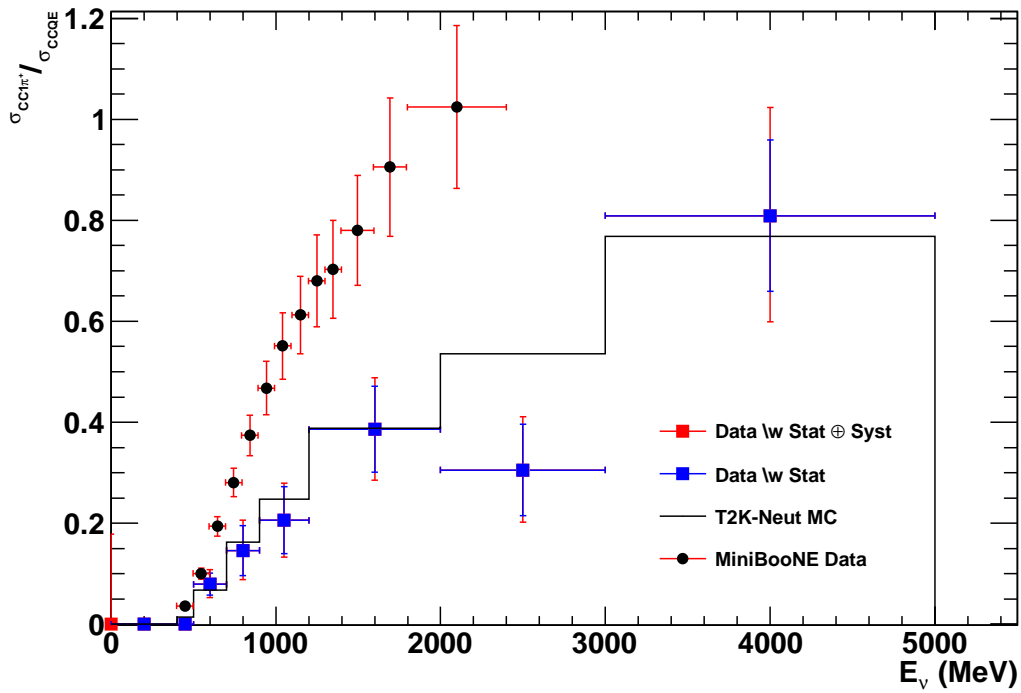


Figure 6.28: A comparison to past MiniBooNE measurements showing the MiniBooNE data and the T2K data with error bars and the NEUT prediction as a histogram.

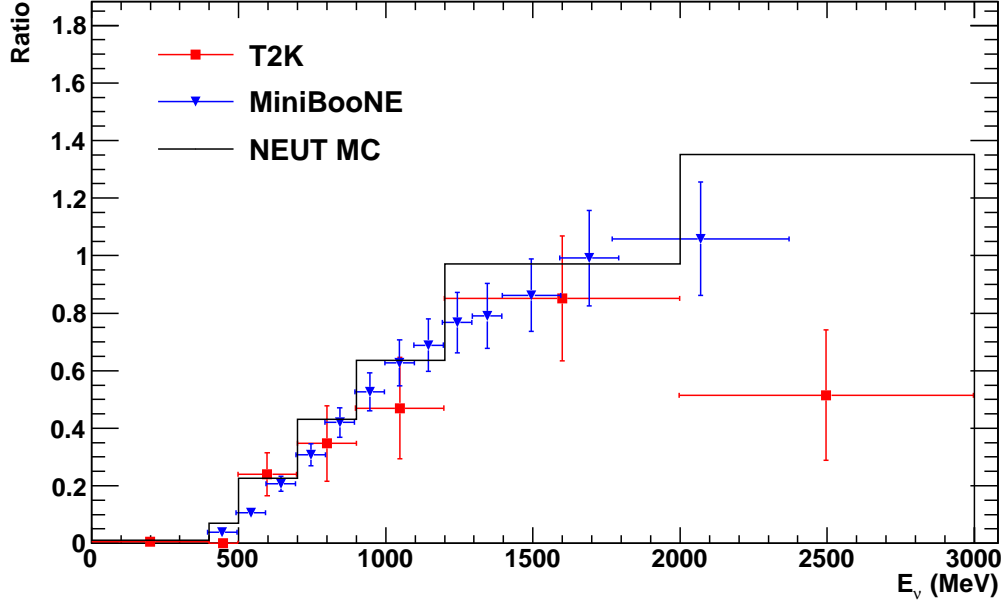


Figure 6.29: A second comparison to MiniBooNE data but this time correcting for final state interactions and normalising to an isoscalar target. The results and MC are now seen to agree. Only the region with MiniBooNE data is shown in the histogram.

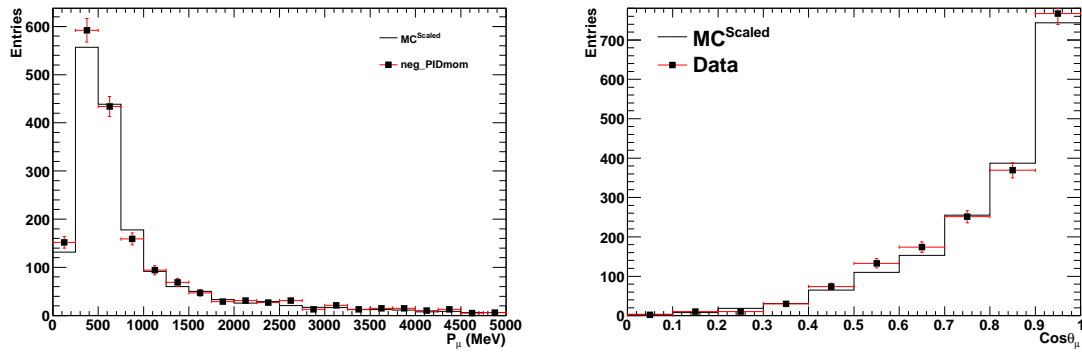


Figure 6.30: Left) The momentum of the particle tagged as the muon for events in the final CCQE selection. Right) The  $\cos\theta$  of the muon candidate where  $\theta$  is angle from the z-axis

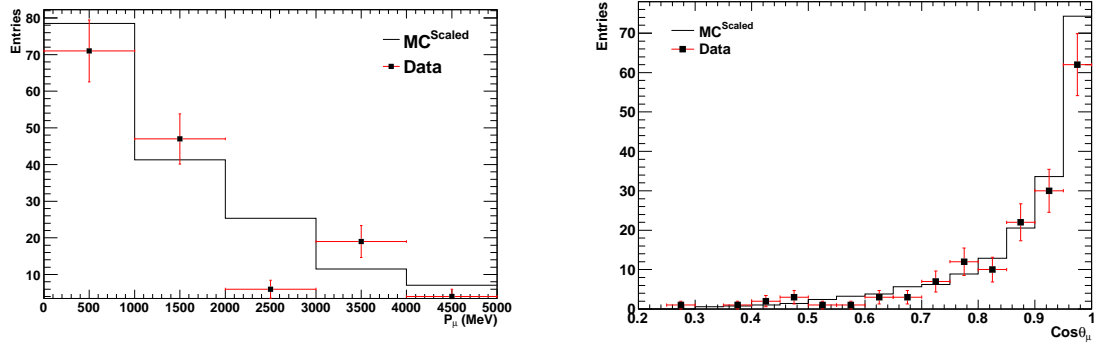


Figure 6.31: Left) The momentum of the particle tagged as the muon for events in the final  $CC1\pi^+$  selection. Right) The  $\cos\theta$  of the muon candidate where  $\theta$  is angle from the z-axis

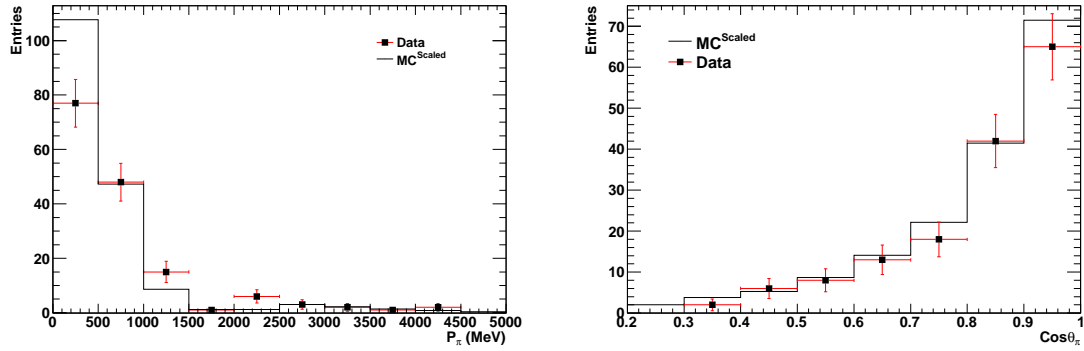


Figure 6.32: Left) The momentum of the particle tagged as the pion for events in the final  $CC1\pi^+$  selection. Right) The  $\cos\theta$  of the pion candidate where  $\theta$  is angle from the z-axis



## Chapter 7

### Conclusions

This thesis has described my work on three main projects. Firstly, the construction of the Barrel ECal modules, in which I made significant contributions. Secondly, the initial commissioning, operation and recovery of the ECal modules at the ND280 site in Japan. Finally, a  $CC1\pi^+/CCQE$  cross-section measurement in the ND280 tracker has been discussed. The current state of knowledge in the neutrino sector has been outlined, along with the T2K experiment.

Much of the work performed in the production of this thesis has concentrated on the ECal hardware. The construction of the ECal barrel modules has been discussed and the details of the construction materials and methods have been given as well as a brief overview of calorimetry. The construction of the ECals was a task requiring careful execution to build a long-lasting, well performing detector. The effective construction and design of the calorimeters (and ND280 as a whole) was shown during the recovery period after the 2011 earthquake. The ECal was found to have sustained only minimal damage and was quickly returned to efficient operation. The commissioning and operation of the ECal after its installation in the detector complex was both a challenging and important task. The duties involved and their importance were discussed. Data lost due to poor online calibration is rarely recoverable at a later point and so efficient operation is crucial to the acquisition of good quality data. In order to commission and operate the detector, a good knowledge of both the hardware itself and the online software methods was vital.

The cross-section ratio analysis described in this document is clearly dominated by statistical errors. Due to the low statistics, the aim has been to perform an initial measure-

ment of this ratio at T2K that can serve as a baseline for future analyses, where statistical errors will become less dominant. The development of this analysis has been challenging due to the low statistics in the  $CC1\pi^+$  channel and the current functionality of the reconstruction software; where both the FGD isolated reconstruction and the ECal reconstruction were unavailable in the data processing. A large proportion of the pions produced stop in the FGD and so these events are lost to the  $CC1\pi^+$  selection and add background to the CCQE selection. Future improvements to the reconstruction software will, therefore, allow for more precise measurements.

This analysis focussed on the selection of pion-like tracks and the rejection of high-multiplicity, multi-pion events. The signal definitions and selection have been performed in a model-independent way and do not correct for FSI effects. The ratio measurement technique has been successful in reducing the size of several systematics, most notably the flux uncertainty. Both a single cross-section ratio and a double cross-section ratio have been presented. From the double ratio measurement, the data is found to be consistent with the MC with a goodness of fit  $\chi^2/NDOF = 6.6/6$ . The results given here were then compared to results from previous experiments. A large discrepancy was observed between the results given here and the previous data. After correcting the measurements for final state interactions both measurements agree well. This implies some difference in the nuclear re-interaction models used and some model-dependence in this analysis. The raw kinematic distributions were compared between data and MC to test the MC model used without introducing any model-dependence to the observed quantities. The kinematic distributions were found to agree within the large statistical error bars.

## Bibliography

- [1] F. A. Scott, “Energy Spectrum of the Beta-Rays of Radium E,” *Phys. Rev.*, vol. 48, pp. 391–395, Sep 1935.
- [2] E. Fermi, “Towards the Theory of  $\beta$ -Rays,” *Z. Phys.*, vol. 8, pp. 161–177, 1934.
- [3] C. L. Cowan, F. Reines, F. B. Harrison, H. W. Kruse, and A. D. McGuire, “Detection of the Free Neutrino: a Confirmation,” *Science*, vol. 124, no. 3212, pp. 103–104, 1956.
- [4] F. Reines, C. L. Cowan, F. B. Harrison, A. D. McGuire, and H. W. Kruse, “Detection of the Free Antineutrino,” *Phys. Rev.*, vol. 117, pp. 159–173, Jan 1960.
- [5] G. Danby *et al.*, “Observation of High-Energy Neutrino Reactions and the Existence of Two Kinds of Neutrinos,” *Phys. Rev. Lett.*, vol. 9, pp. 36–44, Jul 1962.
- [6] M. L. Perl *et al.*, “Evidence for Anomalous Lepton Production in  $e^+ - e^-$  Annihilation,” *Phys. Rev. Lett.*, vol. 35, pp. 1489–1492, Dec 1975.
- [7] O. Adriani *et al.*, “Determination of the number of light neutrino species,” *Physics Letters B*, vol. 292, no. 3â4, pp. 463 – 471, 1992.
- [8] K. Kodama *et al.*, “Observation of tau neutrino interactions,” *Physics Letters B*, vol. 504, no. 3, pp. 218 – 224, 2001.
- [9] R. Davis, D. S. Harmer, and K. C. Hoffman, “Search for Neutrinos from the Sun,” *Phys. Rev. Lett.*, vol. 20, pp. 1205–1209, May 1968.
- [10] P. Anselmann *et al.*, “Solar neutrinos observed by GALLEX at Gran Sasso,” *Physics Letters B*, vol. 285, no. 4, pp. 376 – 389, 1992.

- [11] J. Abdurashitov *et al.*, “Measurement of the solar neutrino capture rate with gallium metal. III: Results for the 2002–2007 data-taking period,” *Phys.Rev.*, vol. C80, p. 015807, 2009.
- [12] F. Boehm *et al.*, “Final results from the Palo Verde neutrino oscillation experiment,” *Phys.Rev.*, vol. D64, p. 112001, 2001.
- [13] K. S. Hirata *et al.*, “Observation of  $^8\text{B}$  solar neutrinos in the Kamiokande-II detector,” *Phys. Rev. Lett.*, vol. 63, pp. 16–19, Jul 1989.
- [14] K. Hirata *et al.*, “Experimental study of the atmospheric neutrino flux,” *Physics Letters B*, vol. 205, no. 2â3, pp. 416 – 420, 1988.
- [15] R. Becker-Szendy *et al.*, “Search for muon neutrino oscillations with the Irvine-Michigan-Brookhaven detector,” *Phys. Rev. Lett.*, vol. 69, pp. 1010–1013, Aug 1992.
- [16] Y. Fukuda *et al.*, “Measurement of a small atmospheric muon-neutrino / electron-neutrino ratio,” *Phys.Lett.*, vol. B433, pp. 9–18, 1998.
- [17] Q. R. Ahmed *et al.*, “Measurement of charged current interactions produced by  $^8\text{B}$  solar neutrinos at the Sudbury Neutrino Observatory,” *Physical Review Letters*, vol. 87, no. 071301, 2001.
- [18] Q. Ahmad *et al.*, “Direct evidence for neutrino flavor transformation from neutral current interactions in the Sudbury Neutrino Observatory,” *Phys.Rev.Lett.*, vol. 89, p. 011301, 2002.
- [19] K. Eguchi *et al.*, “First Results from KamLAND: Evidence for Reactor Antineutrino Disappearance,” *Phys. Rev. Lett.*, vol. 90, p. 021802, Jan 2003.
- [20] J. N. Bahcall, M. C. Gonzalez-Garcia, and C. Peña-Garay, “Solar Neutrinos Before and After KamLAND,” *Journal of High Energy Physics*, vol. 2003, no. 02, p. 009, 2003.
- [21] Y. Oyama, “K2K (KEK to Kamioka) neutrino - oscillation experiment at KEK PS,” 1998.

- [22] P. Adamson *et al.*, “Measurement of Neutrino Oscillations with the MINOS Detectors in the NuMI Beam,” *Phys.Rev.Lett.*, vol. 101, p. 131802, 2008.
- [23] K. Abe *et al.*, “The T2K experiment,” *Nuclear Instruments and Methods in Physics Research Section A: Accelerators, Spectrometers, Detectors and Associated Equipment*, vol. 659, no. 1, pp. 106 – 135, 2011.
- [24] Z. Maki, M. Nakagawa, and S. Sakata, “Remarks on the Unified Model of Elementary Particles,” *Progress of Theoretical Physics*, vol. 28, no. 5, pp. 870–880, 1962.
- [25] B. Pontecorvo, “Neutrino Experiments and the Problem of Conservation of Leptonic Charge,” *Sov.Phys.JETP*, vol. 26, pp. 984–988, 1968.
- [26] T. Schwetz, M. Tórtola, and J. W. F. Valle, “Three-flavour neutrino oscillation update,” *New Journal of Physics*, vol. 10, no. 11, p. 113011, 2008.
- [27] B. Aharmim *et al.*, “Combined Analysis of all Three Phases of Solar Neutrino Data from the Sudbury Neutrino Observatory,” 2011.
- [28] E. Aliu *et al.*, “Evidence for Muon Neutrino Oscillation in an Accelerator-Based Experiment,” *Phys. Rev. Lett.*, vol. 94, p. 081802, Mar 2005.
- [29] P. Adamson *et al.*, “Measurement of the Neutrino Mass Splitting and Flavor Mixing by MINOS,” *Phys. Rev. Lett.*, vol. 106, p. 181801, May 2011.
- [30] K. Abe *et al.*, “First muon-neutrino disappearance study with an off-axis beam,” *Phys. Rev. D*, vol. 85, p. 031103, Feb 2012.
- [31] K. Abe *et al.*, “Search for Differences in Oscillation Parameters for Atmospheric Neutrinos and Antineutrinos at Super-Kamiokande,” *Phys. Rev. Lett.*, vol. 107, p. 241801, Dec 2011.
- [32] M. Apollonio *et al.*, “Search for neutrino oscillations on a long base-line at the CHOOZ nuclear power station,” *The European Physical Journal C - Particles and Fields*, vol. 27, pp. 331–374, 2003. 10.1140/epjc/s2002-01127-9.

- [33] P. Adamson *et al.*, “New constraints on muon-neutrino to electron-neutrino transitions in MINOS,” *Phys. Rev. D*, vol. 82, p. 051102, Sep 2010.
- [34] K. Abe *et al.*, “Indication of Electron Neutrino Appearance from an Accelerator-Produced Off-Axis Muon Neutrino Beam,” *Phys. Rev. Lett.*, vol. 107, p. 041801, Jul 2011.
- [35] F. P. An *et al.*, “Observation of Electron-Antineutrino Disappearance at Daya Bay,” *Phys. Rev. Lett.*, vol. 108, p. 171803, Apr 2012.
- [36] J. K. Ahn *et al.*, “Observation of Reactor Electron Antineutrinos Disappearance in the RENO Experiment,” *Phys. Rev. Lett.*, vol. 108, p. 191802, May 2012.
- [37] N. Abgrall, “The NA61/SHINE long target pilot analysis for T2K,” 2011.
- [38] G. P. Zeller, “Low energy neutrino cross sections from K2K, MiniBooNE, SciBooNE, and MINER $\nu$ A,” *Journal of Physics: Conference Series*, vol. 136, no. 2, p. 022028, 2008.
- [39] D. Casper, “The NUANCE neutrino physics simulation, and the future,” *Nuclear Physics B - Proceedings Supplements*, vol. 112, no. 1â3, pp. 161 – 170, 2002.
- [40] J. A. Nowak, “Wrocław neutrino event generator,” *Physica Scripta*, vol. 2006, no. T127, p. 70, 2006.
- [41] C. Andreopoulos *et al.*, “The GENIE neutrino Monte Carlo generator,” *Nuclear Instruments and Methods in Physics Research Section A: Accelerators, Spectrometers, Detectors and Associated Equipment*, vol. 614, no. 1, pp. 87 – 104, 2010.
- [42] Y. Hayato, “Neut,” *Nuclear Physics B - Proceedings Supplements*, vol. 112, no. 1â3, pp. 171 – 176, 2002.
- [43] C. Llewellyn Smith, “Neutrino Reactions at Accelerator Energies,” *Phys. Rep. 3C*, 1972.

- [44] H. J. Grabosch *et al.*, “Cross-section measurements of single pion production in charged current neutrino and antineutrino interactions,” *Zeitschrift für Physik C Particles and Fields*, vol. 41, pp. 527–531, 1989. 10.1007/BF01564697.
- [45] D. Rein and L. M. Sehgal, “Neutrino-excitation of baryon resonances and single pion production,” *Annals of Physics*, vol. 133, no. 1, pp. 79 – 153, 1981.
- [46] D. Rein and L. M. Sehgal, “Coherent  $\pi^0$  production in neutrino reactions,” *Nuclear Physics B*, vol. 223, no. 1, pp. 29 – 44, 1983.
- [47] G. Rowe, M. Salomon, and R. H. Landau, “Energy-dependent phase shift analysis of pion-nucleon scattering below 400 MeV,” *Phys. Rev. C*, vol. 18, pp. 584–589, Jul 1978.
- [48] *NEUT Nuclear Effects (FSI) T2K-TN-33*.
- [49] Y. Giomataris, P. Rebougeard, J. Robert, and G. Charpak, “MICROMEGAS: a high-granularity position-sensitive gaseous detector for high particle-flux environments,” *Nuclear Instruments and Methods in Physics Research Section A: Accelerators, Spectrometers, Detectors and Associated Equipment*, vol. 376, no. 1, pp. 29 – 35, 1996.
- [50] N. Abgrall *et al.*, “Time projection chambers for the T2K near detectors,” *Nuclear Instruments and Methods in Physics Research Section A: Accelerators, Spectrometers, Detectors and Associated Equipment*, vol. 637, no. 1, pp. 25 – 46, 2011.
- [51] D. Michael *et al.*, “The magnetized steel and scintillator calorimeters of the MINOS experiment,” *Nuclear Instruments and Methods in Physics Research Section A: Accelerators, Spectrometers, Detectors and Associated Equipment*, vol. 596, no. 2, pp. 190–228, 2008.
- [52] F. Zappa *et al.*, “On the bremsstrahlung origin of hot-carrier-induced photons in silicon devices,” *IEEE Trans Electron Dev*, vol. 40, p. 577, 1993.
- [53] *MCM 2 and the Trip chip, DO note 4009*.

- [54] A. Vacheret *et al.*, “The front end readout system for the T2K-ND280 detectors,” in *Nuclear Science Symposium Conference Record, 2007. NSS '07. IEEE*, vol. 3, pp. 1984 –1991, 26 2007-nov. 3 2007.
- [55] *Data Quality at the near detectors for Run2, T2K-TN-50.*
- [56] A. Cervera-Villanueva, J. Gómez-Cadenas, and J. Hernando, “RecPack, a reconstruction toolkit,” *Nuc. Instr. Meth. in Phys. Rev. A*, vol. 534, no. 1â2, pp. 180 – 183, 2004.
- [57] R. Brun and F. Rademakers, “ROOT: An object oriented data analysis framework,” *Nucl.Instrum.Meth.*, vol. A389, pp. 81–86, 1997.
- [58] S. Agostinelli *et al.*, “GEANT4: A simulation toolkit,” *Nucl. Instrum. Meth.*, vol. A506, pp. 250–303, 2003.
- [59] “MYSQL online: URL=<http://www.mysql.com/>,” Aug. 2012.
- [60] *ND280 Reconstruction, T2K-TN-72.*
- [61] *Particle Identification with the T2K TPC, T2K-TN-001.*
- [62] *Global Kalman vertexing in ND280, T2K-TN-46.*
- [63] A. Belkov, “Implementation of the Hough Transform for 3D Track Reconstruction in Drift Chambers,” *ArXiv Physics e-prints*, Jan. 2002.
- [64] Y. Hayato, “Neut,” *Nuclear Physics B - Proceedings Supplements*, vol. 112, no. 1â3, pp. 171 – 176, 2002.
- [65] C. Andreopoulos *et al.*, “The genie neutrino monte carlo generator,” *Nuclear Instruments and Methods in Physics Research Section A: Accelerators, Spectrometers, Detectors and Associated Equipment*, vol. 614, no. 1, pp. 87 – 104, 2010.
- [66] *CCQE-like and CC-non-QE-like  $\nu_\mu$  event selections in the ND280 tracker using Run 1+2 data T2K-TN-093.*



- [67] *Inclusive  $\nu_\mu$  CC analysis using the entire ND280 detector T2K-TN-044.*
- [68] *Measurement of the  $\nu_e$  beam component with Run1+Run2 data using the ND280 Tracker T2K-TN-094.*
- [69] *ND280 tracker tracking efficiency T2K-TN-075.*
- [70] *Charge Misidentification in local and global reconstruction T2K-TN-048.*
- [71] *Michel electron tagging in FGD1 T2K-TN-104.*
- [72] *PID systematics of the Time Projection Chambers for the  $\nu_\mu$  analysis T2K-TN-078.*
- [73] *Inclusive  $\nu_\mu$  CC events in the P0D in Run 1+2 T2K-TN-080.*
- [74] *T2K 2010a Analysis DsECAL Status Report T2K-TN-018.*
- [75] *Study of TPC Momentum Resolution From Tracks That Cross Multiple TPCs and the Associated Systematic Error on the  $\nu_\mu$  CC and CCQE Analyses, T2K-TN-095.*
- [76] *Measurement and Correction of Magnetic Field Distortions in the Time Projection Chambers, T2K-TN-061.*
- [77] *Cross section parameters for the 2012a oscillation analysis T2K-TN-032.*
- [78] *Neutrino Flux Uncertainty for 10a data analysis T2K-TN-039.*
- [79] A. A. Aguilar-Arevalo *et al.*, “Measurement of the Ratio of the  $\nu_\mu$  Charged-Current Single-Pion Production to Quasielastic Scattering with a 0.8 GeV Neutrino Beam on Mineral Oil,” *Phys. Rev. Lett.*, vol. 103, p. 081801, Aug 2009.
- [80] P. de Perio, “NEUT-MiniBooNE Comparisons: T2K Internal Document,” Feb 2011.
- [81] A. Rodriguez *et al.*, “Measurement of single charged pion production in the charged-current interactions of neutrinos in a 1.3 GeV wide band beam,” *Phys. Rev. D*, vol. 78, p. 032003, Aug 2008.